UNIVERSITY OF CALIFORNIA

Los Angeles

Understanding Cycling Mechanisms and Degradation in High-Capacity Electrodes for Ion Battery Applications

A dissertation submitted in partial satisfaction of the

requirements for the degree Doctor of Philosophy

in Chemistry

by

Andrew Akash Dawson

2023

ABSTRACT OF THE DISSERTATION

Understanding Cycling Mechanisms and Degradation in High-Capacity Electrodes for Ion Battery Applications

by

Andrew Akash Dawson

Doctor of Philosophy in Chemistry

University of California, Los Angeles, 2023

Professor Sarah H. Tolbert, Chair

Lithium-ion batteries are essential energy storage devices for modern-day technology and for creating a more sustainable future. One limitation is the energy density. This dissertation describes materials to increase the energy density of batteries, design principles to encourage reversibility, and examines how the structure changes with lithiation and delithiation. The first part focuses on nanoporous tin antimonide (NP-SbSn) as an anode material. NP-SbSn performs well with only 1% capacity fade after 100 cycles. To make structure-property relationships, we use a combination of transmission x-ray microscopy (TXM), X-ray diffraction (XRD), and transmission electron microscopy (TEM). We compare these results with previous results on nanoporous tin to show that the use of an intermetallic stabilizes the structure and discover that the mechanism of lithiation involves amorphization, unlike bulk SbSn. Because of the increased

stability of SbSn vs Sn, NP-SbSn is cycled with sodium, a harder material to cycle with. There is more structural degradation, but we obtain 85% capacity retention of after 100 cycles, To increase structural stability, a surface coating of aluminum oxide was added resulting in less structural damage under sodiation when compared to uncoated NP-SbSn.

The second part of the dissertation focuses on nanoporous antimony (NP-Sb). NP-Sb is used to study the effects of non-crystalline intermediates when cycling because we observed amorphization during lithiation of NP-SbSn. Unusually, Sb cycles similarly with sodium as with lithium. When cycled against lithium, NP-Sb has crystalline intermediates and amorphous intermediates, when cycled against sodium. Through XRD and TXM, we show how crystalline changes can have large effects on macro- and meso-scale structure. Also, we reveal synergistic effects when amorphous intermediates are combined with mesoporosity.

Lastly, we synthesize novel, icosahedral boron clusters as a cathode material through solid-state methods, atypical for boron cluster syntheses. These clusters are cross-linked with disulfides, resulting in redox active sulfur and clusters. The cluster's role is two-fold: the cross-linked nature prevents sulfur dissolution and provide capacity. We observe solid-state redox of the cluster, for the first time, and sulfur with reversible cycling. Cluster and sulfur redox are confirmed with *operando* Raman spectroscopy.

This dissertation of Andrew Akash Dawson is approved.

Chong Liu

Xiangfeng Duan

Ximin He

Sarah H. Tolbert, Committee Chair

University of California, Los Angeles

2023

To my supporters

TABLE OF CONTENTS

List of Figures

Chapter 2. Understanding Stabilization in Nanoporous Intermetallic Alloy Anodes for Li Ion Batteries Using *Operando* Transmission X-ray Microscopy

List of Schemes

Acknowledgements

There are far too many people to thank for supporting me throughout my journey in becoming a scientist. I will, without a doubt, miss some people, but I hope to mention the majority. I would like to begin with my research mentors. Professor Tolbert has been the main scientific mentor in my life. She has taught me an incredible amount of science, but also how to be a scientist. She cares deeply for her students and challenges them to push themselves wherever they are at. Professor Tolbert has a great way of communicating science, and her love of science is contagious. I would like to appreciate some other professors in graduate school for their guidance and conversation. These include Professors Liu, Spokoyny, and Duan. Dr. Johanna Nelson Weker also was an amazing mentor at the Stanford Synchrotron Radiation Lightsource. She has witnessed me at my most stressed and darkest moments, but she always helped me, including with life advice. I fell in love with research during my undergraduate degree, and I have many mentors to thank. Professors Metiu and McFarland gave me my first shot at research as a first-year student. Professor Moth-Poulsen allowed me in his lab in Sweden and supported my ideas fully. Lastly, Julie Standish and Dotti Pak were instrumental in providing funding and supporting my research endeavors. There are other teachers and mentors that helped me in my life that did not support me as a researcher. Dr. Rita Blaik and Elaine were in charge of the science outreach program at UCLA, and it was a breath of fresh air working with them. In college, Professor Laverman and Mehta supported all my wild ideas and encouraged my growth in the College of Creative Studies. Dave Whitman showed me how to me a good mentor. High school provided me with an abundance of great teachers, in particular Dr. Dalton, and, even earlier, Lisa Bennet and David Kristoff helped me grow to who I am today.

I must thank all my friends at UCLA who have helped me throughout this journey. The Tolbert group has been incredibly supportive. My mentors were Professor Eric Detsi and Dr. Terri Lin. Dr. Terri Lin was my mentor for a long time, and I could not have done this without her support. Other older students include: Dr. Patrick Yee, Dr. Abraham Buditama, Ty Karaba, Dr. KJ Winchell, Dr. Tori Basile, Erick Harr, Dr. Ben Lesel, Dr. Yan Yan, and Dr. Stephen Sasaki. Students in my year were also helpful: Dr. Sophia King, Dr. Jeffrey Kurish, Yiyi Yao, and Edgar Olivera. Students that started after me were amazing partners in science: Danny Robertson, Shreya Patel, and Charlene Salamat. Joseph Mazzetti has been my mentee for almost my entire graduate career and has worked tirelessly with me. He has often let me know when I dreamed too big. There has also been colleagues not in the Tolbert group who have helped me: Dr. Jason Belling, Liv Heidenreich, and Dr. David Agyeman-Budu. Also, I want to thank the Dunn group who I have worked with in Battery Journal Club. Other friends from high school and college have been supportive as well including Dr. Tsuyoshi Kohlgruber and Henry Morse.

Lastly, I must thank my family and those closest to me. I first must thank my partner, Risa Jensen who, for some reason, still sticks around with me after more than eight years. She has seen me through my graduate school experience and witnessed my highs and lows. Her mother, Kathy, and father, Joel, have always been supportive of me. They see me as a son and have never wavered in accepting me. It is unfortunate that I could not share this moment with Joel, because of his death by suicide, but, as one of the smartest engineers I have met, he was always someone I loved talking to about science. My in-laws and niece and nephew helped me stay positive as well: Shannon Dawson, Jeremy Lawson, Kabir Lawson, and Simran Lawson. Most importantly, I want to thank my nuclear family of Dulcie Dawson, Joseph Dawson, Sandra Lawson, Noel Dawson, and Anthony Dawson have always pushed me to pursue anything. We

definitely did not have much growing up sometimes, but my family has always been there to challenge and push me to be my best. Each one of them has taught me so much that I would not have learned otherwise, and I would be a much worse person without their guidance.

Contributions of Co-Authors

Chapter 2 is a version of Terri C. Lin, **Andrew Akash Dawson**, Yan Yan, David S. Ashby, Sophia C. King, Bruce Dunn, Johanna Nelson Weker, and Sarah H. Tolbert, " Understanding Stabilization in Nanoporous Intermetallic Alloy Anodes for Li Ion Batteries Using *Operando* Transmission X-ray Microscopy." Sophia and David provided the TEM images. Yan did the XPS. Professor Dunn and Tolbert helped edit and guide the research. Joahnna helped to collect the TXM data and analyze it. Terri and I did synthesis, cycling, and TXM imaging and processing. This was published in ACS Nano.

Chapter 3 is a version of Terri C. Lin, **Andrew Akash Dawson**, Yiyi Yao, and David Agyeman-Budu, Johanna N. Weker, and Sarah H. Tolbert, "Using Transmission X-Ray Microscopy to Understand Stability in Nanoporous Antimony Tin for Application as Sodium Ion Battery Anodes." Professor Tolbert helped edit and guide the research. Johanna helped with data collection and advised with analysis. Yiyi and David did the *operando* X-ray diffraction and analyzed the data. Terri and I synthesized, cycled, and collected and analyzed the TXM data. This work will be published after this dissertation is submitted.

Chapter 4 is a version of Terri C. Lin. Ryan Sheil, Jonathan Lau, **Andrew Akash Dawson**, David Ashby, Johanna N. Weker, Bruce Dunn, Jane P. Chang, and Sarah H. Tolbert, " Improved Cycling Capabilities of Nanoporous Antimony Tin with Atomic Layer DepositionAluminum Oxide for Sodium Ion Battery. Ryan coated the material. Jonathan cycled the material. Terri synthesized the material. David provided the TEM images. Professors Dunn, Chang, and Tolbert helped edit and guide the research. Johanna helped with data collection. I wrote and analyzed the TXM images as well as collected the TXM data with Terri. This work will be submitted after the dissertation is submitted.

Chapter 5 is a version of **Andrew Akash Dawson**, Joseph Mazzetti, David Agyeman-Budu, Yiyi Yao, Daniel Robertson, Johanna Nelson Weker, and Sarah H. Tolbert, "Understanding Stability in Nanoporous Antimony as Lithium and Sodium Ion Battery Anodes Using *Operando* Diffraction and Microscopy." David helped with obtaining the TXM data and preparation at SSRL. Yiyi and Daniel analyzed and took the diffraction data. Johanna helped with beamline support, and Professor Tolbert guided the research and helped edit. Joseph and I synthesized and cycled the material. We also analyzed the TXM data.

Chapter 6 is a version of **Andrew Akash Dawson**, Yessica Nelson, Alexander Spokoyny, and Sarah H. Tolbert, " RedOx Active Dodecaborated as a Cathode Material for Li-ion Batteries." Professors Spokoyny and Tolbert helped guide the research. Yessica synthesized the precursor clusters and obtained the FTIR data. I performed the sulfurization, collected the XPS data, and cycled the material as a battery. This work has not been published before this dissertation.

VITA

2014-2015	Research Internships in Science and Engineering Intern
2014	Mentor for Summer Institute in Mathematics and Science
2015	Cooperative International Science and Engineering Internship Intern
2015-2016	Two-time Undergraduate Research and Creative Activities Presentation finalist
2016	Bachelors of Science, UCSB
2018	Masters of Science, UCLA
2021	Leaders in Sustainability Certificate, UCLA IOES
2016-2021	Teaching Assistant, UCLA
2016-2021	Nanoscience Outreach Program, UCLA
2016-2021	Electrochemical Society Student Chapter member and president

Publications and Presentations

1. Seong Shik Kim, David N. Agyeman-Budu, Joshua J. Zak, **Andrew Akash Dawson**, Qizhang Yan, Miguel Cában-Acevedo, Kamila M. Wiaderek, Andrey A. Yankovenko, Yiyi Yao, Ahamed Irshad, Sri R. Narayan, Jian Luo, Johanna Nelson Weker, Sarah H. Tolbert, and Kimberly A. See. Promoting Reversibility of Multielectron Redox in Alkali-Rich Sulfide Cathodes through Cryomilling. *Chem. Mater.* 34(7) 3236-3245(2022)
2. Bingyu Lu, Edgar Olivera, Jonathan Scharf, Mehdi Chouchane, Chengcheng Fang, Miguel Ceja, Lisa E. Pangilinan, Shiqi Zheng, **Andrew Akash Dawson**, Diyi cheng, Wurigumula Bao, Oier Arcelus, Alejandro A. Franco, Xiaochun Le, Sarah H. Tolbert, and

Ying Shirley Meng. Quantitatively Designing Porous Copper Current Collectors for Lithium Metal Anodes. *ACS Appl. Energy Mater.* 4(7)6454-6465 (2021)

3. Terri C. Lin, **Andrew Akash Dawson**, Sophia C. King, Yan Yan, David S. Ashby, Joseph A. Mazzetti, Bruce S. Dunn, Johanna Nelson Weker, and Sarah H. Tolbert. Understanding stabilization in Nanoporous Intermetallic Alloy Snodes for Li-Ion Batteries Using *Operando* Transmission X-ray Microscopy. *ACS Nano.* 14 (11) 14820-14830 (2020)
4. Qizhang Yan, Shu-Ting Ko, Yumin Zhao, Grace Whang, **Andrew Akash Dawson**, Sarah H. Tolbert, Bruce S. Dunn, and Jian Luo. Cryogenic Milling Method to Fabricate Nanostructured Anodes. *ACS Appl. Energy Mater.* 3(11) 11285-11292 (2020)
5. Chun-Han Lai, David S. Ashby, Terri C. Lin, Jonathan Lau, **Andrew Akash Dawson**, Sarah H. Tolbert, and Bruce S. Dunn. Application of Poly(3-hexythiphene-2,5-diyl) as a Protective Coating for High Rate Cathode Materials. *Chem. Mater.* 30 (8) 2589-2599 (2018)
6. "Understanding Lithiation and Sodiation in Porous Alloy Anodes" Oral presentation at the 12th Doctoral Academic Forum in Changchun, China November 2019
7. "Investigating the RedOx Activity and Lithiation of Boron Icosahedrons in the Solid State" Team Science Competition Oral Presentation and the Energy Frontier Research Center Biannual Meeting Washington D.C. July 2019

Chapter 1: Introduction

Lithium-ion batteries are ubiquitous in our everyday lives from cell phones and laptops to vehicles and grid storage. These devices are incredibly important for a sustainable future, one not as reliant on fossil fuels. Lithium-ion batteries have two electrodes, an anode and cathode, and lithium flows from the anode to the cathode, when discharging, and vice versa, when charging. To increase viability of these devices, the energy density must increase. There are two ways to accomplish this, increase the voltage of the battery or the amount of lithium that the electrodes uptake. This dissertation focuses on the second method on both the anode and cathode. The first four chapters focus on stabilization of alloy anodes, and the last chapter examines dodecaborates as an alternative cathode material.

Alloy anodes are materials that alloy with the alkali metal during discharge. Capacity, or charge per gram or volume of material, is used to describe the amount of lithium that a material can accommodate. Alloy anodes like Si, Ge, Sb, Sn, and SbSn have much more capacity than graphite, the anode used in today's batteries. However, due to incorporation of so much lithium, repeated expansion and contraction fracture the particles and delaminate the slurry electrode resulting in irreversible cycling. In our work, nanostructuring the material can increase reversibility because, at the nanoscale, stresses induced at the surface dissipate through the whole particle so that particle fracture is not an issue.

A relatively inexpensive way to nanostructure material is through selective dealloying. In this method, an alloy of a noble metal and sacrificial metal are introduced to an etchant that selectively etches the sacrificial metal while the noble metal re-arranges itself to minimize surface energy. This results in a mesoporous structure with pores on the scale of tens of nanometers. This method is highly tunable with time in etchant, concentration, and temperature

all having an impact on the final structure. For our materials, we create a hierarchical, porous structure by having crystalline domains that are intermetallic and some that are pure sacrificial metal. The dealloying of the intermetallic provides mesopores, and the etching of pure sacrificial domains provides micron scale pores. The large pores allow for electrolyte diffusion, and the small pores are void spaces for the expansion of the material to occur within. This, inward expansion, is preferred to outward expansion because outward expansion disrupts the slurry connectivity. Dealloying creates the structures in the first four chapters of this dissertation.

The first three chapters focus on NP-SbSn. In the first chapter, we use a combination of TXM, XRD, and TEM to understand the structure evolution of NP-SbSn when cycled against lithium. TXM is a powerful tool to image particles while charging and discharging done at the Stanford Synchrotron Radiation Lightsource (SSRL) beamline 6-2c. This *operando* technique provides large fields of views, ~30 μm, with high resolution, ~30 nm. Pouch cells can be used, a practical environment for the material, but the mass loading is much lower for cells used for TXM than actual application. We compare NP-SbSn with previous results on nanoporous tin (NP-Sn). An intermetallic, like SbSn, is beneficial because as one component lithiates, the other can act as a buffer for the expansion. It is fitting that when compared to NP-Sn, NP-SbSn's mesostructure is more preserved. In addition to the benefit of an intermetallic, we found that SbSn cycles through non-crystalline intermediates which may help stabilize the structure further. To test the limits of the structure, we tried cycling NP-SbSn with sodium.

Sodium ion batteries are an alternative to lithium ion batteries. Sodium is more abundant than lithium, making it better economically. However, sodium is much larger than lithium, resulting is more detrimental volume expansion and contraction. Because it is harder to cycle with, we tested NP-SbSn with sodium because it showed very good stability with lithium in

Chapter 2. *Operando* XRD reveals that NP-SbSn still has the benefits of using an intermetallic because Sb and Sn alloy and dealloy at different potentials. TXM confirms that a mesoporous structure is beneficial for sodiation because the bulk SbSn expands more than NP-SbSn. However, unlike with lithiation, sodiation starts to fracture the pore walls, as seen with lithiation of Sn. Chapter 3 focuses on stabilizing NP-SbSn for sodiation by using a surface coating of aluminum oxide. In comparison to bare NP-SbSn, the coated sample does not expand as much and returns closer to its original size after delithiation, and the mesostructure is maintained better with the coating. This chapter also has *operando* TXM for the tenth cycle. We observe that by the tenth cycle, the structure stabilizes. On the macro-scale, there is minimal expansion and contraction on the tenth cycle. On the meso-scale, the pore evolution during cycling is different for the tenth and first cycle. In the first cycle, the pore walls break under lithiation. Whereas, during the tenth cycle, the pore walls expand into the void space created by the pores. This reveals that after initial cycling, the mesostructure also stabilizes. Chapters 1-3 try to understand how structural changes affect behavior on the macro and meso-scale. Chapter 4 aims to understand how mechanism affects structure.

In Chapter 1, we find that NP-SbSn cycles through non-crystalline intermediates which may contribute to its stability. To test how amorphous intermediates can impact macro and meso-scale structure, we use nanoporous antimony (NP-Sb) in Chapter 4. Sb is unique among alloy anodes because it performs as well, if not better, with sodium than with lithium. This is unusual because since sodium is larger than lithium, sodiation forces particles to expand more, which is detrimental to the battery. Literature suggests that this unusual cycling behavior happens because Sb cycles through amorphous intermediates with sodium and crystalline ones with lithium. In this chapter, we explore lithiation and sodiation on NP-Sb. We observe, through

operando XRD that lithiation of NP-Sb has lithiated antimony crystallites forming once lithiation starts, but, with sodiation, there is a period of amorphization before crystalline sodiated antimony appears. With *operando* TXM, sodiation does expand particles more than lithiation, but, in the case of NP-Sb, desodiation results in the particle returning to almost its original size. This is not the case for the SbSn in previous chapters. Also, more fracturing occurs with lithiation even though there is less expansion. In fact, when porous, cracks that do appear during sodiation heal when the material is cycling through its amorphous phases. This suggests that combining structure and mechanism can have added benefits than each by itself. Chapters 1-4 focus on stabilizing alloy anodes for cycling. We learned that the use of an intermetallic, surface coatings, and mechanism all play a role in stabilizing porous structures for cycling.

Chapter 5 centers on increasing the capacity of the cathode. In fact, the capacity limits of cathodes are even worse than anodes. Unlike anodes, cathodes are much more structurally limited. Common lithium iron phosphate, lithium cobalt oxide, nickel manganese cobalt oxide, and nickel manganese aluminum oxide are transition metals with anions surrounding them to stabilize the crystal structure so that lithium has tunnels or layers to intercalate into. However, only the transition metal performs redox, limiting the capacity to ~200 mAh/g. Researchers are trying to increase the capacity through oxygen redox at high voltages and use anions with more accessible HOMO's, like sulfur. However, in this chapter, we use icosahedral, dodecaboranes as a novel platform for cathode materials. These cage-like boron clusters are very stable to temperature and redox. Because of delocalization across the three-dimensional cage, many clusters can have four oxidation states: +1, 0, -1, and -2, and the redox potential is determined by the substituents on the vertices. By accessing and tuning redox, these boron cluster are powerful tools to reimagine cathodes. Here, we react lithium iodo-dodecaborate with hydrogen sulfide to

make boron clusters crosslinked with disulfide bridges. We show reversible, solid state redox of both the sulfur and, for the first time, boron cluster as a cathode. This opens the door to different cathode structures that have been limiting lithium ion battery performance.

Chapter 2: Understanding Stabilization in Nanoporous Intermetallic Alloy Anodes for Li Ion Batteries Using *Operando* Transmission X-ray Microscopy

2.1 Introduction

In recent years, alloying anodes have received tremendous attention due to their high energy density. Though current Li-ion battery (LIB) technology satisfies the need for consumer electronics, it is not ideal for larger applications such as electrical vehicles (EVs) and grid scale storage. Today, approximately 7000 LIBs are installed in a Tesla roadster in order to achieve its quick acceleration and mileage comparable to traditional vehicles that rely on combustion engines

[1] With the high capacity of alloying anodes (at least 2 times more than graphite), the gravimetric and volumetric energy density of LIBs can be significantly increased, leading to smaller, lighter weight, and lower cost battery packs.[2-4]

Among all alloying anodes, Si, Sn and Sb are the most attractive due to their high capacities (4200 mAh/g or 9786 mAh/cm^3, 994 mAh/g or 7246 mAh/cm^3, and 660 mAh/g or 4422 mAh/cm^3, respectively), low market price, and safety.[3,5] Though Si's gravimetric energy density is much higher than Sn and Sb, they all have comparable volumetric densities.[6] The main advantages of Sn and Sb are their metallic properties and high electrical conductivities that are three orders of magnitude higher than metalloid Si.[6,7] Alloying anodes have high energy densities because they go through a multiple electron process as they alloy with Li^+ to form Li-rich phases during charge. Unfortunately, this results in large volume change and significant structural reconstruction as alloying anodes accommodate multiple Li^+ in their lattices.[8-11] In addition, the slow Li^+ diffusion in these materials typically gives rise to a Li-poor/Li-rich core/shell structure during lithiation.[12,13] The volume mismatch in such a core/shell structure can lead to substantial interfacial strain within a particle and lead to crack propagation and capacity fade over time. This issue has limited the potential of alloying anodes in commercial batteries. Recently, small amount of Si (only ~15%) have been incorporated into graphite anodes for EVs to improve the energy densities of the LIBs without sacrificing the lifetime.[14,15] However, commercial devices with high content alloying elements have yet to be realized.

To overcome these challenges, many different nanostructures of alloying anodes such as nanocrystals,[16-19] nanorods,[20-22] and nanoporous networks[23-30] have been made. Nanostructuring is known to 1) improve Li^+ diffusion as the diffusion path length shortens, therefore facilitating a homogeneous lithiation/delithiation process,[13,31] and 2) reduce the strain in the active material

during volume expansion through stress relaxation effects.[32-34] Stress relaxation is observed when the stress response decreases in a nanomaterial under the same amount of strain applied to a bulk specimen.[35,36] In bulk materials, structures typically stay in the strained condition for a finite interval of time, which can cause plastic deformation, leading to dislocation and crack formation. On the other hand, strain can be readily dissipated in nanomaterials, reducing the overall stress response. Among all nanostructures, a nanoporous network composed of a conductive skeleton made of interconnected metallic linkages with high porosity has many advantages because it mitigates agglomeration and the large contact resistance that occur in nanocrystal based materials. Furthermore, nanoporous networks are mechanically flexible and should be able to better accommodate the volume expansion.[32,37,38]

From our previous studies, we have demonstrated the improvement in cycling capabilities and lifetimes using nanoporous materials in comparison to micron-sized particles and nanocrystals.[25,39] Nanoporous tin (NP-Sn) cycled with Li showed cycling stability over 200 cycles with 93% capacity retention (650 mAh/g) while bulk tin (micron-sized powder) lost capacity in less than 10 cycles.[39] This NP-Sn also outperformed tin nanocrystals that showed 80% capacity retention after only 70 cycles.[40] *Operando* TXM revealed that NP-Sn showed much less volume expansion during cycling than bulk Sn, which also cracked upon lithiation. More interestingly, the pores in NP-Sn remained open throughout the entire cycle, allowing for good ion and electrolyte diffusion across the active material. Unfortunately, even though the overall structural stability was improved in comparison to the bulk, some degree of pore wall degradation was observed.

To enhance the mechanical stability of NP-Sn, a secondary metal can be incorporated.[41,42] Intermetallics are attractive because the additional metal can act as a conductive buffer while the other metal alloys with Li^+. Common intermetallics for tin includes SnNi,[43-45] SnCu,[46,47] SnCo,[48,49]

and SbSn;[20,50-57] we note that only SbSn consists of two Li^+ active metals. An inactive component (no capacity contribution) is not ideal because it can significantly reduce both the gravimetric and volumetric energy densities, which are important performance metrics. During lithiation, Sb first alloys with Li^+ at ~ 0.8 V followed by the alloying reaction of Li^+ with Sn (~ 0.7 V).[42] This spreads-out the lithiation process and allows the active material to have a non-reactive component at all times to stabilize the overall structural change and maintain good electrical contact.

Motivated by this previous work, here we report the synthesis of a nanoporous antimony tin (NP-SbSn) powder with good cycling stabilities (595 mAh/g after 100 cycles with 93% capacity retention). These materials show improved structural integrity, as demonstrated from a series of *operando* transmission X-ray microscopy (TXM) studies aimed at understanding how moving from pure Sn to SbSn stabilizes the nanoporous structure.

2.2 Result and Discussion

2.2.1 Materials and Characterization

Selective etching, also known as dealloying, is a simple and facile method commonly used to synthesize nanoporous metals, where a more chemically active element is selectively removed from a dense parent alloy using acidic or basic electrolytes or electrochemical methods. It is an easily scalable synthesis that has been incorporated into our experimental design to meet the important requirements for commercial battery electrode processing. Nanoporous metal powders produced in this manner can be directly integrated into composite electrodes using commercial battery electrode processing lines and are viable for large-scale fabrication of nanostructured materials.

To make NP-SbSn, excess Sn is etched away from the parent alloy $Sb_{20}Sn_{80}$ at.% with 4M HBr. X-ray diffraction (Figure 2.1a) shows that the parent alloy consists of two phases: Rhombohedral intermetallic β-SbSn (*R-3m space group*, JCPDS No. 00-001-0830) and tetragonal tin (I41/*amd space group*, JCPDS No. 01-086-2265), which are in agreement with the phase diagram of Sb-Sn.[58,59] During dealloying, excess Sn reacts with HBr to form hydrogen gas and $SnBr_2$, which is readily soluble in water, leaving only the intermetallic β-SbSn behind and breaking the material up into micron scale pieces.[60] Sn in the intermetallic β-SbSn phase is also etched, but it does not get etched completely because the alloy composition is close to the percolation threshold for dealloying, which is the minimum geometric criterion required for the non-noble atoms to be connected.[61] With this discontinuity, the etchant cannot readily access the non-noble atoms. As diffraction (Fig. 1a) shows, the crystal structure of the as dealloyed NP-SbSn well matches the β-SbSn phase found in the parent alloy, *R-3m space group* (JCPDS No. 00-001-0830). The reaction scheme for this process is proposed in equation 1.

$$\beta\text{-SbSn} + Sn + 2HBr \rightarrow \beta\text{-SbSn} + SnBr_2 + H_2 \qquad \text{(Equation 1)}$$

During dealloying, metal clusters of β-SbSn and porosity form as the surface rearranges in the absence of Sn. The porous structure of NP-SbSn can be seen in the scanning electron microscopy (SEM) images shown in Figures 2.1 b-d. These NP-SbSn powder are constructed from interconnected micron-sized particles with macropores in between due to their random arrangement. At higher magnification, secondary pores can be found on the surfaces of the

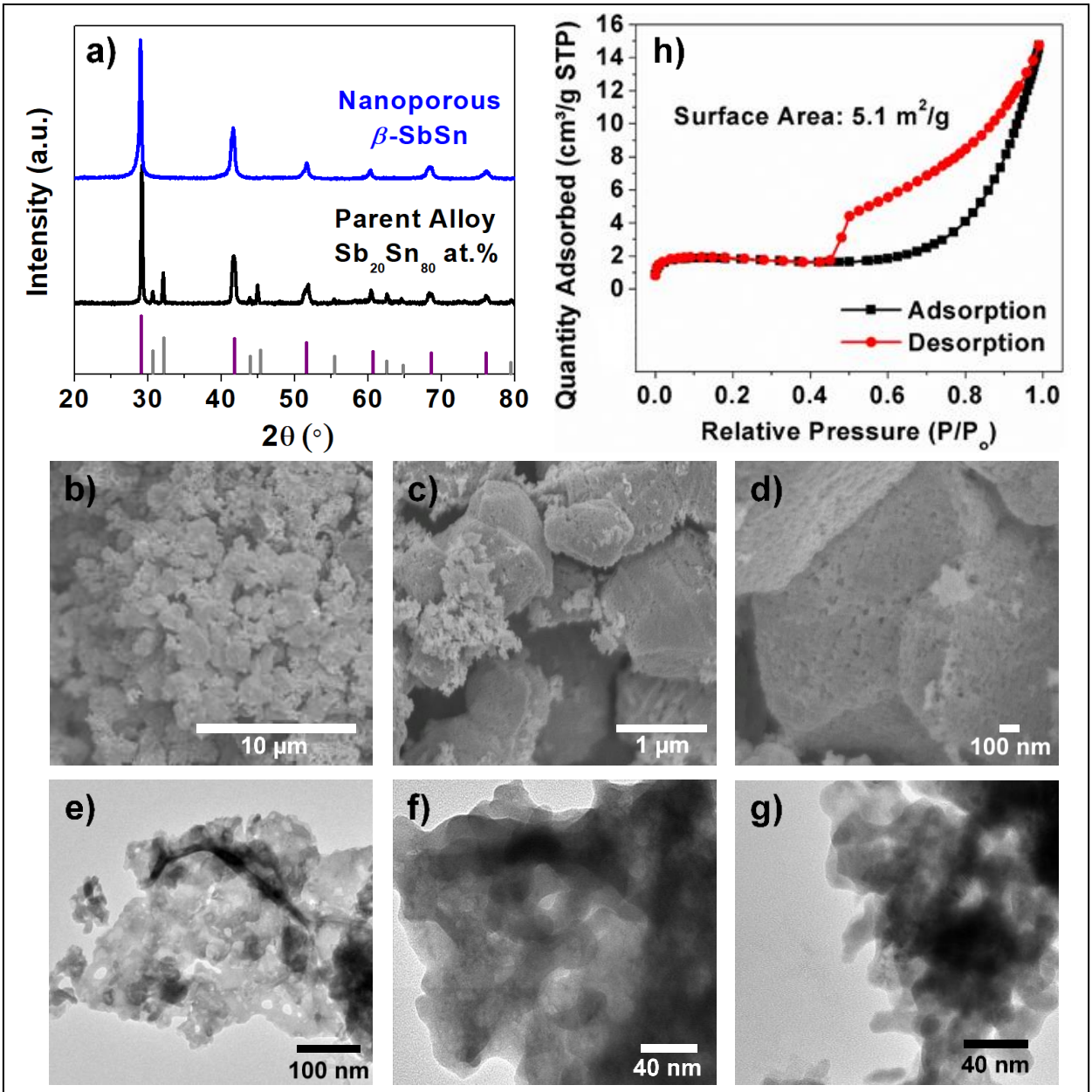

Figure 2.1. a) X-ray diffraction pattern of the parent alloy and the as dealloyed NP-SbSn. Stick patterns of rhombohedral intermetallic *β*-SbSn (*R-3m space group*, JCPDS No. 00-001-0830) and tetragonal tin (I41/*amd space group*, JCPDS No. 01-086-2265) are shown in purple and gray, respectively. **b-d)** SEM images of the NP-SbSn at low and high magnifications. **e-g)** TEM image of the NP-SbSn. **h)** N_2 adsorption/desorption isotherms of the nanoporous SbSn material.

particles. These secondary pores (20-50 nm) and the nanoporous structure are also illustrated in the transmission electron microscopy (TEM) image in Figure 2.1e-g.

The total surface area of NP-SbSn is calculated with the Brunauer-Emmett-Teller (BET) theory from the N_2 porosimetry measurement. NP-SbSn, with a surface area of 5.1 m^2/g, exhibits a type II adsorption-desorption isotherm (Figure 2.1h), representing materials with both macropores and mesopores. Interestingly, the H4 hysteresis observed in the isotherm suggests that these pores could possibly be slit-like.[62] The pore size distribution is also calculated from the Barret-Joyner-Halenda (BJH) models. The average pore size of the mesopores is approximately 30 nm and the calculated fractional porosity from the bulk density and the single point pore volume 24%. These results are consistent with the porosity observed in the SEM and TEM images. X-ray photoelectron spectroscopy (XPS) was carried out to characterize the surface chemical composition of the NP-SbSn. The high resolution XPS spectra of Sb 3d/O 1s and Sn 3d signals are shown in Figure 2.2a. The Sb 3d trace is composed of two sets of the spin-orbit doublets corresponding to Sb $3d_{3/2}$ and Sb $3d_{5/2}$. The signals are fitted and assigned to two chemical states.

The $3d_{3/2}$ peaks at 539.6 eV and 537.2 eV correspond to SbO_2[63] and Sb[64], respectively. Two oxidation states corresponding to Sn and SnO_2 were also fitted in the Sn 3d spectra. The binding energy at 484.7 eV matches metallic Sn[65] while 486.6 eV agrees well with SnO_2.[66] The binding energy of 531 eV in the O 1s spectrum, which overlaps with Sb $3d_{5/2}$, corresponds to the oxygen in SbO_2 and SnO_2.[64,66] This indicates the presence of a thin oxide layer on NP-SbSn surfaces that is likely formed during the DI water washing steps after dealloying. Because zero valent metal can

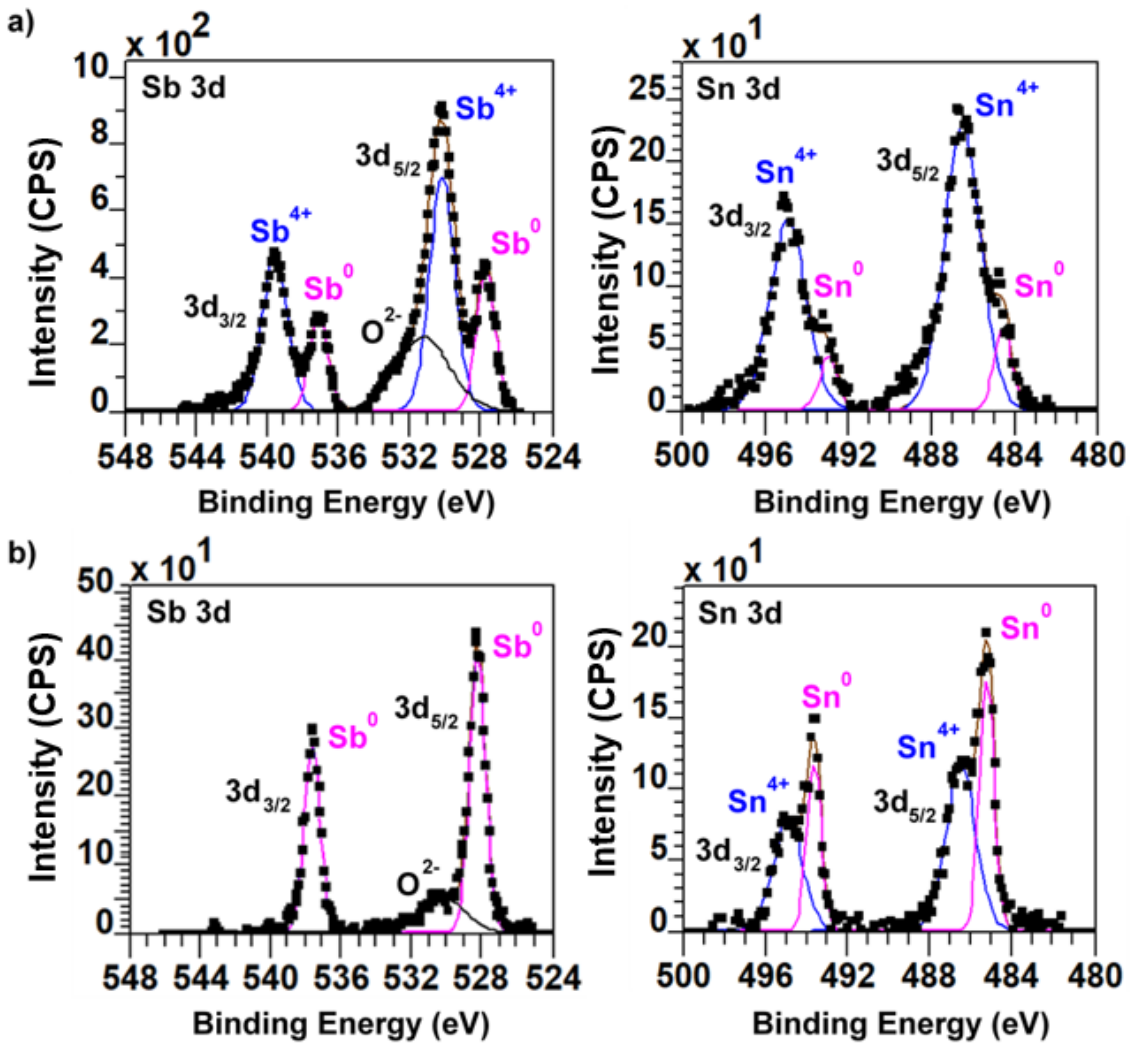

Figure 2.2. X-ray photoelectron spectroscopy of NP-SbSn **a)** before and **b)** after Ar beam etch. Most of the oxide layer was gone after the Ar etch, suggesting that the surface oxide layer is thin.

still be observed, despite the very shallow penetration depth of the XPS experiment, we know that the oxide layer is only a nanometer or two thick. To further confirm that the oxide layer is extremely thin, another set of XPS data were collected after an Ar etch to remove the surface oxide (Figure 2.2b). Similar metallic Sb and Sn peaks were observed before and after etch, but the Sb^{4+} peak at 539.6 eV disappears and the Sn^{4+} from SnO_2 at 486.6 eV dramatically decreases in intensity in the etched XPS spectra.

2.2.2 Electrochemistry

The electrochemical performances of NP-SbSn are investigated in half cells against lithium metal using both cyclic voltammetry (CV) and galvanostatic cycling (GV). The CV curves (Figure

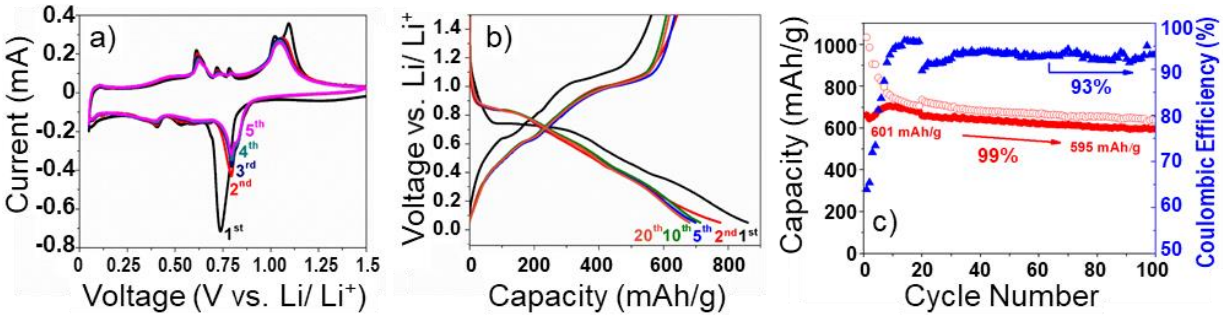

Figure 2.3. a) CV curves for the first five cycles of NP-SbSn at 0.1 mV/s. **b)** Galvanostatic charge and discharge profiles for the 1st, 2nd, 5th, 10th, and 20th cycle of NP-SbSn. **c)** Long term cycle lifetime study of NP-SbSn up to 100 cycles at 0.2C.

2.3a) of the first five cycles were obtained at 0.1 mV/s from 0.05 V-1.5 V. Due to the native oxide layer (SbO_2/SnO_2) and the formation of a solid electrolyte interphase (SEI), a slightly different redox signature is observed in the first cycle.[57,67,68] The reduction peak at 0.75 V corresponds to the reduction of SbO_2 and SnO_2 to Sb and Sn metals. This is followed by a series of alloying reactions, first between Li and Sb, and then between Li and Sn at slightly lower voltages to form the final alloy phases. The reaction pathway for this process is summarized in Equations 2-4. Note that the Li-Sb alloying reaction and electrolyte decomposition both occur around 0.75 V on the

first cycle, resulting in peak asymmetry and a large current response. In subsequent cycles, a doublet at 0.81 V is observed as lithium alloys with Sb to first form the intermediate phase Li_2Sb, and then the lithiated phase Li_3Sb.[16] Starting around 0.6 V, metallic Sn then alloys with lithium through three major phase transitions that form Li_2Sn_5, β-LiSn and finally $Li_{4.4}Sn$.[42,69] Upon reverse reaction, a similar series of peaks can be observed, corresponding to oxidation of Sn (0.6 V, 0.73 V, 0.8 V) and Sb (1.1 V). This series of discrete peaks suggests that the nanoporous material is following the same sequential alloying process as that observed in the bulk.

$$(SbO_2, SnO_2)_{surface} + xLi + xe^- \rightarrow yLi_2O + (Sb, Sn)_{surface} \quad \text{(Equation 2)}$$

$$(Sb, Sn)_{surface} + SnSb + 3Li^+ + 3e^- \leftrightarrow Li_3Sb + Sn \quad \text{(Equation 3)}$$

$$Li_3Sb + Sn + yLi + ye^- \leftrightarrow Li_3Sb + Li_ySn\ (0 \leq y \leq 4.4) \quad \text{(Equation 4)}$$

Figure 2.3b shows the galvanostatic charge and discharge curves of NP-SbSn collected at 0.2C from 0.05 V to 1.5 V. During the first cycle, NP-SbSn delivered 861 mAh/g on discharge and 562 mAh/g on charge. This first cycle irreversibility (65%) can be attributed to the SEI formation and the reduction of the surface oxides on the NP-SbSn. After the formation of a stable SEI on the first cycle, the charge capacity and the coulombic efficiency of the subsequent cycles significantly improved as shown in the GV curves of the 2^{nd}, 5^{th}, 10^{th} and 25^{th} cycle. This stability is further demonstrated in the long-term cycling study (Figure 2.3c) where 595 mAh/g of charge capacity is attained after 100 cycles at 0.25C with 99% capacity retention.

2.2.3 Mechanism of Lithiation

Ex-situ X-ray diffraction (XRD) and high resolution transmission electron microscopy (HR-TEM) with accompanying 2D fast Fourier transforms (FFT) were used to investigate the phases present during lithiation and delithiation in dealloyed NP-SbSn. The starting material is semi-crystalline SnSb, with a small amount of residual Sb, as shown in the bottom pattern in Figure 2.4a and the TEM images in Figure 2.4b. The semi-crystalline nature of the starting phase is expected for a dealloyed material synthesized at room temperature.[70] When cycled to 0.75 V *vs.* Li/Li^+, the crystalline metal peaks disappear and broad peaks corresponding to two lithiated Sb phases appear in the diffraction patterns (Figure 2.4a). These peaks can be indexed to a mixture of nanoscale Li_2Sb and Li_3Sb (JCPDS No. 00-032-0037 and No. 00-004-0791) and indicate demixing of Sb and Sn to form pure lithiated Sb domains. JCPDS stick patterns for β-Sn (JCPDS No. 00-001-0926) are also included, although no distinct Sn peaks can be discerned in the pattern, suggesting that the Sn is mostly amorphous. HR-TEM images (Figure 2.4c) confirm the presence of multiple crystalline Li_2Sb domains and a few diffuse lattice fringes corresponding to semi-crystalline Sn. Moreover, the homogeneous dark contrast observed in Figure 2.4b is replaced by mottled few-nm sized regions of dark and light contrast, corresponding to delithiated and lithiated metal, respectively, as expected in nanosized, phase-separated partly lithiated SbSn. In the fully lithiated sample, X-ray diffraction (Figure 2.4a) shows only broad peaks roughly corresponding to Li_3Sb. The JCPDS stick pattern for $Li_{22}Sn_5$ is also included and may account for some of the broad diffraction intensity, but it is clearly poorly crystalline. In agreement with the diffraction, only lattice planes corresponding to Li_3Sb are observed in TEM images of the fully lithiated sample (Figure 2.4d), again indicating that the lithiated Sn is poorly crystalline. It is not unusual for nanoscale Group IV elements to be amorphous when lithiated.[71,72] In addition, the mottled contrast

seen in Figure 2.4c is replaced by more homogeneous density in Figure 2.4d, as expected for a fully lithiated sample.

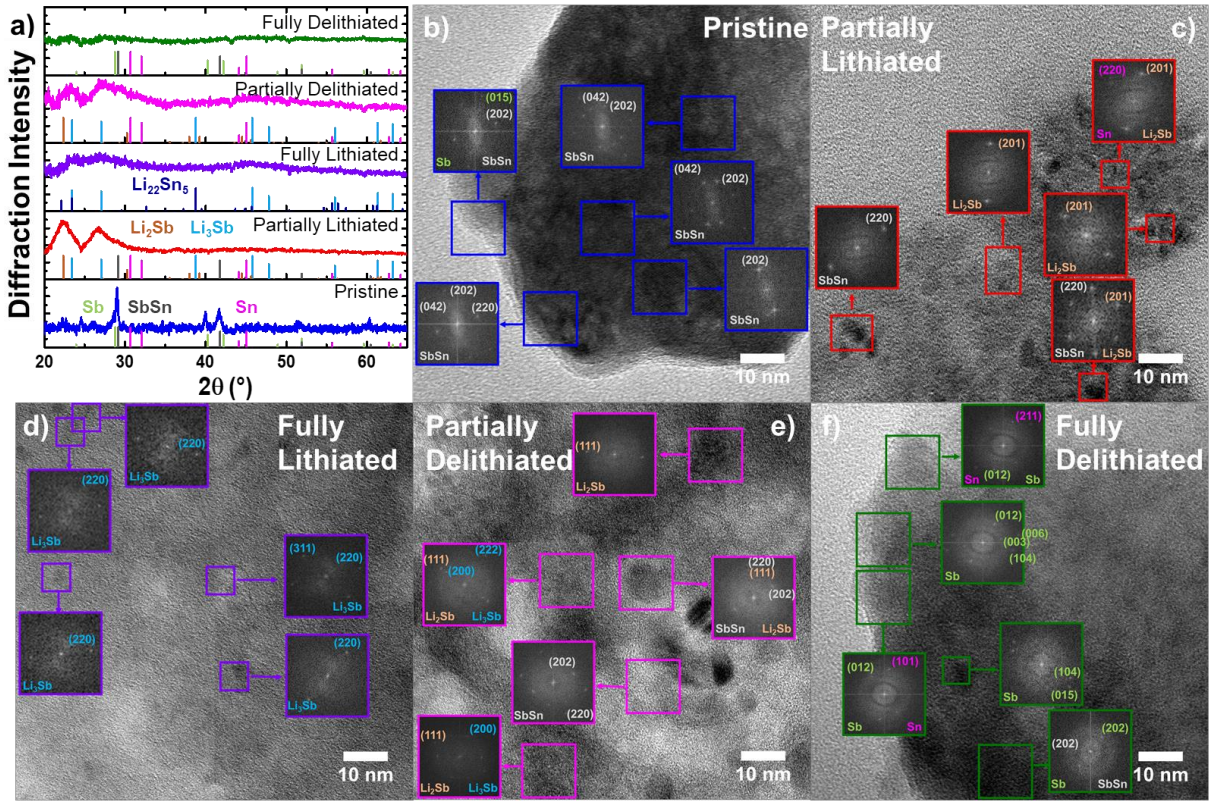

Figure 2.4. a) *Ex-situ* X-ray diffraction collected on NP-SbSn electrodes in various states of charge, ordered bottom to top. Potentials are the same as those described below for panels b-f. For all samples, stick patterns for relevant phases are shown below each pattern. Phase labels are color matched to the stick pattern and are included only near the pattern where that pattern is first included. **c-f)** TEM images and electron diffraction patterns of NP-SbSn electrodes in various states of charge: **b)** pristine/uncycled, **c)** lithiated to 0.75 V *vs.* Li/Li$^+$, **d)** lithiated to 0.05 V *vs.* Li/Li$^+$, **e)** delithiated to 0.8 V *vs.* Li/Li$^+$, and **f)** fully delithiated to 1.45 V *vs.* Li/Li$^+$. For each image, regions that show clear lattice fringes are shown with open squares along with the 2D FFT of that region. Indexing of spots in the FFT is given in the inset. Good consistency is found between XRD and TEM characterization of the samples.

Upon delithiation, similar phases are observed. In the partly delithiated sample, X-ray diffraction (Figure 2.4a) is dominated by Li_3Sb, with additional broad intensity that may correspond to Li_2Sn and poorly crystalline Sn, as expected. The TEM image (Figure 2.4e) also shows a mixture of Li_3Sb and Li_2Sb, as well as a small amount of SbSn, suggesting that the

intermetallic can reform upon Sn delithiation. In Figure 2.4e, contrast is again mottled, indicating a mixture of phase separated lithiated and unlithiated metal. Finally, after full delithiation, TEM (Figure 2.4f) shows a return to a more homogenous dark contrast and diffuse lattice planes corresponding mostly to Sb (the most crystalline phase), but some Sn and SbSn lattice planes are also observed. This suggests that SbSn does not fully reform in the nanoporous network after the first cycle, and subsequent lithiation occurs from a nano-phase separated material. This geometry may be important for the mechanical stability described below and observed using TXM. Interestingly, the material is also much more amorphous than when it started, as indicated by both X-ray diffraction and TEM (Figure 2.4a,f). Indeed, no clear peaks can be observed in the diffraction pattern. This amorphous, nanoscale structure may help with cycling stability, as amorphous phases have been observed to show much better reversibility upon alloying and dealloying than crystalline phases.[73,74]

2.2.4 Operando Transmission X-ray Microscopy Study

To understand the role of Sb in improving stability, *operando* TXM was performed at the Stanford Synchrotron Radiation Lightsource (SSRL) beamline 6-2. Two-dimensional X-ray images were collected continuously during electrochemical cycling on multiple particles to ensure that changes in the particles and pore sizes are representative of the active material. A time interval between images of ten minutes was chosen to provide sufficient data while still preventing beam damage. TXM is a very powerful tool and has been used to study many systems to understand their

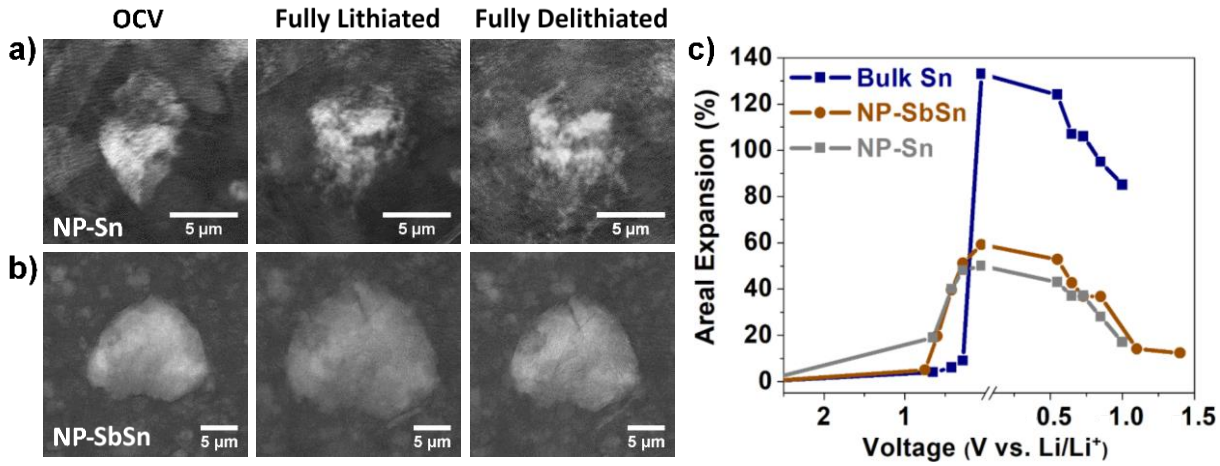

Figure 2.5. Absorption images of **a)** NP-Sn and **b)** NP-SbSn at OCV (left), fully lithiated (middle) and delithiated (right). **c)** Areal expansion of bulk and NP-Sn and NP-SbSn throughout the first cycle. Both NP-Sn and NP-SbSn expand much less than bulk Sn.

morphological and chemical changes during electrochemical cycling.[12,75-78]. From our previous *operando* TXM study on NP-Sn, some structural change (particle shape change) was observed due to pore wall degradation during lithium alloying and dealloying (Figure 2.5a).[39] This occurs despite the fact that NP-Sn demonstrated good cycling capabilities and lower volume expansion than bulk tin (Figure 2.5c). By contrast, particle shape change was not observed in NP-SbSn during cycling, as seen in Figure 2.4b. Indeed, even though NP-SbSn shows slightly larger volume expansion than NP-Sn (59% and 50%, respectively, Figure 5c), the shape of the NP-SbSn particles stayed nearly

invariant throughout the lithiation and delithiation process, despite the formation of a few minor cracks. The presence of a non-reacting component at all potentials apparently prevents dramatic restructuring of the active material and allows the particle to preserve its shape.

In addition to the shape retention, the improved structural integrity can also be seen in the pore size evolution throughout cycling. Pore size distributions were quantified by thresholding images to convert grayscale data to black and white and then creating histograms of the resulting pore areas. With NP-Sn, a significant increase in average pore size was measured by the end of the cycle due to pore wall degradation and the merging of neighboring pores (Figure 2.6a,b). This process is briefly described here, but a detailed analysis can be found in our previous work.[39] When NP-Sn starts to lithiate, the pore size first decreases slightly as the pore walls expanded into the

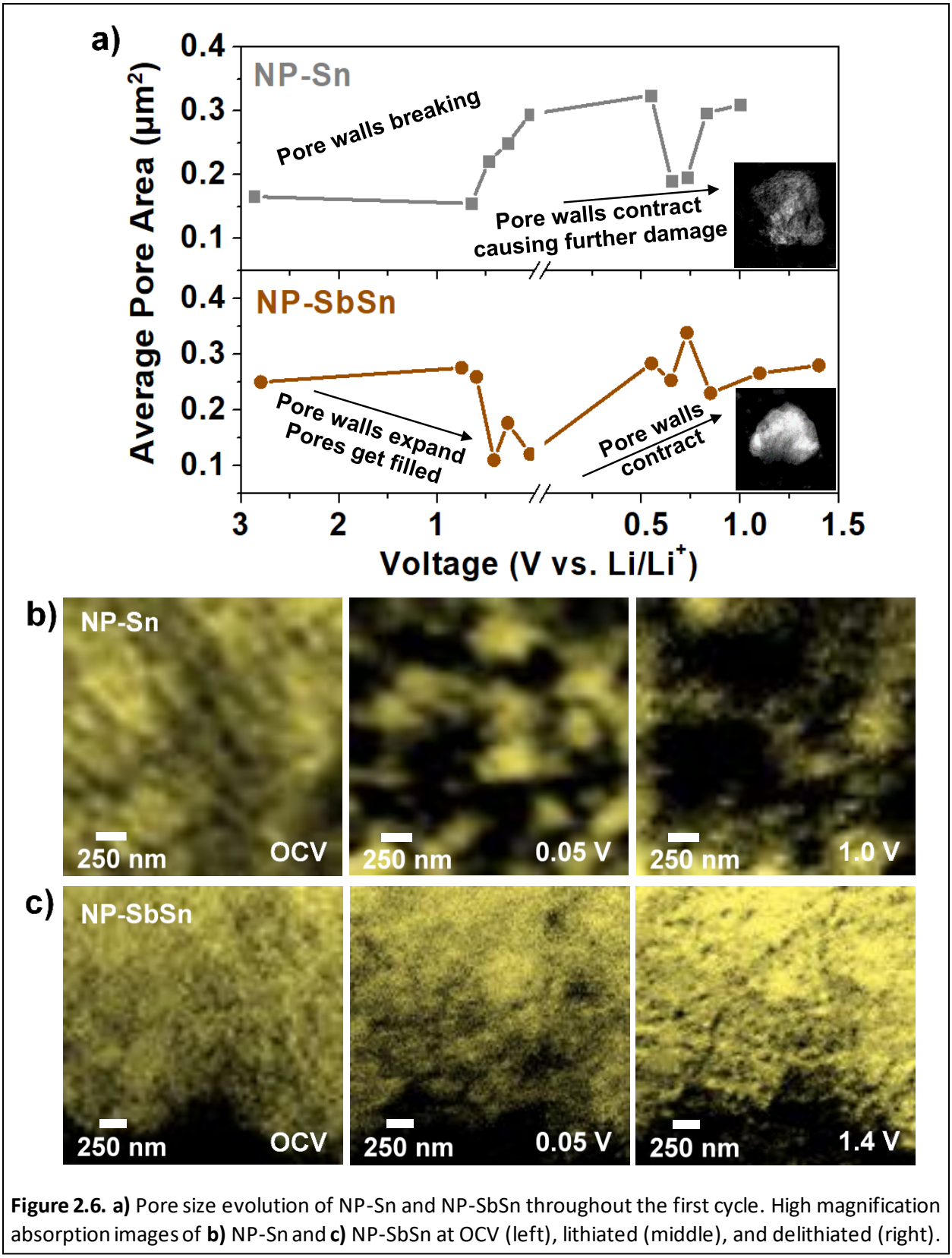

Figure 2.6. a) Pore size evolution of NP-Sn and NP-SbSn throughout the first cycle. High magnification absorption images of **b)** NP-Sn and **c)** NP-SbSn at OCV (left), lithiated (middle), and delithiated (right).

void spaces. As lithiation continued, the pore walls break, causing neighboring pores to

merge (Figure 2.6a). This fragmentation continued throughout delithiation, resulting in a bimodal pores size distribution by the end of the cycle, with a new population of larger pores formed by pore merging observed in addition to the original smaller pores that survive the alloying process.[39]

Very different pore size evolution was observed for the NP-SbSn in this work (Figure 2.6a,c). In NP-SbSn, the pores contracted significantly during lithiation due to extensive pore wall expansion into the pores as lithium alloys with SbSn to form Li_3Sb and $Li_{4.4}Sn$, but they do so predominantly without wall fracture. During delithiation, this allows the pores to grow back to their original size without significantly damaging the porous structure (Figure 2.6a). Figures 6c shows the absorption TXM images of NP-SbSn at OCV, and in the lithiated and the delithiated states. Similar pore size evolution can also be observed for other NP-SbSn particles. In considering the details of the pore size histograms, we observe only one population with an average pore area < 0.5 μm^2 in NP-SbSn at OCV, and as lithiation proceed, the average pore area decreases significantly to approx. 0.1 μm^2. After delithiation, most of the pores return to their original < 0.5 μm^2 size. A very small population of slightly larger pores (1-2.25 μm^2) was found, suggesting some degradation in the pore walls, but nothing on the scale of the large scale pore breakage found in the NP-Sn.

Interestingly, the most dramatic changes in pore size (Figure 2.6a) are associated with lithiation of the Sn (below 0.55 V *vs.* Li/Li^+) rather than lithiation of the Sb (0.6V *vs.* Li/Li^+ and higher). By contrast, the largest changes in overall particle area occur at potentials where the Sb is lithiated (Figure 2.5c). This suggests that lithiation of the Sb to create crystalline Li_3Sb mechanically expands the porous grain, similar to many other main group alloy anodes. Once formed, however, the crystalline Li_3Sb locks the porous network structure in place. The amorphous lithiated Sn that is formed in subsequent steps, is then forced to occupy internal pore volume, rather

than further expanding the overall size of the porous grain. Because the Sn is present and unreactive while Li_3Sb is forming, and Li_3Sb is present and unreactive when Sn is lithiating, the porous network is never fully in flux. Thus the pore walls do not have an easy opportunity to fracture, as they do in the NP-Sn material. We thus hypothesize that it is the combination of a two component system, nanosized domains of each component, and the mechanical flexibility of amorphous Sn and Li_xSn combined with the rigidity of crystalline Li_2Sb and Li_3Sb that allows for such good preservation of the nanoscale pore system upon lithiation and delithiation.

It is important to note that even though the pore size decreased during charge, the pores are still opened in the fully lithiated state. This is critical to allow for uniform lithiation and delithiation, which mitigates crack propagation induced by interfacial strain. The homogeneous lithiation/delithiation process can also be confirmed by the even change in optical density across the particle at each potential, as seen in Figures 2.4. A previous study by Chao and *et al.* showed that although bulk SbSn experiences a more gradual volume expansion compared to bulk Sn due to the two-step electrochemical process, a core-shell structure was still obtained during cycling due to slow lithium diffusion through the bulk solid. This core-shell structure eventually leads to crack formation in the shell.[12]

The mechanical stability of our NP-SbSn was also examined after 36 cycles. Note that *operando* TXM of the 1st cycle and the 36th cycle are taken on different particles/electrodes due to limited beamtime. Precycling of the 36th cycle cell was done in house prior the *operando* TXM

study at SSRL. The particle remains completely intact (Figures 2.7a) and the degree of expansion

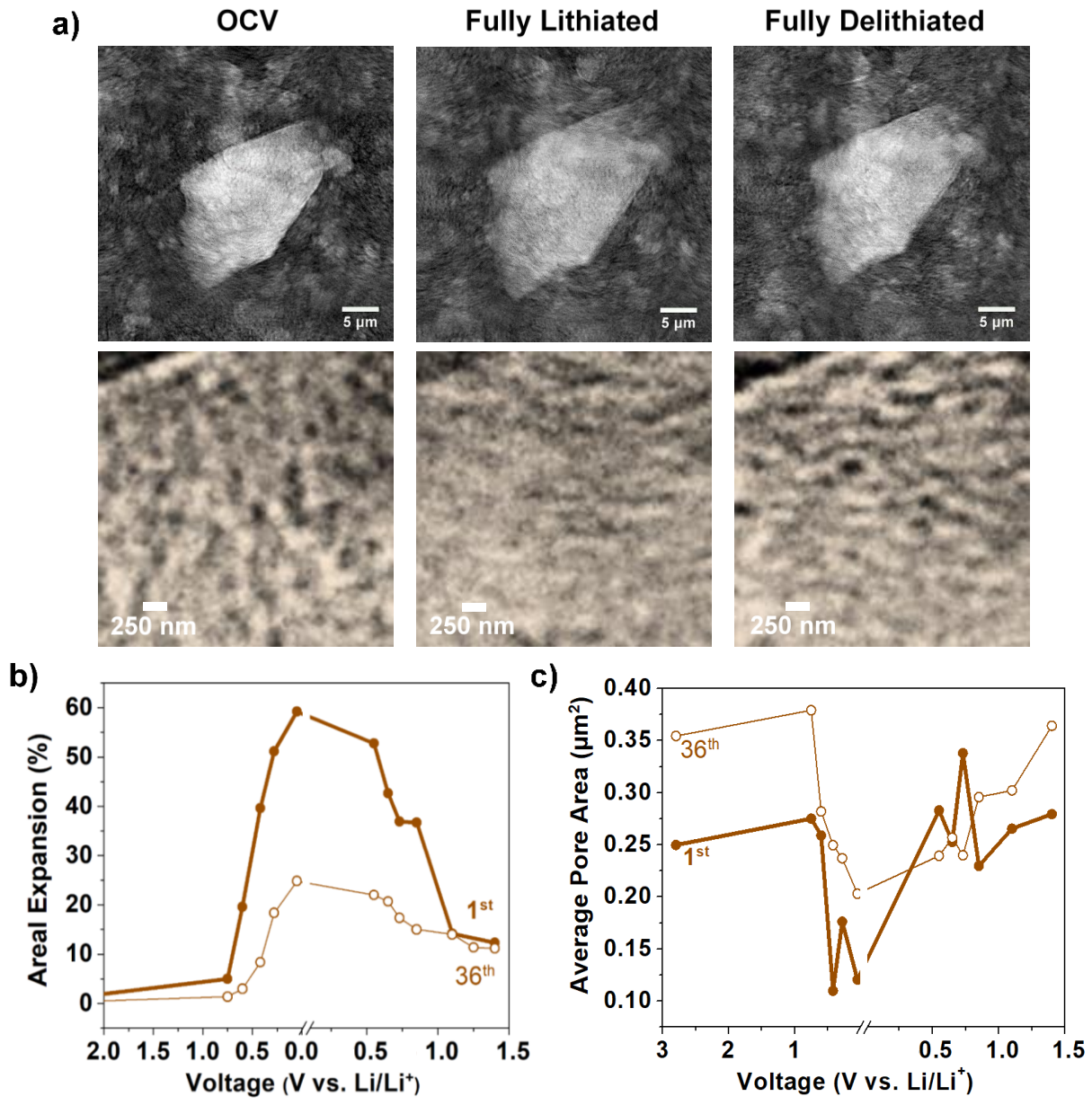

Figure 2.7. a) Low and high magnification absorption images of NP-SbSn during the 36th cycle at OCV, at 0.05 V, and at 1.5 V. The change in areal expansion **(b)** and pore size **(c)** throughout the 36th cycle. After 36 cycles, the NP-SbSn shows less overall grain expansion, but a similar pore size decrease, compared to the original NP-SbSn material.

upon lithiation has decreased to only 25% on the 36th cycle, suggesting that the pore structure in NP-SbSn has been stabilized (Figure 2.7b). The reduced grain expansion on the 36th cycle may be

related to the fact that the NP-SbSn is almost completely amorphous after the first cycle (Figure 2.4), and may lithiate more facilely and with less strain from this amorphous state.

At smaller length scales, the same general trend in pore size evolution is observed in both the 1st and the 36th cycle, with the pores first shrinking and then expanding back to their original size (Figure 2.7c). One difference is that the pore sizes in the 36th cycle are all shifted to slightly larger size than those observed in the first cycle, a result that is likely due to a small amount of pore wall degradation occurring over time. In addition, the pore size changes occur over a broader range of potentials, suggesting that after 36 cycles, both lithiated Sb and lithiated Sn can expand into the pore space, in agreement with the smaller particle level areal expansion (Figure 2.7b). The excellent stability of the pore system after repeated cycling is a testament to the robust nature of the nanoporous architecture.

2.3 Conclusion

In this study, we have successfully synthesized a nanoporous NP-SbSn powder with good cycling stability by taking advantage of the combined structural stability that intermetallic and nanoporous structures provide. These intermetallic 3D conductive materials with open pores were synthesized *via* a one-step dealloying method, and showed a reasonable cycle life with only 1% capacity fade of 100 cycles. *Ex-situ* diffraction and TEM indicate phase separation of the Sb and Sn upon lithiation into nanosized domains, and the Sb forming crystalline domains when lithiated and the Sn forming amorphous structures in all states. *Operando* TXM was used to show that the porous structure of these NP-SbSn materials are well retained upon cycling and show significantly better structural stability than the pure Sn analogue, NP-Sn, which was studied previously. Very little pore wall degradation was observed upon alloying and dealloying with lithium and the

lithiated Sn and Sb appear to expand into the pore spaces, decreasing the pore size. More importantly, the good structural integrity was still observed after 36 cycles, demonstrating the robust nature of the nanoporous network. This work thus provides a direct observation of how intermetallics can interact with a nanoscale structure to further stabilize alloy anodes during charge and discharge. It appears that by having two elements that lithiate and delithiate at different potentials, there is always a non-reactive component stabilizing the nanostructure, and by having a plurality of nanoscale pores, the large volume expansion can be effectively be accommodated. The work further suggests that having one crystalline component (Li_3Sb) and one amorphous component (Li_xSn) can provide an optimal combination of mechanical rigidity and flexibility. This nanoporous intermetallic NP-SbSn with good structural stability, electronic conductivity, and ion/electrolyte diffusion pathways has what appears to be a very favorable architecture to serve as an alloy anode. Given the observed stability with Li^+, these materials can potentially be cycled with even larger ions such as Na^+ and K^+ for alternative energy storage systems.

2.4 Experimental Section

2.4.1 Synthesis

Nanoporous antimony tin (β-SbSn) was made from a one-step chemical dealloying synthesis. A parent alloy of $Sb_{20}Sn_{80}$ at.% was made by melting the stoichiometric amounts of Sb (Alfa Aesar) and Sn (Sigma Aldrich) in a graphite crucible under Ar flow at 700 ^{o} C then cooled to room temperature. To make a homogeneous alloy, the alloy was then heated and cooled several times at 400 ^{o} C. The extra Sn in the parent alloy was then etched away with a 4M HBr (Sigma Aldrich) electrolyte for 21 hr to make the nanoporous structure. After etching, the nanoporous

antimony tin powder is washed with water and ethanol several times. The synthesis of the NP-Sn was reported previously.[24]

2.4.2 Characterization

Powder X-ray diffraction (XRD) was performed on a D8 (Brucker) and a PANalytical X'PertPro diffractometer operating with Cu Kα radiation (λ = 1.5418 Å) with a voltage of 45 kV and a current of 40 mA. XRD patterns were recorded in the range of $10° < 2\theta < 80°$ using a 0.03° step size. Scanning electron microscopy (SEM) images were obtained using a model JEOL JSM-6700F field emission electron microscope with 5 kV accelerating voltage and secondary electron detector configuration. Transmission electron microscopy (TEM) was performed using a FEI Technai G^2 TF20 High-Resolution EM, CryoEM and CryoET operating at an accelerating voltage of 200 kV with a TIETZ F415MP 16 megapixel 4k×4k CCD detector. Nitrogen porosimetry was carried out using a Micromeritics TriStar II 3020. The surface area was calculated from the adsorption branch of the isotherm (between 0.04 – 0.30 P/Po) using the BET model. The pore diameter and pore volume were also calculated from the adsorption branch of the isotherm using the BJH model. XPS analysis was performed using a Kratos Axis Ultra DLD with a monochromatic Al K-α radiation source. The charge neutralizer filament was used to control charging of the sample, a 20 eV pass energy was used with a 0.1 eV step size, and scans were calibrated using the C 1s peak shifted to 284.8 eV. The integrated area of the peaks was found using the CasaXPS software, and atomic ratios were also found using this software. The sample was etched with an Ar beam (raster size 1 mm x 1 mm) at 4 kV for 1 minute

2.4.3 Electrochemical Testing

Carbon-based slurries with 70 wt.% NP-SbSn, 15 wt.% vapor grown carbon fibers (Sigma), and 15 wt.% carboxymethyl cellulose (M_w=250K, Sigma Aldrich) were used for all electrochemical testing. All electrochemical cycling were performed in Swagelok cells with glass fiber separators (Advantec) and 1M $LiPF_6$ (Oakwood Inc) in ethylene carbonate: diethylene carbonate (1:1 vol.%) (Sigma) containing 5% fluorinated ethylene carbonate (TCI America). Samples were cycled against lithium.

2.4.4 Sample Preparation for Ex-Situ X-Ray Diffraction and Transmission Electron Microscopy

Electrodes were cycled in Swagelok cells to the voltage of interest: 0.75 V *vs.* Li/Li^+ for partially lithiated, 0.05 V *vs.* Li/Li^+ for fully lithiated, 0.8 V *vs.* Li/Li^+ for partially delithiated, and 1.5 V *vs.* Li/Li^+ for fully delithiated. The cells were disassembled, and the electrodes were washed, dried, and sealed in Kapton tape for diffraction. The TEM samples were prepared by scraping the electrode off of the copper current collector into dry acetonitrile in a glovebox. These solutions were sonicated for 1 hour before casting onto TEM grids and dried.

2.4.5 Operando Transmission X-ray Microscopy

A different set of carbon-based slurries and cells were made specifically for imaging purposes. These slurries consist of only 25-50 wt.% NP-SbSn, 30-55 wt.% vapor grown carbon fibers, and 20 wt.% carboxymethyl cellulose. Less active material has to be used for TXM imaging in order to reduce the probably of the particles overlapping. Pouch cells were used for the TXM measurements and were sandwiched between two aluminum plates with imaging holes. Be

windows between the plates and cell ensure uniform pressure across the imaging hole and the rest of the cell. Components in the pouch cells include 0.5 mm lithium foil as the counter electrode, Celgard (gift from Celgard) soaked in 1 M $LiPF_6$ in a 1:1 ethylene carbonate/dimethylcarbonate solvent (Sigma Aldrich) with 5% (v/v) fluorinated ethylene carbonate (TCI America) as the electrolyte. For the *operando* TXM study collected on the 36th cycle, the electrode was precycled in a Swagelok cell for 35 cycles, disassembled in an Ar glovebox, and transferred into a pouch cell for the TXM experiment with everything else the same as described above.

Transmission X-ray microscopy of NP-SbSn was performed on beamline 6-2C at the SSRL. 8.95 KeV X-rays were used to perform investigations of electrode morphology at the nano/meso scale. The X-ray energy was chosen to be directly below the Cu K-edge to minimize attenuation from the Cu current collector. The spatial resolution of this microscope is ~30 nm, and the field of view at 8.95 KeV is 38.3 μm. Details regarding the *operando* transmission X-ray microscopy experiments on NP-Sn can be found in our previous study.[39]

During *operando* imaging, the cell was galvanostatically charged and discharged at 0.25C with a VSP potentiostat/galvanostat (Bio-Logic) between 1.4 – 0.05V *vs.* Li/Li^+. A three by three mosaic consists of nine TXM images (38.3 μm x 38.3 μm) were collected at 10-12 regions in the cell. The mosaics were collected continuously (every ten minutes) during cycling. A camera binning of two (four pixels are averaged into one) was used to further improve the image quality. These parameters result in a pixel size of ~35 nm.

2.4.6 Data Processing

X-ray micrographs were processed using an in-house developed software package known as TXM-Wizard.[79] The reference correction was done in TXM-Wizard and the images were further

processed using ImageJ. The reference corrected images were first converted to 8-bit images in ImageJ in order to linearly scale all pixels within the image to 255 different grey-levels (0 being white and 255 being black). A threshold was then applied to the image to differentiate the grey-level of the particle and the background. Since TXM is an absorption measurement, all features of interest are light while background is black. The particle area was then calculated by totaling the number of pixels within the particle after the threshold was applied.

Images used to determine pore size distributions were further processed in ImageJ. The grey scale image described above were thresholded again to convert the 255 grey-levels to black and white. A black and white representation of the porous network provides sharp edges and makes the pore more distinguishable. Black regions (*i.e.* pores) connected by 4 pixels or more were considered individual domains representing individual pores, and the area of each pore was quantified using ImageJ. For this analysis, we magnified the pixelated NP-SbSn grain to find a region where pores could be easily distinguished, then measured the number of pores present and the area of each individual pore at each voltage plateau during lithiation and delithiation. Average pore area and the standard deviation of the pore area were also calculated for each voltage plateau. In addition, a series of histograms with 0.25 μm^2 binning were constructed in an effort to study the change in pore size distribution within NP-SbSn upon cycling.

2.5 References

[1] Cairns, E.J.; Albertus, P. Batteries for Electric and Hybrid-Electric Vehicles. *Annu. Rev. Chem. Eng.* **2010**, *1*, 299-320.

[2] Nitta, N.; Yushin, G. High-Capacity Anode Materials for Lithium-Ion Batteries: Choice of Elements and Structures for Active Particles *Part. Part. Syst. Charact.* **2014**, *31*, 317-336.

[3] Zhang, W.-J. A Review of the Electrochemical Performance of Alloy Anodes for Lithium-Ion Batteries. *J. Power Sources* **2011**, *196*, 13-24.

[4] Zhang, W.-J. Lithium Insertion/Extraction Mechanism in Alloy Anodes for Lithium-Ion Batteries. *J. Power Sources* **2011**, *196*, 877-885.

[5] Li, H.; Shi, L.; Wang, Q.; Chen, L.; Huang, X. Nano-Alloy Anode for Lithium Ion Batteries. *Solid State Ionics* **2002**, *148*, 247-258.

[6] Ma, D.; Cao, Z.; Hu, A. Si-Based Anode Materials for Li-Ion Batteries: A Mini Review. *Nano-Micro Lett.* **2014**, *6*, 347-358.

[7]He, J.; Wei, Y.; Zhai, T.; Li, H. Antimony-Based Materials as Promising Anodes for Rechargeable Lithium-Ion and Sodium-Ion Batteries. *Mater. Chem. Front.* **2018**, *2*, 437-455.

[8]Larcher, D.; Beattie, S.; Morcrette, M.; Edstrom, K.; Jumas, J.-C.; Tarascon, J.-M. Recent Findings and Prospects in the Field of Pure Metals as Negative Electrodes for Li-Ion Batteries. *J. Mater. Chem.***2007**, *17*, 3759-3772.

[9]Huggins, R. A.; Nix, W. D. Decrepitation Model for Capacity Loss during Cycling of Alloys in Rechargeable Electrochemical Systems. *Ionics* **2000**, *6*, 57-63.

[10]Beaulieu, L. Y.; Eberman, K. W.; Turner, R. L.; Krause, L. J.; Dahn, J. R. Colossal Reversible Volume Changes in Lithium Alloys. *Electrochem. Solid-State Lett.* **2001**, *4*, A137-A140.

[11]Park, C.- M.; Kim, J.- H.; Kim, H.; Sohn. H.-J. Li-Alloy Based Anode Materials for Li Secondary Batteries. *Chem. Soc. Rev.* **2010**, *39*, 3115-3141.

[12]Chao, S.-C.; Song, Y.- F.; Wang, C.-C.; Sheu, H.-S.; Wu, H.-C.; Wu, N.-L. Study on Microstructural Deformation of Working Sn and SnSb Anode Particles for Li-Ion Batteries by *in Situ* Transmission X-Ray Microscopy. *J. Phys. Chem. C* **2011**, *115*, 22040-22047.

[13]McDowell, M. T.; Lee, S. W.; Nix, W. D.; Cui, Y. 25th Anniversary Article: Understanding the Lithiation of Silicon and Other Alloying Anodes for Lithium-Ion Batteries.*Adv. Mater.* **2013**, *25*, 4966-4985.

[14]An, S. J.; Li, J.; Daniel, C.; Meyer, H. M.; Trask, S. E.; Polzin, B. J.; Wood, D. L. Electrolyte Volume Effects on Electrochemical Performance and Solid Electrolyte Interphase in Si-Graphite/NMC Lithium-Ion Pouch Cells. *ACS Appl. Mater. Interfaces* **2017**, *9*, 18799-18808.

[15]Louli, A. J.; Li, J.; Trussler, S.; Fell, C. R.; Dahn, J. R. Volume, Pressure and Thickness Evolution of Li-Ion Pouch Cells with Silicon-Composite Negative Electrodes. *J. Electrochem. Soc.* **2017**, *164*, A2689-A2696.

[16]He, M.; Kravchyk, K.; Walter, M.; Kovalenko, M. V. Monodisperse Antimony Nanocrystals for High-Rate Li-Ion and Na-Ion Battery Anodes: Nano *versus* Bulk. *Nano Lett.* **2014**, *14*, 1255-1262.

[17]Tang, X.; Yan, F.; Wei, Y.; Zhang, M.; Wang, T.; Zhang, T. Encapsulating SnxSb Nanoparticles in Multichannel Graphene-Carbon Fibers as Flexible Anodes to Store Lithium Ions with High Capacities. *ACS Appl. Mater. Interfaces*, **2015**, *7*, 21890-21897.

[18]Zhou, D.; Song, W.-L.; Li, X.; Fan, L.-Z.; Deng, Y. Tin Nanoparticles Embedded in Porous N-Doped Graphene-Like Carbon Network as High-Performance Anode Material for Lithium-Ion Batteries. *J. Alloy Compd*. **2017**, *699*, 730-737.

[19]Xu, L. Kim, C. Shukla, A. K. Dong, A. Mattox, T. M. Milliron, D. J. Cabana, J. Monodisperse Sn Nanocrystals as a Platform for the Study of Mechanical Damage during Electrochemical Reactions with Li. *Nano Lett.* **2013**, *13*, 1800-1805.

[20]Wang, Y.; Lee, J. Y. One-Step, Confined Growth of Bimetallic Tin-Antimony Nanorods in Carbon Nanotubes Grown *in Situ* for Reversible Li+ Ion Storage. *Angew. Chem. Int. Ed.* **2006**, *45*, 7039-7042.

[21]Lee, S. H.; Mathews, M.; Toghiani, H.; Wipf, D. O.; Pittman Jr., C. U. Fabrication of Carbon Encapsulated Mono- and Bimetallic (Sn and Sn/Sb Alloy) Nanorods. Potential Lithium-Ion Battery Anode Materials. *Chem. Mater*., **2009**, *21*, 2306-2314.

[22]Li, H.; Zhu, G.; Huang, X.; Chen. L. Synthesis and Electrochemical Performance of Dendrite-Like Nanosized SnSb Alloy Prepared by Co-Precipitation in Alcohol Solution at Low Temperature. *J. Mater. Chem*., **2000**, *10*, 693-696

[23]Park, C.-M.; Jeon, K. Porous Structured SnSb/C Nanocomposites for Li-Ion Battery Anodes. *Chem. Commun*., **2011**, *47*, 2122-2124.

[24]Cook, J. B.; Detsi, E.; Liu. Y.; Liang, Y.-L.; Kim, H.-S.; Petrissans, X.; Dunn, B.; Tolbert, S. H. Nanoporous Tin with a Granular Hierarchical Ligament Morphology as a Highly Stable Li-Ion Battery Anode., *ACS Appl. Mater. Interfaces,* **2017**, *9*, 293-303

[25]Cook, J. B.; Kim, H.-S.; Lin, T. C.; Robbennolt, S.; Detsi, E.; Dunn, B.; Tolbert, S. H. Tuning Porosity and Surface Area in Mesoporous Silicon for Application in Li-Ion Battery Electrodes. *ACS Appl.Mater. Interfaces,* **2017**, *9*, 19063-19073

[26]Liu, J; Kopold, P.; Aken van, P. A.; Maier, J.; Yu, Y. Energy Storage Materials from Nature through Nanotechnology: A Sustainable Route from Reed Plants to a Silicon Anode for Lithium-Ion BatterieS. *Angew. Chem*., **2015**, *127*, 9768-9772.

[27]Detsi, E. Petrissans, X. Yan, Y. Cook, J. B. Deng, Z. L. Liang, Y. L. Dunn, B. Tolbert, S. H. Tuning Ligament Shape in Dealloyed Nanoporous Tin and the Impact of Nanoscale Morphology on its Applications in Na-Ion Alloy Battery Anodes. *Phys. Rev. Materials,* **2018**, *2*, 055404

[28]Jung, D.S.; Ryou, M.-H.; Sung, Y.J.; Park, S.B.; Choi, J.W. Recycling Rice Husks for High-Capacity Lithium Battery Anodes. *Proc. Natl. Acad. Sci. U. S. A.* **2013**, *110*, 12229-12234.

[29]Liu, N.; McDowell, M.T.; Zhao, J.; Cui, Y. Rice Husks as a Sustainable Source of Nanostructured Silicon for High Performance Li-Ion Battery Anodes. *Sci. Rep*., **2013**, *3*, 1919-1926.

[30]Jia, H.; Gao, P.; Yang, J.; Wang, J.; Nuli, Y. Yang, Z. H.Novel Three-Dimensional Mesoporous Silicon for High Performance Li-Ion Battery Anodes. *Adv. Energy Mater*. **2011**, *1*, 1036-1039.

[31]Cortes, F.J.Q; Boebinger, M.G; Xu, M.; Ulyestad A.; McDowell M.T. *Operando* Synchrotron Measurement of Strain Evolution in Individual Alloying Anode Particles within Lithium Batteries. *ACS Energy Lett*., **2018**, *3*, 349-355.

[32]Wang B.; Luo, B.; Li, X.; Zhi, L. B. Wang, B. Luo, X. Li, L. Zhi,The Dimensionality of Sn Anodes in Li-Ion batteries. *Mater. Today Chem*., **2012**, *15*, 544-552.

[33]Tippabhotla, S.K.; Radchenko, I.; Stan, C.V.; Tamura, N.; Budiman, A.S. Enabling the Study of Stress States Using *in-Situ* μSXRD in the Silicon Nanowire Anode during Electrochemical Lithiation in a Specially Designed Li-Ion Battery Test Cell .*Procedia Engineering*, **2017**, *215*, 263-275.

[34]Wu, H.; Cui, Y. Desinging Nanostructured Si Anodes for High Energy Lithium Ion Batteries. *Nano Today*, **2012**, *7*, 414-429.

[35]Obaid, N.; Kortschot, M.T.; Sain, M. Understanding the Stress Relaxation Behavior of Polymers Reinforced with Short Elestic Fibers. *Materials,* **2017**, *10*, 472.

[36]Guiu, F.; Pratt, P.L. Stress Relaxation and the Plastic Deformation of Solids. *Phys. Stat. Sol.* **1964**, *6*, 111-120.

[37]Ying, H.; Han, W.-Q. Metallis Sn-Based Anode Materials: Application in High Performance Lithium-Ion and Sodium-Ion Batteries. *Adv. Sci.*, **2017**, *4*, 1700298.

[38]Brezesinski, T.; Wang, J.; Senter, R.; Brezensinski, K.; Dunn, B.; Tolbert, S.H. On the Correlation between Mechanical Flexibility, Nanoscale Structure, and Charge Storage in Periodic Mesoporous CeO_2 Thin Films. *ACS Nano*, **2010**, *4*, 967-977.

[39]Cook, J.B.; Lin, T.C.; Detsi, E.; Nelson Weker, J. Tolbert, S.H. Using X-Ray Microscopy to Understand How Nanoporous Materials Can Be Used to Reduce the Large Volume Change in Alloy Anodes. *Nano Lett.* **2017**, *17*, 870-877.

[40]Im, H.S.; Cho, Y.J.; Lim, Y.R.; Jung, C.S.; Jang, D.M.; Park, J.; Shojaei, F.; Kang, H.S. Phase Evolution of Tin Nanocrystals in Lithium Ion Batteries. *ACS Nano*, **2013**, *7*, 11103-11111.

[41]Wang, X.-L.; Han, W.-Q.; Chen, J.; Graetz, J. Singe-Crystal Intermetallic M-Sn (M=Fe,Cu,Co,Ni) Nanospheres as Negative Electrodes for Lithium-Ion Batteries. *ACS Appl. Mater. Interfaces,* **2010**, *2*, 1548-1551.

[42]Winter, M.; Besenhard, J.O. Electrochemical Lithiation of Tin and Tin-Based Intermetallics and Composites. *Electrochim. Acta*, **1999**, *45*, 31-50.

[43]Hassoun, J.; Panero, S.; Simon, P.; Taberna, P.L.; Scrosati, B. High-Rate, Long-Life Ni-Sn Nanotructured Electrodes for Lithium-Ion Batteries. *Adv. Mater*. **2007**, *19*, 1632-1635.

[44]Liao, X.-Z.; Ma, Z.-F,; Hu, J,-H.; Sun, Y.-Z.; Yuan, X. SnNi-Deposited Carbonaceous Mesophase Spherule as Anode Material for Lithium Ion Betteries. *Electrochemistry Communications*, **2003**, *5*, 657-661.

[45]Zhang, H.; Shi, T.; Wetzel, D.J.; Nuzzo, R.G.; Braun, P. V. 3D Scaffolded Nickel-Tin Li-Ion Anodes with Enhanced Cyclability. *Adv. Mater*. **2016**, *28*, 742-747.

[46]Xia, Y.; Sakai, T.; Fujieda, T.; Wada, W.; Yoshinaga, H. Flake Cu-Sn Alloys as Negative Electrode Materials for Rechargeable Lithium Batteries. *J. Electrochem. Soc*. **2001**, *148*, A471-A481.

[47]Chen, J.; Yang, L.; Fang, S.; Hirano, S.-I. Synthesis of Mesoporous Sn-Cu Composite for Lithium Ion Batteries. *J. Power Sources* **2012**, *209*, 204-208.

[48]Ke, F.-S.; Huang, L.; Wei, H.-B.; Cai, J.-S.; Fan, X.-Y, Yang, F.-Z.; Sun, S.-G. Fabrication and Properties of Macroporous Tin-Cobalt Alloy Film Electrodes for Lithium-Ion Batteries. *J. Power Sources* **2007**, *170*, 450-455.

[49]Tamura, N.; Fujimoto, M.; Kamino, M.; Fujitani, S. Mechanical Stability of Sn–Co Alloy Anodes for Lithium Secondary Batteries. *Electrochim. Acta* **2004**, *49*, 1949.

[50]Mukaibo, H. Osaka, T.; Reale, P. Panero, S.; Scrosati, B.; Wachtler, M. Optimized Sn/SnSb Lithium Storage Materials *J. Power Sources* **2004**, *132*, 225-228.

[51]Park, M.-S.; Needham, S.A.; Wang, G,-X.; Kang, Y.-M.; Park, J.-S.; Dou, S.-X. Liu, H.-K. Nanostructured SnSb/Carbon Nanotube Composites Synthesized by Reductive Precipitation for Lithium-Ion Batteries. *Chem. Mater*. **2007**, *19*, 2406-2410.

[52]Chen, W.X.; Lee, J.Y.; Liu, Z. The Nanocomposites of Carbon Nanotube with Sb and $SnSb_{0.5}$ as Li-Ion Battery Anodes. *Carbon*, **2003**, *41*, 959-966.

[53]Tang, X.; Yan, F.; Wei, Y.; Zing, M.; Wang, T.; Zhang, T. Encapsulating SnxSb Nanoparticles in Multichannel Graphene-Carbon Fibers as Flexible Anodes to Store Lithium Ions with High Capacities. *ACS Appl. Mater. Interfaces* **2015**, *7*, 21890-21897.

[54]Li, J.; Ru, Q.; Hu, S.; Sun, D. Zhang, B.; Hou, X. Spherical Nano-SnSb/MCMB/Carbon Core–Shell Composite for High Stability Lithium Ion Battery Anodes. *Electrochim. Acta*, **2013**, *113*, 505-513.

[55]Park, C.-M.; Jeon, K.-J. Porous Structured SnSb/C Nanocomposites for Li-Ion Battery Anodes. *Chem. Commun*. **2011**, *47*, 2122-2124.

[56]Li, J.; Pu, J.; Liu, Z.; Wang, J. Wu, W.; Zhang, H.; Ma, H. Porous-Nickel-Scaffolded Tin–Antimony Anodes with Enhanced Electrochemical Properties for Li/Na-Ion Batteries. *ACS Appl. Mater. Interfaces* **2017**, *9*, 25250-25256.

[57]Li, H.; Zhu, G.; Huang, X.; Chen, L. Synthesis and Electrochemical Performance of Dendrite-Like Nanosized SnSb Alloy Prepared by Co-Precipitation in Alcohol Solution at Low Temperature. *J. Mater. Chem*. **2000**, *10*, 693-696.

[58]Okamoto, H. Sb-Sn (Antimony-Tin). *J. Phase Equilib*. **1998**, *19*, 292.

[59]Legendre, B.; Dichi, E.; Vassiliev, V. The Phase Diagram of the In-Sb-Sn System. Z. *Metallkd*. **2001**, *92*, 328.

[60] Gmelin, L. *Hand-Book of Chemistry*, Cavendish Society, London, United Kingdom, Vol.5, **1851**, p.84.

[61]McCue, I.; Benn, E.; Gaskey, B.; Erlebacher, J. Dealloying and Dealloyed Materials. *Annu. Rev. Mater. Res*, **2016**, *46*, 263-286.

[62]Alothman, Z.A. A Review: Fundamental Aspects of Silicate Mesoporous Materials. *Materials*, **2002**, *5*, 2874-2902.

[63]Bodenes, L.; Darwiche, A.; Monconduit, L. Martinez, H. The Solid Electrolyte Interphase a Key Parameter of the High Performance of Sb in Sodium-Ion Batteries: Comparative X-Ray Photoelectron Spectroscopy Study of Sb/Na-Ion and Sb/Li-Ion Batteries. *J. Power Source* **2015**, *273*, 14-24.

[64]Zhou, B.; Sham, E.; Machej, T.;Bertrand, P. Ruiz, P.; Delmon, B. Catalytic Cooperation between MoO_3 and Sb_2O_4 in N-Ethyl Formamide Dehydration I. Preparation, Characterization, and Catalytic Results. *J. Catal.* **1991**, *132*, 157-182.

[65]Baronetti, G.T.; Miguel S.R.; Scelza, O.A.; Castro, A.A. State of Metallic Phase in Pt-Sn/Al_2O_3 Catalysts Prepared By Different Deposition Techniques. *Appl. Cata*. **1984**, *24*, 109.

[66]Süzer, S.; Voscoboinikov T.; Hallam, K.R.; Allen, G.C. Electron Spectroscopic Investigation of Sn Coatings on Glasses .*Anal. Bioanal. Chem*. **1996**, *355*, 654-656.

[67]Ding, L.; He, S.; Miao, S.; Jorgensen, M.R.; Leubner, S.; Yan, C.; Hickey, S.G.; Eychülle, A.; Xu, J.; Schmidt, O.G. Ultrasmall SnO_2 Nanocrystals: Hot-Bubbling Synthesis, Encapsulation

in Carbon Layers and Applications in High Capacity Li-Ion Storage. *Sci. Rep*. **2014**, *4*, 4647-4655.

[68]Yi, Z.; Han, Q.; Li, X.; Wu, Y.; Wang, C.L. Two-Step Oxidation of Bulk Sb to One-Dimensional Sb_2O_4 Submicron-Tubes as Advanced Anode Materials for Lithium-Ion and Sodium-Ion Batteries. *Chem. Eng. J.* **2017**, *315*, 101-107.

[69]Rhode, K.J.; Meisner, R.; Kirkham, M.; Dudney, N.; Daniel, C. *In Situ* XRD of Thin Film Tin Electrodes for Lithium Ion Batteries. *J. Electrochem. Soc*. **2012**, *159*, A294-A301.

[70]Dutta, I.; Carpenter, M.K.; Balogh, M.P.; Ziegelbauer, J.M.; Moylan, T.E.; Atwan, M.H.;Irish, N.P.Electrochemical and Structural Study of a Chemically Dealloyed PtCu Oxygen Reduction Catalyst. *J. Phys. Chem*. **2010,** *114,* 16309-16320.

[71]Wang, J.W.; He, Y.; Fan, F.; Liu, X.H.; Xia, S.; Liu, Y.; Harris, C.T.; Li, H.; Huang, Y.; Mao, S. X.; Zhu, T. Two-Phase Electrochemical Lithiation in Amorphous Silicon. *Nano Lett.* **2013**, *13*, 709-715.

[72]Im, H.S.; Cho, Y.J.; Lim, Y.R.; Jung, C.S.; Jang, D.M.; Park, H.; Shojaei, F.; Kang, H.S. Phase Evolution of Tin Nanocrystals in Lithium Ion Batteries. *ACS Nano*. **2013**, *7*, 11103-11111.

[73]Darwiche, A.; Marino C.; Sougrati, M.T.; Friasse, B.; Stievano, L.; Monconduit, L. Better Cycling Performances of Bulk Sb in Na-Ion Batteries Compared to Li-Ion Systems: An Unexpected Electrochemical Mechanism *J. Am.Chem. Soc.* **2012**, *134*, 20805-20811.

[74]Todd, A.D.W.; Mar, R.E.; Dahn, J.R. Combinatorial Study of Tin-Transition Metal Alloys as Negative Electrodes for Lithium-Ion Batteries. *J. Electrochem*. **2006**, *153*, A1998-A2005

[75]Nelson Weker, J.; Toney, M.F. Emerging *in Situ* and Operando Nanoscale X-Ray Imaging Techniques for Energy Storage Materials. *Adv, Funct. Mater.* **2015**, *25*, 1622.

[76]Nelson Weker, J.; Liu, N.; Andrews, J.C.; Cui, Y.; Toney, M.F. *In Situ* Nanotomography and Operando Transmission X-Ray Microscopy of Micron-Sized Ge Particles. *Energy Environ. Sci.,* **2014**, *7*, 2771-2777.

[77]Chao, S,-C.; Yen, Y.-C.; Song, Y-F.; Chen, Y,-M, Wu, H.-C; Wu, N.-L. A Study on the Interior Microstructures of Working Sn Particle Electrode of Li-Ion Batteries by *in Situ* X-Ray Transmission Microscopy. *Electrochemistry Communications*, **2010**, *12*, 234-237.

[78]Andrews, J.C.; Weckhuysen, B.M. Hard X-Ray Spectroscopic Nano-Imaging of Hierarchical Functional Materials at Work. *ChemPhysChem*. **2013**, *14*, 3655-3666.

[79]Liu, Y.; Meirer, F.; Williams, P.A.; Wang, J.; Andrews, J.C.; Pianetta, P.TXM-Wizard: A Program for Advanced Data Collection and Evaluation in Full-Field Transmission X-Ray Microscopy *J. Synchrotron Radiation* **2012**, *19*, 281-287.

Chapter 3: Using Transmission X-Ray Microscopy to Understand Stability in Nanoporous Antimony Tin for Application as Sodium Ion Battery Anodes

3.1 Introduction

To extend the technology and application of rechargeable batteries beyond personal electronics to electrical vehicles and grid-scale storage, which is critical to the growth of renewable energies, batteries with lower cost and higher energy density need to be developed. Though lithium-ion batteries (LIBs) are currently the system of choice for many portable power applications, sodium-ion batteries (SIBs) have gained tremendous interest in recent years as an alternative because of sodium's earth abundance and similar alkali chemistry.[1,2] SIBs offer a significant cost advantage over LIBs due to the possible shortage and associated price increase in lithium.[3] Though Li^+ and Na^+ undergo comparable electrochemical processes during cycling, the sodium analogue of many materials established for LIBs cannot readily be used in SIBs.[4] This incompatibility is due to the larger ionic radii of Na^+, causing certain reactions to be thermodynamically unfavorable and making it difficult to find host lattices with adequate capacity. [1,4,5] In addition, it results in slower kinetics, and poor cycling stability as it induces significant structural distortion and rearrangements during charge and discharge.[4,6-10]

Today, significant progress has been made on SIB cathodes while the anode side falls far behind. Graphite, which can readily intercalate Li^+, does not intercalate Na^+ well because it is not energetically favorable and therefore results in Na plating.[11-13] However, hard carbon, also known as non-graphitized carbon, has recently demonstrated promising potentials as a SIB anode. [14, 15] With the increased defect sites and layer spacing between the randomly oriented graphene sheets in non-graphitized carbon, Na^+ are allowed to intercalate/ deintercalate reversibly into the system.[13, 16, 17] Though hard carbon is attractive because of its low cost, the specific capacity is

still low (300 mAh/g). To increase the energy density of SIBs, alloying anodes with high theoretical capacities are good candidates.[18-21] Similar to alloying anodes used in LIBs, these anodes also go through a series of alloying reactions with Na^+ to form Na-rich phases during cycling. This multi-electron process offers at least two times more energy density than hard carbon. Among all, Sn and Sb have been widely studied due to their decent theoretical capacities and high electrical conductivities compare to other metals (Bi, Pb), metalloids (Ge, As) and polyatomic nonmetal compounds (P).[22,23] Sn and Sb have electrical conductivities of 9×10^4 Scm^{-1} and 2.5×10^4 Scm^{-1} and theoretical capacities of 847 and 660 $mAhg^{-1}$, respectively.[2,24] Unfortunately, due to a larger ionic radius and much slower kinetics compared to Li^+, these alloying anodes suffer from even more drastic volume changes and shorter lifetime.[25,26]

In order for alloying anodes to survive this tremendous volume change and repetitive structural rearrangement during Na^+ intercalation and deintercalation, mechanically stable architectures have to be designed. The architecture should include a robust yet flexible conductive scaffold with volume expansion accommodation during cycling. This can be achieved by implementing the two of the following strategies: 1) Using an intermetallic (e.g., SbSn) instead of a single metal (e.g., Sn or Sb) as the active material. Intermetallics with two active components that alloy with Na^+ at different potentials are more mechanically stable because at any given voltage there is an unreactive component stabilizing the overall structure.[27-31] 2) Adopting a 3D nanoporous architecture with void spaces for materials to expand into without inducing and accumulating stress. This can therefore reduce the overall volume expansion and structural

damage.[32-39] In addition, nanoporous structures allow for better electrolyte penetration and kinetics, resulting in a more uniform sodiation/desodiation process.

3.2 Synthesis and Characterization

In this work, we have synthesized a nanoporous antimony tin powder (np-SbSn) that resembles a dynamic, conductive skeleton made of interconnected metallic networks and high porosities. This np-SbSn exhibits long cycle lifetimes (85% capacity retention after 100 cycles), decent capacity (434 mAh/g or 1098 mAh/cm^3), and a scalable processing route that involves selective dealloying. In addition to the electrochemical cycling studies, *operando* transmission X- ray microscopy was performed to correlate the structural changes in micron-sized SbSn (b-SbSn) and np-SbSn during volume expansion to their different cycling performance. Together, these methods demonstrate the promise of optimizing both composition and nanoporous architecture for new sodium ion anodes.

A common method to make homogeneous nanoporous metals and intermetallics is through dealloying. Dealloying occurs when an alloy is immersed in an electrolyte under a driving force such that the more reactive component dissolves and the more noble component remains stable in the metallic and intermetallic form, resulting in the formation of a 3D bicontinuous network of randomly interconnected nanochannels and nanostruts.[40,41] The np-SbSn powder used in this study was dealloyed from a $Sb_{20}Sn_{80}$ at.% parent alloy with strong acid HBr. Meanwhile, the micron-sized SbSn particles were synthesized through a solid-state synthesis. The stoichiometric amounts of Sb and Sn metallic powder were melted to make a β-SbSn alloy, which was later ballmilled in liquid nitrogen to break the alloy into powders that consists of micron-sized particles. Figure 3.1a

shows the X-ray diffraction pattern of both np-SbSn and b-SbSn synthesized in house. Both patterns match the JCPD card No.00-033-0118 for rhombohedral (*R-3m*) Stistaite β-SbSn phase with no impurities.

The different morphology of b-SbSn and np-SbSn can be seen from the scanning electron microscopy (SEM) images shown in Figures 3.1b-c and 3.1d-e, respectively. Though both b-SbSn and np-SbSn powders are made of micron-size particles, the morphology of the particles are very different. As expected, dense b-SbSn particles have very smooth surfaces whereas pores ~ 20-50 nm can be seen on np-SbSn's texturous surface, resembling porous structures resulted from

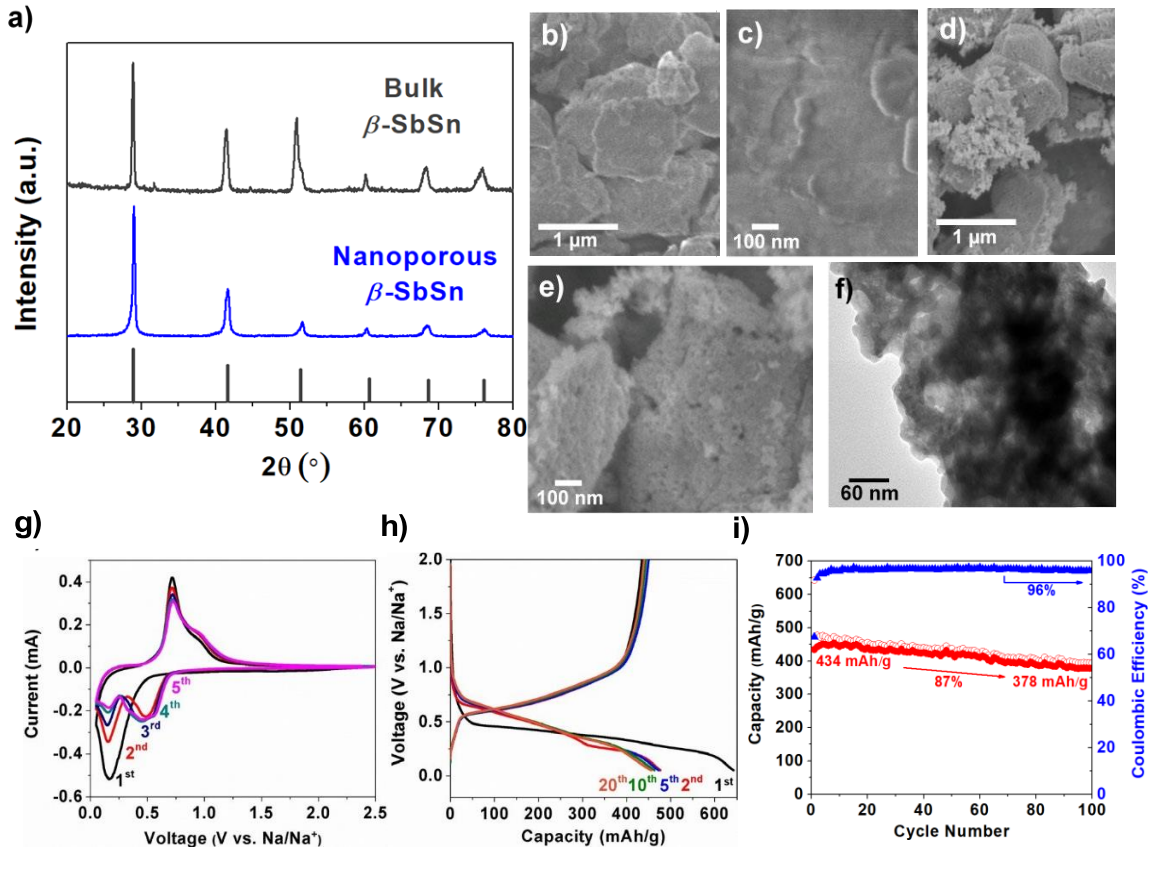

Figure 3.1. Materials Characterization of b- and np-SbSn. a) XRD patterns of b-SbSn in dark gray and np-SbSn in blue. **b-c)** Low and high magnification SEM images of b-SbSn and **d-e)** np-SbSn. f) TEM image of np-SbSn **g)** CV of the first five cycles of np-SbSn cycled at 0.1 mV/s. **h)** Galvanostatic charge and discharge profiles of 1st, 2nd, 5th, 10th and 20th cycle of NP-SbSn. **i)** Longterm cycling of np- SbSn

dealloying. The distinct ligaments and pores can be seen in the transmission electron microscopy images in Figure 3.1f.

The type II isotherm measured from N_2 porosimetry suggests that np-SbSn consists of both

mesopores and macropores.[42] The mesopores represent the intrinsic porosity/nanochannels in the np-SbSn particles while the macropores are originated from the spaces between the randomly arranged micron-size np-SbSn particles as seen from the lower magnification SEM images.

Figure 3.1h shows the galvanostatic charge and discharge profiles of the 1st, 2nd, 5th, 10th and 20th cycle of np-SbSn at 0.2C. During the first discharge, a low 67% coulombic efficiency as well as a lower voltage plateau at 0.5 V is observed compared to the subsequent cycles. This is in good agreement with the surface oxide reduction and SEI formation observed in the CV curves. During the first cycle, the charge capacity is 643 mAh/g and the discharge capacity is 434 mAh/g. After the stable SEI forms, these np-SbSn showed great stability in the subsequent cycle with 92% coulombic efficiency ($Capacity_{discharge}$ = 477 mAh/g and $Capacity_{charge}$ = 442 mAh/g). Even after 100 cycles, 85% of charge capacity was retained. The long term cycling study performed at a rate of 0.2C can be found in Figure 3.1i. In stark contrast to the performance of np-SbSn, b-SbSn died after three cycles as a result of crack propagation and poor electrical contact. This is one of the few pure SbSn anodes that has demonstrated such stability.[43] Most studies still rely on carbon for extra mechanical support and electrical conductivity.[44-46] This conductive bicontinuous scaffold of np-SbSn offers great advantage over other carbon composites as it is flexible to accomodate volume change and favorable for the electron and mass transportation during cycling. These np- SbSn also cycled much better than the nanoporous tin (np-Sn) demonstrated in our previous study, signifying the enhanced structural stability from the intermetallic.

To understand the electrochemical reactions occurred during sodiation and desodiation of np-SbSn, cyclic voltammetry (CV) was performed between 0.05V and 2V with a scan rate of 0.1 mV/s. The first five cycles are shown in Figure 3.1g. During the first cathodic scan, the broad peak from 0.5V- 0.05V corresponds to the formation of stable solid electrolyte interphase and the

reduction of surface oxides (SbO_2 and SnO_2) to metallic Sb and Sn follow by the alloying reactions of Sb and Sn metals with Na^+.[47-49] During the anodic scan, two peaks are observed at 0.71V and 0.9 V and can be attributed to the desodiation process of sodiated Sb and sodiated Sn to metallic Sb and Sn. [50, 51, 52] The typical reaction pathway can be explain by Equation 1-4.[6, 53] In the subsequent cycles, only redox pairs related to the sodiation and desodiation of Sb and Sn metals can be observed, indicating a stable oxidation/ reduction process with good reversibility.

$(SbO_2, SnO_2)_{surface} + xNa + xe^- \rightarrow yNa_2O + (Sb, Sn)_{surface}$ (Equation 1)

$SnSb + xNa^+ + xe^- \rightarrow Sn + Na_xSb$ (Equation 2)

$Sn + Na_xSb + (3-x)Na^+ + (3-x)e^- \rightarrow Sn + Na_3Sb$ (Equation 3)

$Na_3Sb + Sn + 3.75Na + 3.75e^- \leftrightarrow Na_3Sb + Na_{3.75}Sn$ (Equation 4)

3.2 Operando X-Ray Diffraction

However, due to the nanoscale properties of the np-SbSn, *operando* X-ray diffraction was done at Stanford Sychrotron Radiation Lightsource (SSRL) beamline 11-3 to uncover the mechanism of sodiation of nanoscale SbSn. Figure 3.2 shows the results of these measurements. In the beginning, we observe peaks at ~2.05 and 2.92 A^{-1} associated with rhombohedral (*R-3m*) Stistaite *β*-SbSn. As sodiation occurs, this peak disappears and no other peaks appear. This is reasonable because Sb sodiates through amorphous intermediates, and it is common for Group IV elements, like Sn, to be amorphous.[54,55] At the end of sodiation, small crystalline Na_3Sb (JCPD No. 00-004-0724) peaks emerge at ~1.50, 2.40, and 2.35 A^{-1} indicating that the fully sodiated antimony phase separates from sodiated Sn. [6,56] As desodiation begins, the Na_3Sb peaks persist. Therefore,

Sn desodiates before Sb, and Na_3Sb stay separated. These peaks are present for much of the desodiation, but eventually they fade because Na_3Sb desodiates. This confirms that Sb and

Sn alloy at different potentials allowing one component to buffer the expansion of the other, a key to intermetallic stabilization of alloy anodes.[53,57]

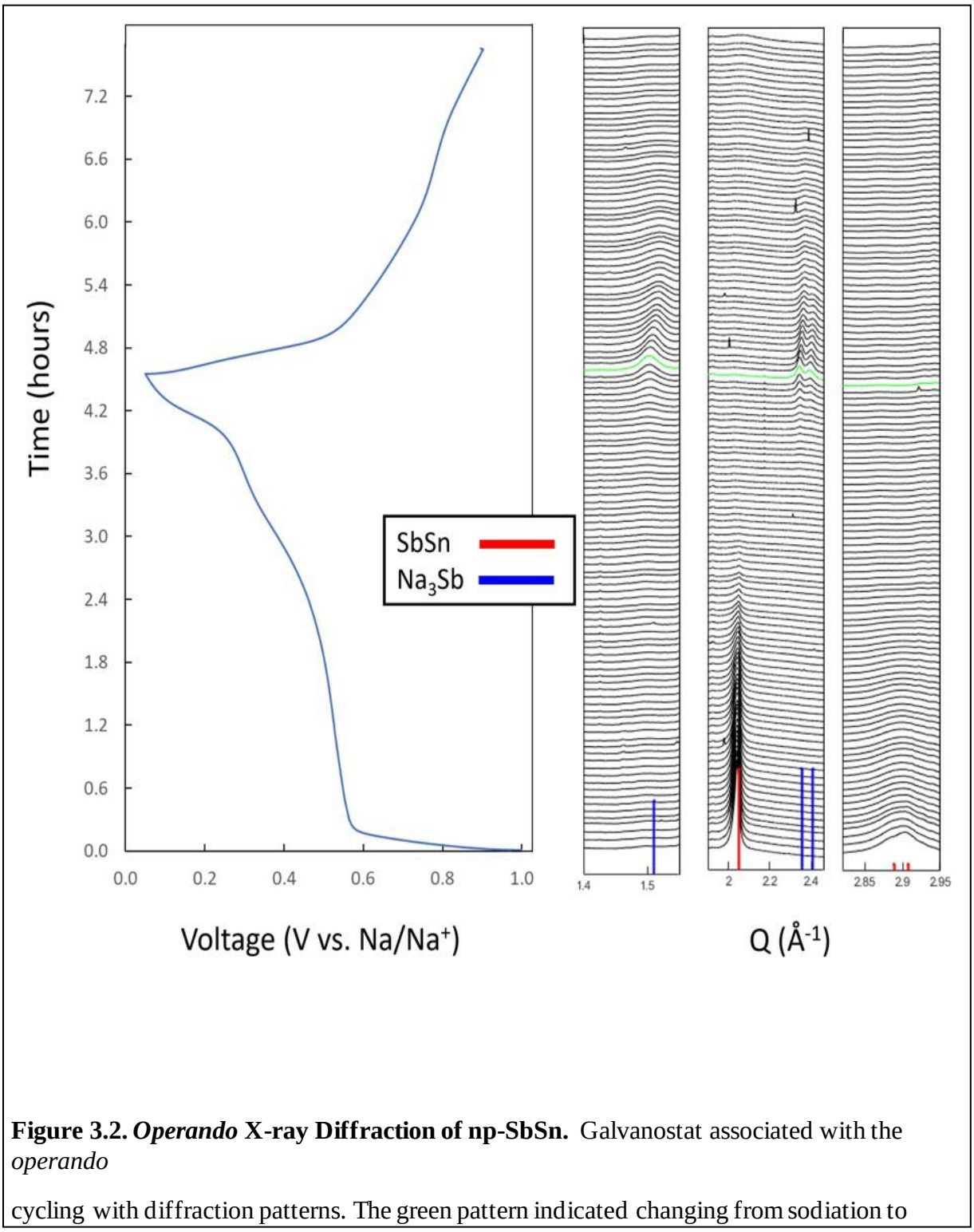

Figure 3.2. *Operando* X-ray Diffraction of np-SbSn. Galvanostat associated with the *operando*

cycling with diffraction patterns. The green pattern indicated changing from sodiation to

3.3 Operando Transmission X-Ray Microscopy

To develop a structural understanding of the origins of np- and b-SbSn's markedly different cycling performance with sodium, *operando* transmission X-ray microscopy (TXM) was performed at SSRL beamline 6-2C to monitor the morphological changes in bulk and nanoporous SbSn during cycling. The cells used for TXM have lower mass loadings than typical cells so there is more carbon contribution for the galvanostat. Figure 3.3a and 3.3b shows the 2D adsorption images of b-SbSn and np-SbSn, respectively, at open circuit voltage (OCV), 0.05V

(sodiated state) and 2V (desodiated state). During cycling, severe crack propagation was observed in b-SbSn while none were found in np-SbSn. Crack propagation is detrimental to the cycling performance as it can cause the particles to lose electrical contact with the slurry matrix and current collector.[58] Moreover, crack formation introduces unprotected surfaces to the electrolyte. If new SEI continues to grow in every cycle, the amount of available active material and Li^+ will be reduced, leading to capacity loss.[59] As expected, b-SbSn expanded more than np- SbSn as shown in Figure 3.3c. Over a hundred percent (104 %) of areal expansion was calculated for b-SbSn while np-SbSn only expanded 68% with no physical disintegration. The outline of

np-SbSn particle stayed nearly identical throughout charge and discharge. At the fully desodiated state, np-SbSn almost contracted back to its original size (only 24% expanded) and b-SbSn remained more expanded (54% expanded). Np-SbSn's good structural stability can be attributed to the nanporous structure, where the diffusion of Na^+ is largely improved and therefore enabling a homogeneous sodiation/desodiation process. This is confirmed from the uniform optical density observed across the particle throughout the charge and discharge process.

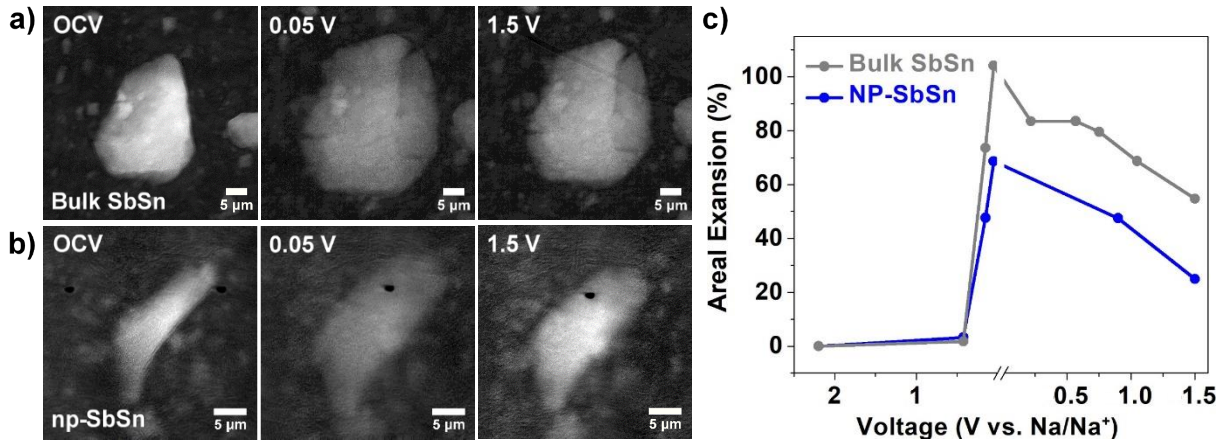

Figure 3.3. Adsorption images of b- and np-SbSn collected during operando TXM study. **a)** b- and **b)** np-SbSn collected at OCV, fully sodiated and desodiated state. **c)** Percent Areal expansion calculation of b- and np-SbSn throughout the whole cycle.

In addition to the overall structural change, the evolution of porosity in np-SbSn was also studied. Figure 3.4b-d shows the high magnification 2D TXM images of np-SbSn at OCV, sodiated and desodiated state. Throughout discharge, the pores had grown larger compare to the pores in pristine np-SbSn. Even though the pores slightly contracted by the end of the first cycle, they are still larger than at OCV. To quantitatively analyze the change in pore size, a series of histograms (number of pores versus individual pore area) were constructed. These histograms were then used to calculate the average pore area at each voltage plateau shown in Figure 3.4a. The trend depicted in Figure 3.4a is in good agreement with the TXM images and suggests that the pore wall slightly degraded during sodiation as the pore wall expands. This evolution is similar to what we had previously found in our *operando* TXM study on np-Sn during lithiation and delithiation but in a

less drastic manner.[36] The reduced amount of damage suggest that np-SbSn is more mechanically stable and can therefore cycle better with Na^+. Figure 3.4e-g are the pore size distributions for the TXM images, Figure 3.4b-d. Most pores are still 0-1 μm^2. Therefore, the average pore area shown in Figure 3.4a is the result of a few large pores dominating the distribution. Certain ligaments in the porous structure may not be as structurally sound as others resulting in fracture and pore size increases. Whereas, the majority of ligaments offer structural stability while cycling and keep the pore area increase to a minimum. Despite the degradation in the porous structure, pores remained open throughout cycling. This is critical in allowing for good electrolyte penetration and

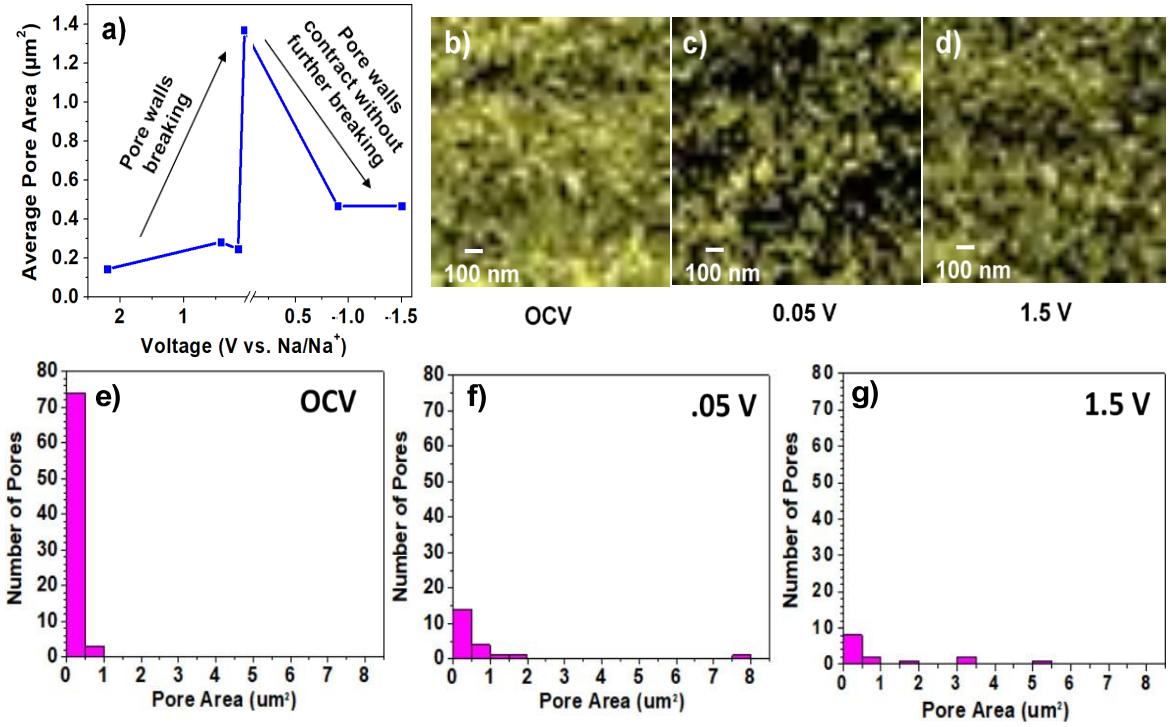

Figure 3.4. The pore wall evolution study of np-SbSn a) Change in pore size throughout cycling and adsorption images of the pores at **b)** OCV, **c)** 0.05 V and **d)** 1.5 V. Pore size distributions at **e)** OCV, **f)** 0.05 V and **g)** 1.5 V

homogeneous sodiation/desodiation, which avoids the formation of a core shell structure and the lattice mismatch between the Na-rich and Na-poor phase that results in interfacial strain and crack

formation.

The good cycling performance of this np-SbSn system compared to the b-SbSn and the np- Sn we have previously synthesized,[39] is attributed to the spread out sodiation voltage of intermetallic SbSn and its nanoporous architecture. Through *operando* TXM imaging, we have shown that the combination of these tools increases the structural stability of anode particles. The unique, interconnected, granular morphology accommodates the large volume changes taking place during sodiation and preserves the electrical contact with the macroporous carbon fiber electrode network even in the sodiated state, allowing for good electrolyte penetration to all active sites, and the intermetallic buffering prevents severe damage to the porous structure with most pores staying small throughout cycling. With this np-SbSn, we have successfully delivered 430 $mAhg^{-1}$ with 85% capacity retention after 100 cycles, which out-performs the NP-Sn we have

previously synthesized (550mAhg^{-1} initial capacity, but only 50% capacity retention after 90 cycles).

3.4 References

[1] Hwang, J.-Y.; Myung, S.-T.; Sun, Y.-K. Sodium-ion batteries: present and future. *Chem. Soc. Rev.* **2017**, *46*, 3529-3614

[2] Kang, H.; Liu, Y.; Cao, K.; Zhao, Y.; Jiao, L.; Wang, Y.; Yuan, H. Update on anode materials for Na-ion batteries. *J. Mater. Chem. A* **2015**, *3*, 17899-17913.

[3] Vaalma, C.; Buchholz, D.; Weil, M.; Passerini. S. A cost and resource analysis of sodium-ion batteries. *Nat. Rev. Mater.* **2018**, *3*, 18013.

[4] Nayak, P. K.; Yang, L.; Brehm, W.; Adelhelm, P. From Lithium-ion to sodium-ion batteries: Advantages, challenges and surprises. *Angew. Chem. Int. Ed.* **2017**, *57*, 102-120.

[5] Balogun, M.-S.; Luo, Y.; Qiu, W.; Liu, P.; Tong, Y. A review of carbon materials and their composites with alloy metals for sodium ion battery anodes. *Carbon* **2016**, *98*, 162-178.

[6] Xie, H.; Tan, X.; Luber, E. J.; Olsen, B. C.; Kalisvaart, W. P.; Jungjohann, K. L.; Mitlin, D.; Muriak, J. M. β-SbSn for sodium ion battery anode: Phase transformations responsible for enhanced cycling stability revealed by in situ TEM. *ACS Energy Lett.* **2018**, *3*, 1670-1676.

[7] Liang, Y.; Lai, W.-H.; Miao, Z.; Chou, S.-L. Nanocomposite materials for the Sodium-ion battery: A review. *Small* **2018**, *14*, 1702514.

[8] Xie, H.; Kalisvaart, W. P.; Olsen, B. C.; Luber, E. J.; Mitlin, D.; Muriak, J. M. Sn-Bi-Sb alloys as anode materials for sodium ion batteries. *J. Mater. Chem. A* **2017**, *5*, 9661-9670.

[9] Wang, L. P.; Yu, L.; Wang, X.; Srinivasan, M.; Xu, Z. J. Recent developments in electrode materials for sodium-ion batteries. *J. Mater. Chem. A* **2015**, *3*, 9353–9378.

[10] Slater, M. D.; Kim, D.; Lee, E.; Johnson, C. S. Sodium-Ion Batteries. *Adv. Funct. Mater.* **2013**, *23*, 947-958.

[11] Ge, P.; Fouletier, M. Electrochemical intercalation of sodium in graphite. *Solid State Ionics* **1988**, 28–30, 1172-1175.

[12] Doeff, M. M.; Ma, Y.; Visco, S. J.; DeJonghe, L. C. Electrochemical insertion of sodium into carbon. *J. Electrochem. Soc.* **1993**, *140*, L169-L170.

[13] Wen, Y.; He, K.; Zhu, Y.; Han, F.; Xu. Y.; Matsuda, I.; Ishii, Y.; Cumings, J.; Wang, C. Expanded graphite as superior anode for sodium-ion batteries. *Nat. Commun.* **2014**, *5*, 4033.

[14] Irisarri, E.; Ponrouch, A.; Palacin, M. R. Review – Hard carbon negative electrode materials for sodium-ion batteries. *J. Electrochem. Soc.* **2015**, *162*, A2476-A2483.

[15] Ponrouch, A.; Dedryvere, R.; Monti, D.; Ateba, J. M.; Croguennec, L.; Masquelier, C.; Johansson, P.; Palac´ın, and M. R. Towards high energy density sodium ion batteries through electrolyte optimization. *Energy Environ. Sci.* **2013**, *6*, 2361-2369.

[16] Stevens, D. A.; Dahn, J. R. The mechanisms of lithium and sodium insertion in carbon materials. *J. Electrochem. Soc.* **2001,** *148*, A803–A811.

[17] Wang, Y.-X.; Chou, S.-L.; Liu, H.-K.;Dou, S.-X. Reduced graphene oxide with superior cycling stability and rate capability for sodium storage. *Carbon* **2013**, *57*, 202–208.

[18] Zhang, H.; Hasa, I.; Passerini, S. Beyyond Insertion for Na-Ion Batteries: Nanostructured Alloying and Conversion Anode Materials. *Adv. Ener. Mater.* **2018**, 8, 1072582

[19] Luo, W.; Shen. F.; Bommier, C.; Zhu, H.; Ji, X.; Hu, L. Na-ion battery anodes: Materials and electrochemistry. *Acc. Chem. Res.* **2016**, *49*, 231-240.

[20] Ying, H.; Han, W.-Q. Metallic Sn-based anode materials: Application in high-performance lithium-ion and sodium-ion batteries. *Adv, Sci.* **2017**, *4*,1700298.

[21] Kim, Y.; Ha, K.-H.; Oh, S. M.; Lee, K. T. High-capacity anode materials for sodium-ion batteries. *Chem. Eur. J.* **2014**, *20*, 11980-11992.

[22] Mou, H.; Xiao,W.; Miao, C.; Li, R.; Yu, L. Tin and Tin Compound Materials as Anodes in Lithium-Ion and Sodium-Ion Batteries: A Review. *Front. Chem.* **2020**, 8, 1-10.

[23] Sarkar, S.; Peter, S.C. An Overview on Sb-Based Intermetallics and Alloys for Sodium-Ion batteries: Trends, Challenges, and Future Prospects from Material Synthesis to Battery Performance. *J. Mater. Chem. A.* **2021**, 9, 5164-5196

[24] He, J.; Wei, Y.; Zhai, T.; Li, H. Antimony-based materials as promising anodes for rechargeable lithium-ion and sodium-ion batteries. *Mater. Chem. Front.* **2018**, *2*, 437-455.

[25] Wang, J. W.; Liu, X. H.; Mao, S. X. Huang, J. Y. Microstructural evolution of tin nanoparticles during in situ sodium insertion and extraction. *Nano Lett.* **2012**, *12*, 5897-5902.

[26] Wang, J.; Eng, C.; Chen-Wiegart, Y.-C. K.; Wang, J. Probing three-dimensional sodiation-desodiation equilibrium in sodium-ion batteries by in situ hard X-ray nanotomography. *Nat. Commun.* **2015**, *6*, 7496.

[27] Mohammad, I.; Blondeau, L.; Foy,E.;Leroy, J.; Leroy, E.; Khodja, H.; Gauthier, M.

Nanostructured Intermetallic InSb as a High-Capacity and High-Performance Negative Electrode for Sodium-Ion Batteries. *Sus. Energ. Fuels.* **2021**, 5, 3825-3835.

[28] Xie, H.; Tan, X.; Luber, E.J.; Olsen, B.C.; Kalisvaart, W.P.; Jungjohan, K.L.; Mitlin, D.; Buriak, J.M. β-SnSb for Sodium Ion Battery Anodes: Phase Transformations Responsible for Enhanced Cycling Stability Revealed by In Situ TEM. *ACS Energy Lett.* **2018**, 3, 1670-1676

[29] Pan, Y.; Wu, X.-J.; Zhang, Z.-Q.; Fu, Z.-W.; Zhou, Y.-N. Binder and carbon-free SbSn-P nanocomposite thin films as anode materials for sodium-ion batteries. *J. Alloy Compd.* **2017**, *714*, 348-355.

[30] Lin, Y.-M.; Abel, P. R.; Gupta, A.; Goodenough, J. B.; Heller, A.; Mullins, C. B. Sn-Cu nanocomposite anode for rechargeable sodium-ion batteries. *ACS Appl. Mater. Interfaces* **2013**, *5*, 8273-8277.

[31] Liu, J.; Wang, S.; Kravchyk, K.; Ibáñez, M.; Krumeich, F.; Widmer, R.; Nasiou, D.; Meyns, M.; Llorca, J.;Arbiol, J.; Kovalenko, M. V.; Cabot, A. SnP Nanocrystals as Anode Materials for Na-Ion Batteries. *J. Mater. Chem. A* **2018**, 6, 10958– 10966.

[32] Yang, L.; Yang,B.;Chen, X.;Wang, H.; Dang, J.;Liu, X. Bimetallic Alloy SbSn Nanodots Filled in Electrospun N-doped Carbon Fibers for High Performance Na-ion Battery Anode. *Electrochim. Acta.***2021**, 389, 138246

[33] Li, X.;Xiao,S.;Niu,X;Chen,J.S.;Yan,Y. Efficient Stress Dissipation in Well-Aligned Pyramidal SbSn Alloy Nanoarrays for Robust Sodium Storage. *Adv. Func. Mat.* **2021**, *31*, 2104789

[34] Liu, J.; Wen, Y.; van Aken, P. A.; Maier, J.; Yu, Yan. Facile synthesis of highly porous Ni-Sn intermetallic microcages with excellent electrochemical performance for lithium and sodium storage. *Nano Lett.* **2014**, *4*, 6387-6392.

[35] Liu, J.; Yang, Z.; Wang, J.; Gu, L.; Maier, J.; Yu, Y. Three-dimensionally interconnected nickel-antimony intermetallic hollow nanosphere as anode material for high-rate sodium-ion batteries. *Nano Energy* **2015**, *16*, 389-398.

[36] Cook, J. B.; Lin, T. C.; Detsi, E.; Weker, J. N.; Tolbert, S. H. Using X-ray Microscopy To Understand How Nanoporous Materials Can Be Used To Reduce the Large Volume Change in Alloy Anodes. *Nano Lett.* 2017, *17*, 870-877.

[37] Cook, J. B.; Kim, H.-S.; Lin, T. C.; Robbennolt, S.; Detsi, E.; Dunn, B. S.; Tolbert, S. H. Tuning porosity and surface area in mesoporous silicon for application in Li-ion battery electrodes. *ACS Appl. Mater. Interfaces* **2017**, *9*, 19063-19073.

[38] Cook, J. B.; Detsi, E.; Liu. Y.; Liang, Y.-L.; Kim, H.-S.; Petrissans, X.; Dunn, B.; Tolbert, S. H. Nanoporous tin with a granular hierarchical ligament morphology as a highly stable li-ion battery anode. *ACS Appl. Mater. Interfaces* **2017**, *9*, 293-303.

[39] Detsi, E.; Petrissans, X.; Yan, Y.; Cook, J. B.; Deng, Z.; Liang, Y.-L.; Dunn, B.; Tolbert, S. H. Tuning ligament shape in dealloyed nanoporous tin and the impact of nanoscale morphology on its applications in Na-ion alloy battery anodes. *Phys. Rev. Materials* **2018**, *2*, 055404.

[40] Hayes, J. R.; Hodge, A. M.; Biener, J.; Hamza, A. V. Monolithic nanoporous copper by dealloying Mn-Cu. *J. Mater. Res.* **2006**, *21*, 2611-2616.

[41] Detsi, E.; Tolbert, S.H.; Punzhin, S.; De Hosson, J.Th.M. Metallic muscles and beyond: nanofoams at work. *J. Mat. Sci.* **2016**, *51*, 615–634.

[42] Thommas, M.; Kaneko, K.; Neimark, A. W.; Olivier, J. P.; Rodriguez-Reinoso, F.; Rouquerol, J.; Sing, K. S. W. Physisorption of gases, with special reference to the evaluation of surface area and pore size distribution (IUPAC Technical Report). *Pure Appl. Chem*. **2015**, *87*, 1051- 1069.

[43] Darwiche, A.; Sougrati, M. T.; Fraisse, B.; Stievano, L.; Monconduit, L. Facile synthesis and long cycle life of SnSb as negative electrode material for Na-ion batteries. *Electrochemistry Communications* **2013**, *32*, 18-21.

[44] Chen, C.; Fu, K.; Lu, Y.; Zhu, J.; Xue, L.; Hu, Y.; Zhang, X. Use of a tin antimony alloy-filled porous carbon nanofiber composite as an anode in sodium-ion batteries. *RSC Adv.* **2015**, *5*, 30793-30800.

[45] Xiao, L.; Cao, Y.: Xiao, J.; Wang, W.; Kovarik, L.; Nie, Z.; Liu, J. High capacity, reversible alloying reactions in SnSb/C nanocomposites for Na-ion battery applications. *Chem. Commun.* **2012**, *48*, 3321-3323.

[46] Ji, L.; Zhou, W.; Chabot, V.; Yu, A.; Xiao, X. Reduced graphene oxide/Tin-antimony nanocomposite as anode materials for advanced sodium-ion batteries. *ACS Appl. Mater. Interfaces* **2015**, *7*, 24895-24901.

[47] Zhou, X.; Liu, X.; Xu, Y.; Liu, Y.; Dai, Z.; Bao, J. An SbOx/ Reduced graphene oxide composite as a high-rate anode material for sodium-ion batteries. *J. Phys. Chem. C* **2014**, *118*, 23527-23534.

[48] Sun, Q.; Ren, Q.-Q.; Li, H.; Fu, Z.-W. High capacity Sb2O4 thin film electrodes for rechargeable sodium battery. *Electrochemistry Communications* **2011**, *13*, 1462-1464.

[49] Wang, Y.; Su, D.; Wang, C.; Wang, G. SnO2@MWCNT nanocomposite as a high capacity anode material for sodium-ion batteries. *Electrochemistry Communications* **2013**, *29*, 8-

11.

[50] Wu, L.; Hu, X.; Qian, J.; Pei, F.; Wu, F.; Mao, R.; Ai, X.; Yang, H.; Cao, Y. Sb-C Nanofibers with long cycle life as an anode material for high-performance sodium-ion batteries. *Energy Environ. Sci.* **2014**, *7*. 323-328.

[51] Darwiche, A.; Marino, C.; Sougrati, M. T.; Fraisse, B.; Stievano, L.; Monconduit, L. Better cycling performances of bulk Sn in Na-ion batteries compared to Li-ion systems: An unexpected electrochemical mechanism. *J. Am. Chem. Soc.* **2012**, *134*, 20805-20811.

[52] Kim, C.; Lee, K.-Y.; Kim, I.; Park, J.; Cho, G.; Kim, K.-W.; Ahn, J.-H.; Ahn, H.-J. Long-term cycling stability of porous Sn anode for sodium-ion batteries. *J. Power Sources* **2016**, *317*, 153-158.

53 Rodriguez, J.R.; Aguirre, S.B.; Pol, V.G. Role of operando microscopy techniques on the advancement of sustainable sodium-ion battery anodes. *J. of Pow. Sourc.* **2019**, 437, 226851.

54 Darwiche, A.; Marino, C.; Sougrati, M.T.; Friasse, B.; Stievano, L.; Monconduit, L. Better Cycling Performance of Bulk Sb In Na-Ion Batteries compared to Li-Ion Systems: An Unexpected Electrochemical Mechanism. *J. Am. Chem. Soc.* **2012**, *134*, 20805-20811

55 Im, H.S.; Cho, Y.J.; Lim, Y.R.; Jung, C.S.; Jang, D.M.; Park, H.; Shojaei, F;Kang, H.S. Phase Evolution of Tin Nanocrystals in Lithium Ion Batteries. *ACS Nano* **2013**, 7, 11103-11111.

56 Baggetto, L.; Hah, H.Y.; Jumas, J.C.; Johnson, C.E.; Johnson, J.A.; Keaum, J.K.; Bridges, C.A.; Veith, G.M. The reaction mechanism of SnSb and Sb thin film anodes for Na-ion batteries studied by X-ray diffraction, ^{119}Sn and ^{121}Sb Mossbauer spectroscopies. *J. of Pow. Sourc.* **2014**, 267, 329-336.

[57] Lin, T.C.; Dawson, A.A.; King, S.C.; Yan, Y.; Ashby, D.S.; Mazzetti, J,A,; Dunn, B.S.; Weker,.N.; Tolbert, S.H.; Understanding Stabilization in Nanoporous Intermetallic Alloy Anodes for Li-Ion Batteires Using *Operando* Transmission X-Ray Microscopy. *ACS Nano.* **2020**, 14, 14820-14830.

[58] Liu, Y.; Palmieri, A.; He, J.; Meng, Y.; Beauregard, N.; Suib, S. L., Mustain, W. E. Highly Conductive In-SnO2/RGO Nano-Heterostructures with Improved Lithium-Ion Battery Performance. *Scientific Reports* **2016**, *2*, 25860.

[59] Chae, S.; Ko, M.; Kim, K.; Ahn, K.; Cho, J. Confronting issues of the practical implementation of Si anode in high-energy lithium-ion batteries. *Joule* **2017**, *1*, 47-60.

Chapter 4: Improved Cycling Capabilities of Nanoporous Antimony Tin with Atomic-Layer-Deposition Aluminum Oxide for Sodium Ion Batteries

4.1 Introduction

Rechargeable batteries with high energy densities are critical for the development of renewable energies as the intermittent nature of solar and wind resources produce varying amounts of energy based on the vagaries of weather. In order to store this energy for the grid, economic battery chemistries are required. Sodium-ion batteries with alloying anodes have recently become a promising cheaper alternative to lithium-ion batteries due to the low market price of sodium and the high specific volumetric energy densities of alloying anodes (3-10 times higher than graphite).[1-6]

Though alloying anodes such as Sn and Sb are attractive, the unstable metal/electrolyte interface and the materials degradation resulting from the volume change during alloying reactions with Na^+ still hinder their use in practical devices.[1-8] While nanostructuring is an effective method for reducing the volume expansion and crack propagation of alloying anodes,[9,10] the increased surface area leads to increased amounts of electrolyte degradation.[11] Typically, a stable solid electrolyte interphase (SEI) forms on the surface of an active material during the first few cycles as the electrolyte decomposes to form a thin layer of inorganic and organic products.[12-16] Conventional carbonate-based electrolytes with sodium salts (e.g., $NaPF_6$, $NaClO_4$, etc.) readily decompose below ~1.5 V vs. Na/Na^+ to a series of carbonates, fluorides, chlorides, and oxides derivatives. A stable SEI that is electronically insulating and ionically conductive is beneficial because it prevents further electrolyte degradation by blocking the electron transport while allowing Na^+ to pass during cycling.[11] However, this can also introduce a high interfacial resistance

due to the ionically insulating nature of certain decomposition products and reduce the capacity of the device as the formation of SEI consumes the sodium ions in the electrolyte.[17,18] Particularly with alloying anodes, stable SEIs can be difficult to form due to repetitive volume changes and crack propagation that expose new surfaces for SEI formation.[17] Certain metals such as Sn, are also known to catalyze electrolyte decomposition.[7,8,19] In order to enable the use of these high-energy-density materials, controlling the stability and properties of electrochemical interfaces while limiting the volume expansion is crucial.

The use of oxides and nitrides as artificial SEIs have recently demonstrated promising results in improved cycling stability and reversibility.[20-25] These thin surface coatings not only prevent the formation of a SEI but also improve the structural integrity of the electrode by anchoring the active material to the current collector.[26-28] Among potential artificial SEI oxides, Al_2O_3 is particularly attractive due to its high ionic conductivity after sodiation (and the formation of a Na-Al-O glass) and its robust ceramic nature.[29-32] Atomic layer deposition (ALD) can be used to deposit a thin coating of materials. Surface coatings deposited through ALD is favorable because of the low deposition temperature, conformality, and tunable thickness.[20,21,33] More importantly, the layer-by-layer atomic scale depositions allow tailoring of the exact stoichiometric composition.

In this study, we demonstrate the improved electrochemical performance of nanoporous antimony tin (NP-SbSn) with an ALD Al_2O_3 coating for sodium ion batteries. Intermetallic SbSn is chosen because the two active components alloy with Na^+ at different potentials, allowing for a more gradual volume expansion. This reduces the stress accumulated in the materials and improves the mechanically stablility. Moreover, at any given voltage, there is an unreactive component stabilizing the overall structure.[34-36] NP-SbSn with an Al_2O_3 coating can be cycled reversibly with 312 mAh/g after 100 cycles. *Operando* transmission X-ray microscopy (TXM) was performed to

understand the stabilization mechanism of these coatings on nanoporous structures. In the first TXM study performed on alloying anodes with ALD coating, NP-SbSn with Al_2O_3 coating is shown to expand less during electrochemical cycling, allowing better retention of the porous structure over 10 cycles. These results provide a mechanistic understanding of surface coatings on nanostructured materials and indicate the viability of the approach in enabling alloying anodes for high energy density applications.

4.2 Results and Discussion

4.2.1 Materials and Characterization

NP-SbSn was synthesized using a facile selective etching synthesis. In brief, NP-SbSn was etched from a $Sb_{20}Sn_{80}$ at.% parent alloy, consisting of tetragonal Sn and rhombohedral β-SbSn, using HBr acid. As Sn (the less noble metal) dissolves into the etchant, the remaining intermetallic SbSn forms nanoclusters that rearrange into a bicontinuous porous structure. Details regarding this synthesis can be found in our previous studies on NP-SbSn's cycling performances as lithium- and sodium-ion anodes. The X-ray diffraction pattern of NP-SbSn is shown in Figure 4.1a. The XRD pattern matches well with the JCPD pattern (No. 00-001-0830) of β-SbSn with the *R-3m* space group.

The optimal ALD coating thickness is dependent on the pores size of NP-SbSn. According to the pore size distribution calculated from the Barrett-Joyner-Halenda (BJH) model, the mesopores in NP-SbSn are >20 nm as shown in the inset of Figure 4.1b. Figure 4.1b shows the Type-IV isotherm of NP-SbSn measured from N_2 porosimetry, indicating that the structure is

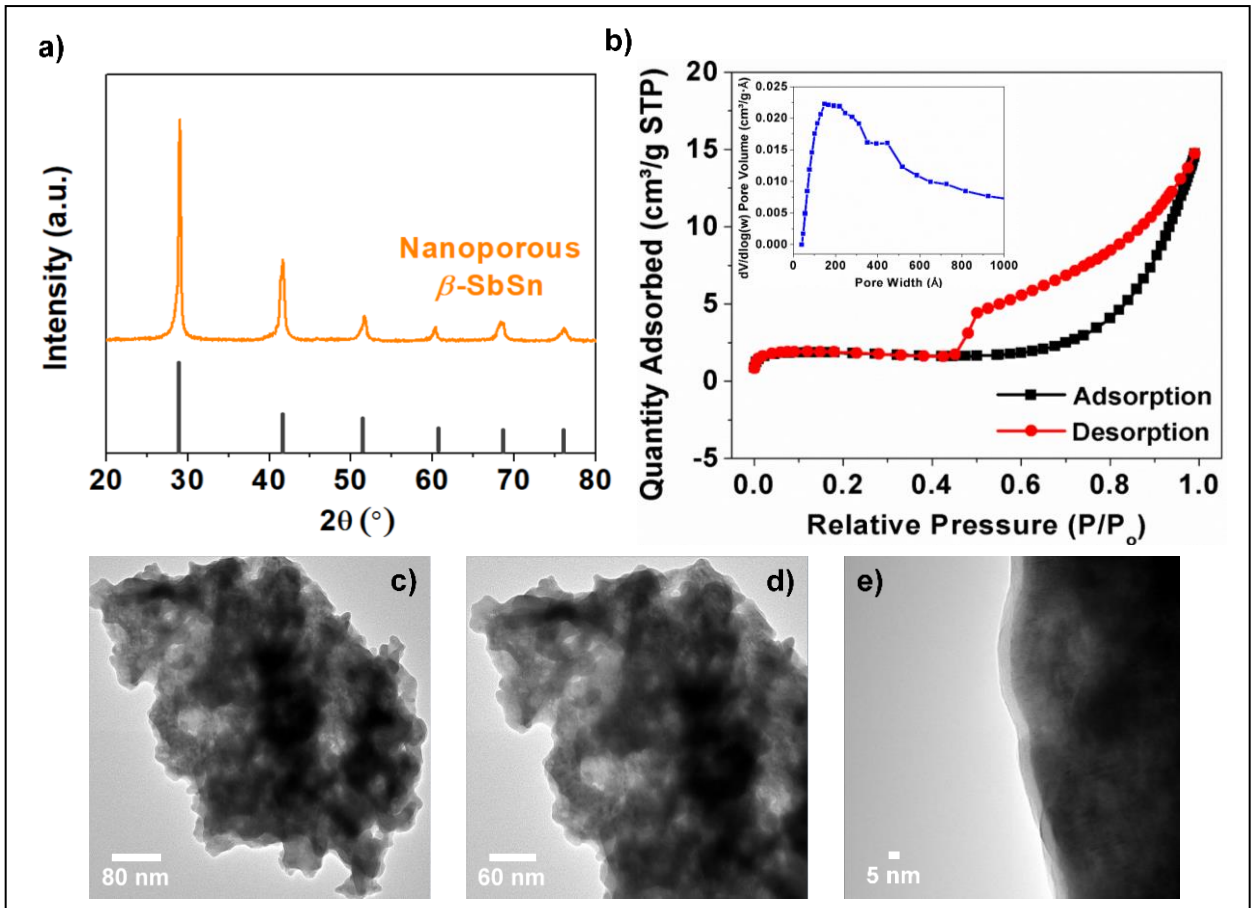

Figure 4.1. a) Powder X-ray diffraction pattern of NP-SbSn. **b)** Isotherm of N_2 porosimetry. The inset shows the pore size distribution calculated from BJH. **c-d)** TEM images of pristine and **e)** Al_2O_3-coated NP-SbSn powder.

bimodal with both macropores and mesopores. The total surface area is 5 m^2/g calculated from the Brunauer-Emmett-Teller (BET) model. A 5 nm thickness of Al_2O_3 was chosen for this study because it allows the >20 nm pores in NP-SbSn to remain open after deposition of the oxide and

previous studies have shown that open pores are crucial for suppressing volume expansion in these nanoporous metals during electrochemical cycling. The voids improve electrolyte penetration and promote a more uniform sodiation/desodiation process without the formation of core shell structures that lead to the propagation of cracks. Al_2O_3 was deposited onto NP-SbSn powder to demonstrate the conformality of the coatings through ALD. Figures 4.1c and 4.1d show the TEM images of the pristine powder and Figure 4.1e shows the Al_2O_3-coated NP-SbSn particle. The evenly coated 5 nm artificial SEI on nanoporous particle surface can be observed. While the deposition of Al_2O_3 onto the active material is suitable for imaging, the application of an artificial SEI prior to electrode fabrication can result in slower ion diffusion and the obstruction of electron transport pathways as the oxide layer prohibits direct particle to particle contact within the electrode.[37] Therefore, to study the cycling stability of Al_2O_3-coated NP-SbSn, the ALD coatings were deposited directly onto the composite electrode composed of active material, conductive additive, and binder.

4.2.2 Electrochemical Cycling

Figure 4.2a and 4.2b show the cyclic voltammograms (CV) of the bare and Al_2O_3-coated NP-SbSn, respectively. Na^+ first alloys with Sb to form amorphous Na_xSb and hexagonal Na_3Sb then alloys with Sn to $Na_{3.75}Sn$. The electrochemical processes are described in Equation 1-3. The voltammograms of the bare and Al_2O_3-coated electrodes reveal very similar redox features. On the first cycle, NP-SbSn undergoes an activation process in which the native surface oxides reduce to Sb and Sn metal (Equation 4).[38-40] The required overpotential for this reaction bypasses the antimony reduction potential (0.7 V vs. Na/Na^+), resulting in the presence of a big broad peak starting at 0.6V (alloying/dealloying SbSn to Na_3Sb and $Na_{3.75}Sn$). On the following cycle, redox

peaks of the reversible alloy and dealloy reactions can be observed at their expected potentials and redox pairs at 0.55/0.9 and 0.2V/0.7 V vs. Na/Na^+ represent the conversion of Sb to Na_3Sb and Sn to $Na_{3.75}Sn$, respectively.[41-43] An additional peak at 0.81 V vs. Na/Na^+ is observed in the anodic scan of the coated sample. The corresponding cathodic peak is present at 0.48 V vs. Na/Na^+. This peak corresponds to the intermediate phase, Na_xSb, of the Na and Sb alloying reaction.[41] With the improved ionic conductivity of the coated sample and absence of the SEI, sharper and more refined redox peaks are revealed from the CV curve due to the improved reversibility from the ionically conductive ALD layer.

$$SnSb + xNa^+ + xe^- \rightarrow Sn + Na_xSb \quad \text{(Equation 1)}$$

$$Sn + Na_xSb + (3-x)Na^+ + (3-x)e^- \rightarrow Sn + Na_3Sb \quad \text{(Equation 2)}$$

$$Na_3Sb + Sn + 3.75Na + 3.75e^- \rightarrow Na_3Sb + Na_{3.75}Sn \quad \text{(Equation 3)}$$

$(SbO_2, SnO_2)_{surface} + xNa + xe^- \rightarrow yNa_2O + (Sb, Sn)_{surface}$ (Equation 4)

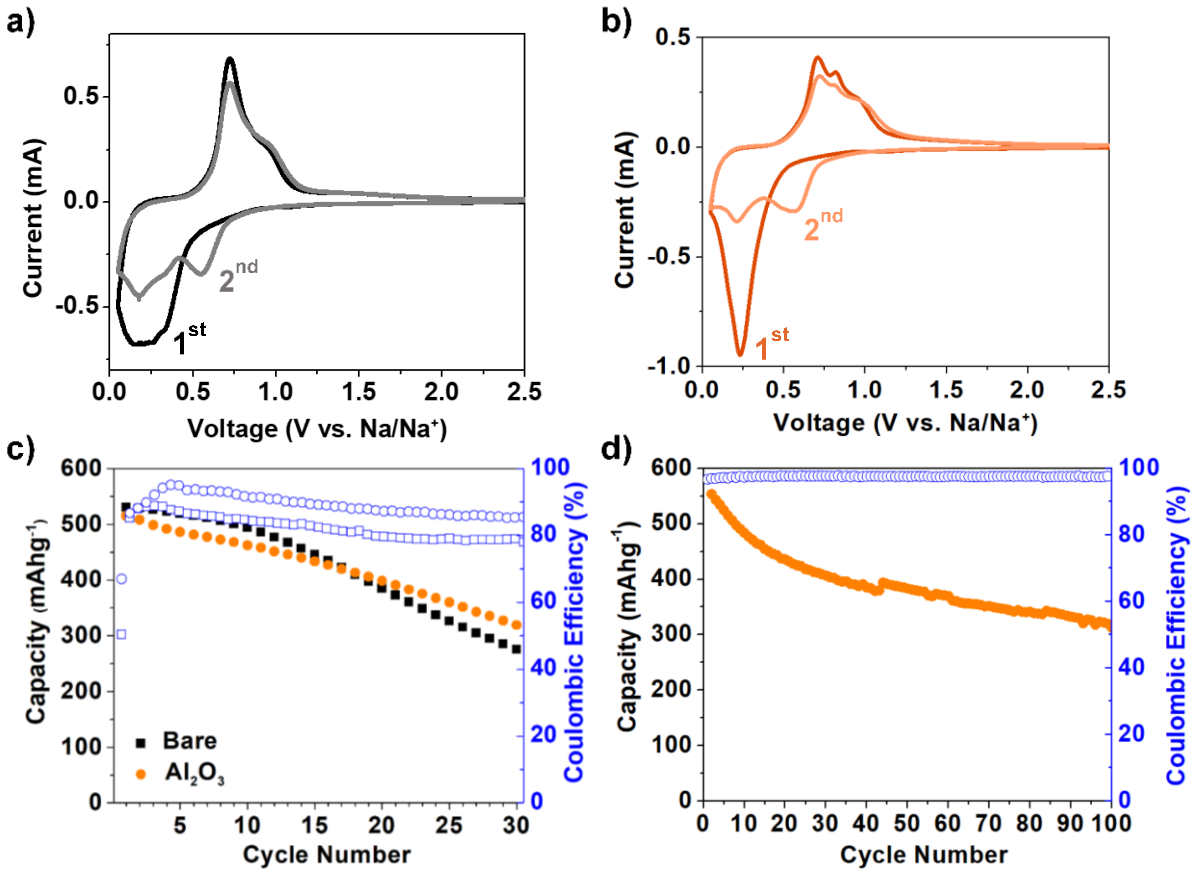

Figure 4.2. Cyclic Voltammogram of the **a)** bare electrode and the **b)** Al_2O_3-coated electrode. **c)** Stability test of the bare and Al_2O_3-coated SbSn in a three-electrode flooded cell. d**)** Long term cycling of the Al_2O_3-coated SbSn in a two-electrode cell.

Galvanostatic charge and discharge profiles of bare and Al_2O_3-coated NP-SbSn electrodes cycled at 0.1C (based on the theoretical capacity of SbSn 725 mAh/g) are shown in Figure 4.2c. This preliminary study was performed in a three-electrode flooded cell before the long-term study to demonstrate the improved cycling capability of the coated electrode in comparison to the bare. The lack of stack pressure in a flooded cell represents a worse-case scenario for the lifetime SbSn electrodes, allowing for the accelerated testing of the coating. The 530 mAh/g capacity of the bare

SbSn electrode is close to the theoretical specific capacity of 725 mAh/g. As described previously, alloying anodes undergo pulverization due to the volume expansion and continuous formation of SEI during electrochemical cycling. This results in a capacity of only 275 mAh/g after 30 cycles. Though the capacity of the coated sample was initially lower than the bare, it demonstrated better capacity retention with 318 mAh/g after 30 cycles. Better columbic efficiency is also found in the ALD NP-SbSn due to the lack of SEI formation on the electrode. The efficiency increased steadily in the first few cycles as the Al_2O_3 layer continues to sodiate with increased cycling, resulting in higher ionic conductivities. Long-term cycling of the Al_2O_3-coated samples in a two-electrode Swagelok cell is shown in Figure 4.2d. With Al_2O_3, NP-SbSn delivered 312 mAh/g after 100 cycles, which is higher than the specific capacity of hard carbon, which is another promising alternative anode for Na-ion batteries.

4.2.3 Operando Transmission X-ray Microscopy Study

To understand the role of surface coatings in stabilizing the nanoporous structure during electrochemical cycling, o*perando* TXM was performed at beamline 6-2C at Stanford Synchrotron Radiation Lightsource (SSRL). *Operando* TEM studies have been performed in attempt to understand the structural changes of alloying anodes with artificial SEIs,[26,44-46] but are not compatible with the study of composite electrodes used in actual devices due to the limited field of view and the extinction depth of electrons.[47] The use of high flux hard X-ray radiation in TXM offers a large field of view (15−30 μm) and a penetration depth of 100 nm -100 micron with a spatial resolution of 30 nm.[48,49] Because of this, TXM is well suited for studying battery electrodes at the nanoscale under actual operating conditions.[47,50]

Figure 4.3a and 4.3b show the absorption images of NP-SbSn with and without Al_2O_3 coating at OCV, 0.05V (sodiated), and 1.5V (desodiated) vs. Na/Na^+. The calculated volume change throughout cycling is presented in Figure 4.3c. It is apparent that the coated NP-SbSn expands less (49%) than the bare NP-SbSn (68%) during charging and the coated NP-SbSn contracts close to its original size (7%) while NP-SbSn does not (25%). This difference in volume change suggests that the coating is physically restraining the volume expansion of NP-SbSn during the sodiation process due to the high bulk modulus of Al_2O_3 compared to the intermetallic.[51,52] The better reversibility of the expansion and contraction of the nanoporous structure can also be attributed to the Na-Al-O layer that allows more uniform sodiation/desodiation of NP-SbSn compared to the SEI present on the bare NP-SbSn.

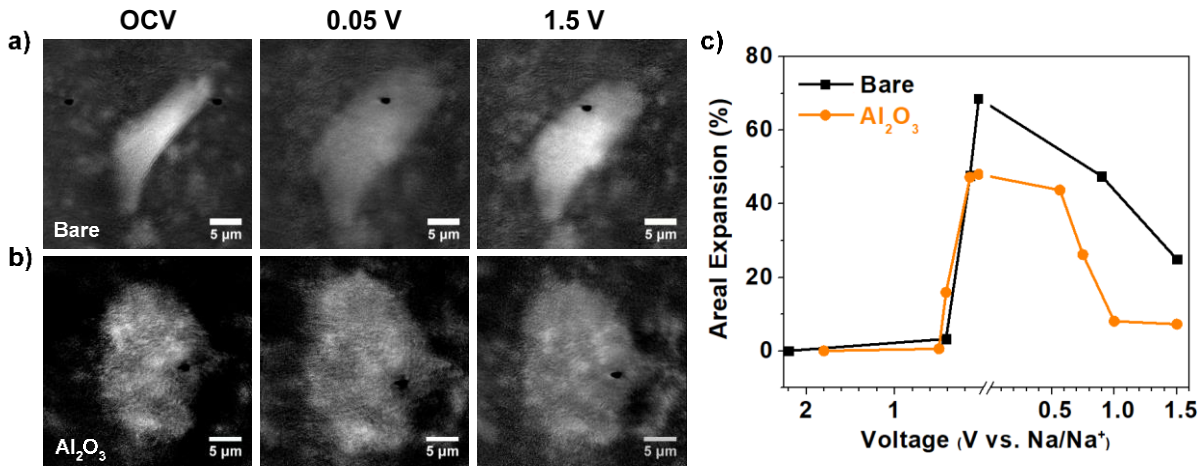

Figure 4.3. Absorption images of the **a)** bare and **b)** Al_2O_3-coated SbSn particle. **c)** Areal expansion of the two electrodes throughout cycling.

The pore evolution during electrochemical cycling was also analyzed using *operando* TXM. Figure 4.4a shows the pore evolution throughout charge and discharge while Figure 4.4b shows the absorption images of the pores at OCV, 0.05 V and 1.5 V vs. Na/Na^+. In addition to stabilizing the overall particle structure, the conformal Al_2O_3 coating is shown to also stabilize the inner porous structure, particularly the pore walls. High magnification absorption images used to calculate the pore size and their corresponding histograms at different voltages can be found in

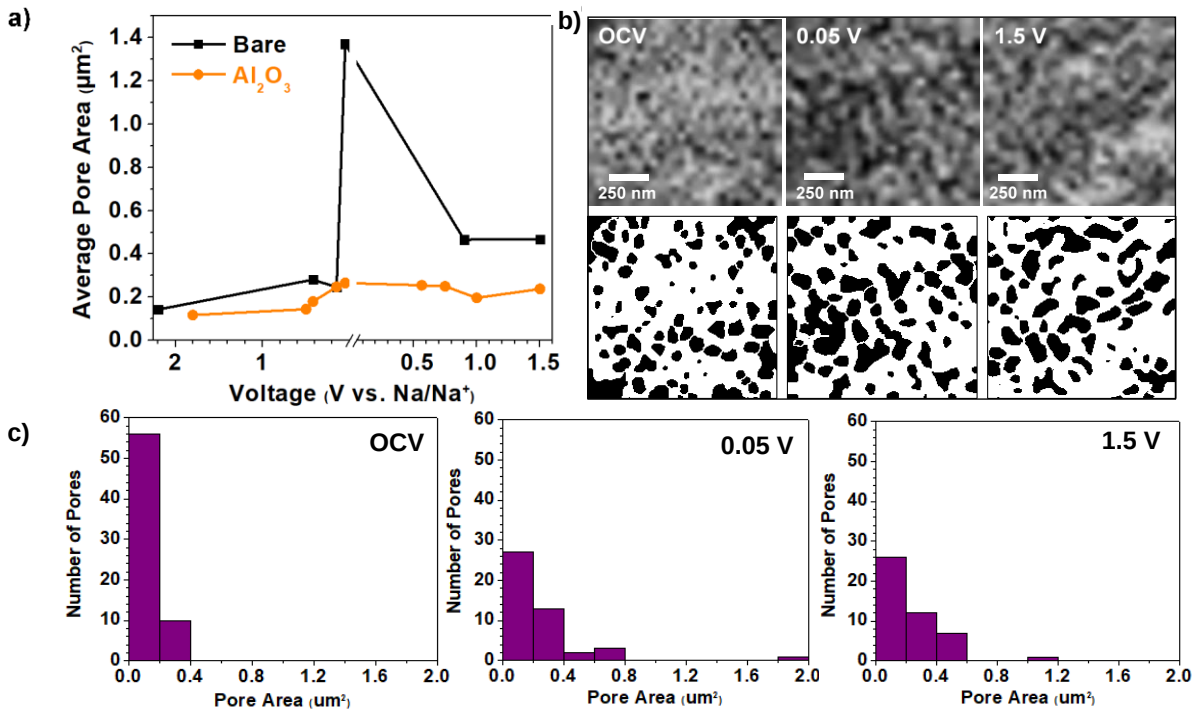

Figure 4.4. a) Pore evolution of bare and coated SbSn throughout cycling **b)** Absorption images of pores of the Al_2O_3-coated NP-SbSn powder at OCV, 0.05 V (sodiated), and 1.5 V (desodiated) vs. Na/Na^+. The images converted to black and white are below with black indicating porous regions. **c)** Pore area distributions of each state of charge calculated using the black and white images in b.

Figure 4.4b, 4.4c. A much smaller increase in the pore area due to pore wall degradation is observed in the coated NP-SbSn compared to the bare SbSn. Under ideal conditions, a decrease in pore area should occur as the particle expands isotropically during sodiation. This small degree of pore wall degradation in the coated sample can potentially result from the expansion of the Al_2O_3

coating during the initial sodiation process. It has been shown that sodiation occurs at the Al_2O_3 layer first before the active material. This causes the Al_2O_3 coating to expand as it sodiates to Na-Al-O.[26,45]

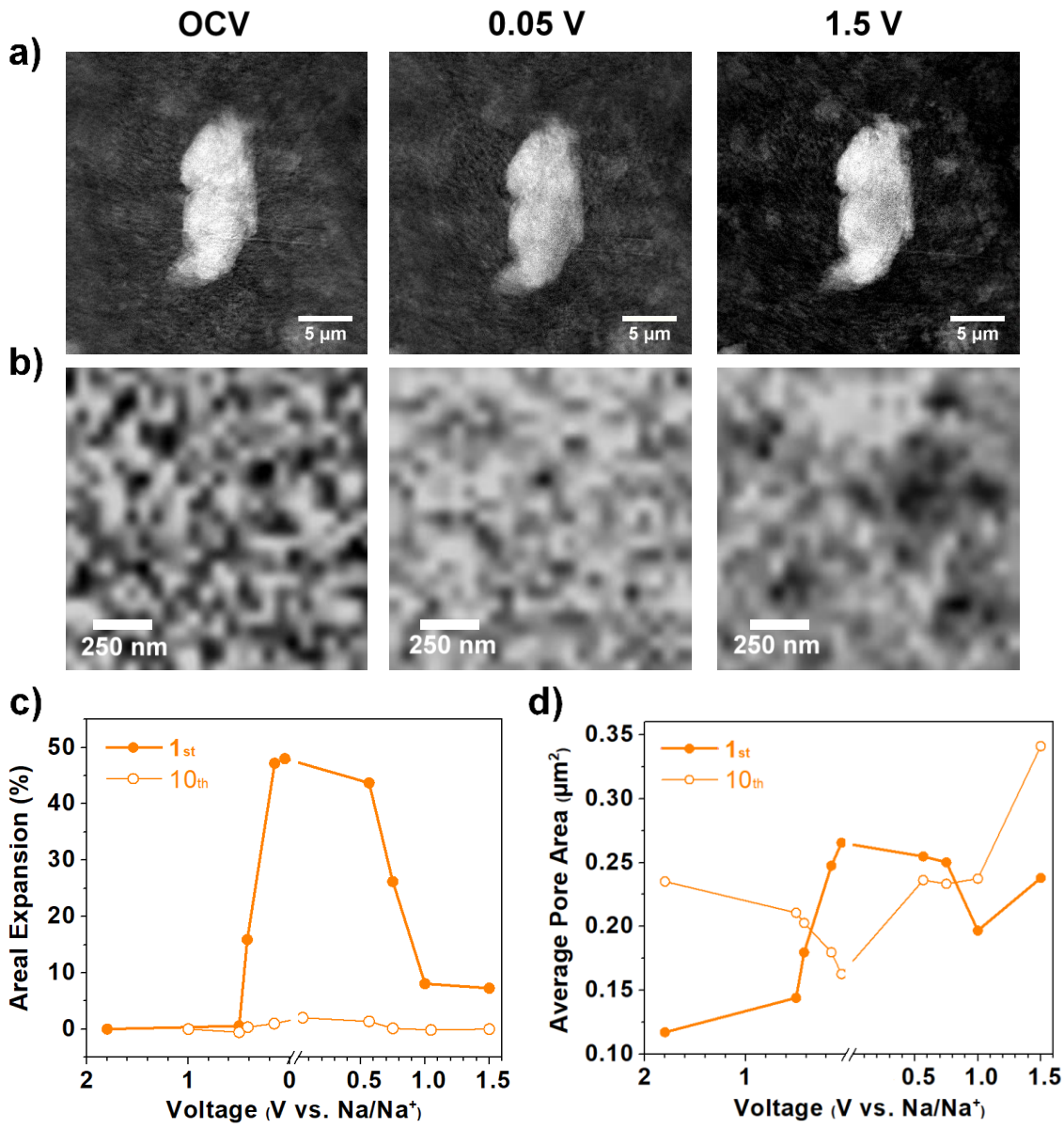

Figure 5. a) Absorption images of the coated NP-SbSn on the 10th cycle. **b)** High magnification of the absorption images of the pores. The black regions resulting from image thresholding correspond to domains of the NP-SbSn. **c)** Areal expansion of the Al_2O_3-coated NP-SbSn powder on first and 10th cycle **d)** Pore area evolution of the Al_2O_3-coated NP-SbSn powder on the first and 10th cycle.

To study the change in stabilization mechanism over repeated cycling, *operando* TXM was performed on the 10th charge-discharge cycle. The charge capacity of cycle 1-9 in addition to the galvanostatic charge and discharge profile of the *operando* cell on the 10th cycle can be found in. During the 10th cycle, negligible volume change is observed throughout cycling. Furthermore, a

different evolution in the porosity is observed in the coated NP-SbSn. Interestingly, Na-Al-O has a lower bulk modulus (more elastic) than Al_2O_3.[30] After the initial surface sodiation process, the coating provides a flexible protective layer with good ionic conductivity. This can therefore result in different behaviors in the stabilization mechanism in the first and subsequent cycles. Instead of an increase in pore area during charge, the pore area decreased as expected for an isotropic expansion. This suggests that after the initial pore degradation in the first cycle, the Na-Al-O coating allows the material to expand in all directions. With the particle expanding into the voids of the porous structure, the overall volume expansion decreases significantly. The presence of this elastic artificial SEI is critical in preserving the conduction pathways in the electrode and prolonging the lifetime of alloying anodes. A stretchable SEI layer with high ionic conductivity that can expand and contract with the material without breaking is beneficial as it creates a robust kinetic barrier for electron transfer. This prevents the formation of the traditional SEI with low ionic conductivity. Even though pore wall degradation was observed in the first cycle of our ALD NP-SbSn when the particle and the Al_2O_3 layer expand, a stable pore evolution and minimal volume expansion were observed in later cycles. This suggests that the small amount of traditional SEI introduced during the first cycle is stable with the ALD coating.

4.3 Conclusions

In this study we have demonstrated that artificial SEIs are effective in reducing the volume expansion, improving the structural integrity of the porous structure and maintaining good electrical and ionic conductivity of NP-SbSn electrode. This improves the reversibility of the alloying reactions and the longevity of NP-SbSn. These NP-SbSn can be cycled stably over 100 cycles with a capacity of 312 mAh/g. *Operando* TXM shows that the nanoporous structure was

stabilized in later cycles as the Al_2O_3 becomes more flexible to accommodate the volume change. This highly ionically conductive layer prevents the formation a SEI layer and constrains the volume expansion of these alloying anodes. Though this work focuses on the changes in pristine and Al_2O_3-coated NP-SbSn during sodiation/desodiation, this result should be insightful and for many other nanostructured materials with different coatings.

4.4 References

[1] Park, C.- M.; Kim, J.-H.; Kim, H.; Sohn, H.-J. Li-alloy Based Anode Materials for Li Secondary Batteries. *Chem. Soc. Rev.* **2010**, *39*, 3115-3141.

[2] Zhang, W.-J. Lithium Insertion/ Extraction mechanism in Alloy Anodes for Lithium-ion Batteries. *J. Power Source* **2011**, *196*, 877-885.

[3] Nitta, N.; Yushin, G.; Higher Capacity Anode Materials for Lithium-Ion Batteries: Choice of Elements and Structures for Active particles. *Part. Part. Syst. Charact.* **2014**, *31*, 317-336.

[4] Kim, Y.; Ha, K.-H.; Oh, S. M.; Lee, K. T. High-Capacity Anode Materials for Sodium-Ion Batteries. *Chem. Eur. J.* **2014**, *20*, 11980-11992.

[5] Luo, W.; Shen, F.; Bommier, C.; Zhu, H.; Ji, X.; Hu, L. Na-Ion Battery Anodes: Materials and Electrochemistry. *Acc. Chem. Res.* **2016**, *49*, 231-240.

[6] Hwang, J.-Y.; Myung, S.-T.; Sun, Y.-K. Sodium-Ion Batteries: Present and Future. *Chem. Soc. Rev.* **2017**, ***46***, 3529-3614.

[7] Beaulieu, L. Y.; Beattie, S. D.; Hatchard, T. D.; Dahn, J. R. The Electrochemical Reaction of Lithium with Tin Studied By In Situ AFM. *J. Electrochem. Soc.* **2003**, *150*, A419-A424.

[8] Wagner, M. R.; Raimann, P. R.; Trifonova, A.; Moeller, K.-C.; Besenhard, J. O.; Winter, M. Electrolyte Decomposition Reactions of Tin and Graphite-Based Anodes are Different. *Electrochem. Solid-State Lett.* **2004**, *7*, A201-A205.

[9] Wu, H.; Cui, Y. Designing Nanostructured Si Anodes for High Energy Lithium-ion Batteries. *Nano Today* **2012**, *7*, 414-429.

[10] Zhang, H.; Hasa, I.; Passerini, S. Beyond Insertion for Na-Ion Batteries: Nanostructured Alloying and Conversion Anode Materials. *Adv. Energy Mater.* **2018**, *8*, 1702582.

[11] Park, M.; Zhang, X.; Chung, M.; Less, G. B.; Sastry, A. M. A Review of Conduction Phenomena in Li-ion Batteries. *J. Power Sources* **2010**, *195*, 7904-7929.

[12] Wang, A.; Kadam, S.; Li, H.; Shi, S.; Qi, Y. Review on Modeling of the Anode Solid Electrolyte Interphase (SEI) for Lithium-ion Batteries. *npj Computational Materials* **2018**, *4*, 15.

[13] Slater, M. D.; Kim, D.; Lee, E.; Johnson, C. S. Sodium-Ion Batteries. *Adv. Funct. Mater.* **2013**, *23*, 947-958.

[14] Lucas, I. T.; Pollak, E.; Kostecki, R. In situ AFM Studies of SEI Formation at a Sn Electrode. *Electrochemistry Communication* **2009**, *11*, 2157-2160.

[15] Verma, P.; Maire, P.; Novák, P. A Review of the Feature and Analyses of the Solid Electrolyte Interphase in Li-Ion Batteries. *Electrochimica Acta* **2010**, *55*, 6332-6341.

[16] An. S. J.; Li, J.; Daniel, C.; Mohanty, D.; Nagpure, S.; Wood, D. L. The State of Understanding of the Lithium-ion Battery Graphite Solid Electrolyte Interphase (SEI) and its Relationship to Formation Cycling. *Carbon* **2016**, *105*, 52-76.

[17] Jin, Y.; Zhu, B.; Lu, Z.; Liu, N.; Zhu, J. Challenges and Recent Progress in the Development of Battery. *Adv. Energy Mater.* **2017**, *7*, 1700715.

[18] Zhang, S. S. A Review on Electrolyte Additives for Lithium-ion Batteries. *J. Power Sources* **2006**, *162*, 1379-1394.

[19] Beattie, S. D.; Hatchard, T.; Bonakdarpour, K. C. H.; Dahn, J. R. Anomalous, High-Voltage Irreversible Capacity in Tin Electrode for Lithium Batteries. *Journal of The Electrochemical Society* **2003**, *150*, A701-A705.

[20] Meng, X. Atomic-scale Surface Modifications and Novel Electrode Designs for High -Performance Sodium-Ion Batteries via Atomic Layer Deposition. *J. Mater. Chem. A* **2017**, *5*, 10127-10149.

[21] Meng, X.; Yang, X.-Q.; Sun, X. Emerging Applications of Atomic Layer Deposition for Lithium-Ion Battery Studies. *Adv. Mater.* **2012**, *24*, 3589-3615.

[22] He, Y.; Yu, X.; Wang, Y.; Li, H.; Huang, X. Alumina-Coated Patterned Amorphous Silicon as the Anode for a Lithium-Ion Battery with High Coulombic Efficiency. *Adv. Mater.* **2011**, *23*, 4938-4941.

[23] Loftabad, E. M.; Kalisvaart, P.; Cui, K.; Kohandehghan, A.; Kupsta, M.; Olsen, B.; Mitlin, D. ALD TiO2 Coated Silicon Nanowires for Lithium-ion Battery Anode with Enhanced Cycling Stability and Coulombic Efficiency. *Phys. Chem. Chem. Phys.* **2013**, *15*, 13646 -13657.

[24] Kohandehghan, A.; Kalisvaart, P.; Cui, K.; Kupsta, M.; Memarzadeh, E.; Mitlin, D. Silicon Nanowire Lithium-ion Battery Anodes with ALD Deposited TiN Coatings Demonstrate a major Improvement in Cycling Performance. *J. Mater. Chem. A* **2013**, *1*, 12850-12861.

[25] Perng, Y.-C.; Cho, J.; Sun, S. Y.; Membreno, D.; Cirigliano, N.; Dunn, B.; Chang, J. P. Synthesis of Ion Conducting $Li_xAl_ySi_zO$ Thin Films by Atomic Layer Deposition. *J. Mater. Chem. A* **2014**, *2*, 9566-9573.

[26] Han, X.; Liu, Y.; Jia, Z.; Chen, Y.-C.; Wan, J.; Weadock, N.; Gaskell, K. J.; Li, T.; Hu, L. Atomic-Layer-Deposition Oxide Nanoglue for Sodium Ion Batteries. *Nano Lett.* **2014**, *14*, 139-147.

[27] Wang, D.; Yang, J.; Liu, J.; Li, X.; Li, R.; Cai, M.; Sham, T.-K.; Sun, X. Atomic Layer Deposited Coatings to Significantly Stabilize Anodes for Li Ion Batteries: Effects of Coating Thickness and the Size of Anode Particles. *J. Mater. Chem. A* **2014**, *2*, 2306-2312.

Kang, E. K.; Jung, Y. S.; Cavanagh, A. S.; Kim, G.-H.; George, S. M.; Dillon, A. C.; Kim, J. K.; Lee, J. Fe3O4 Nanoparticles Confined in Mesocellular Carbon Foam for High

Performance Anode Materials for Lithium-Ion Batteries. *Adv. Funct. Mater.* **2011**, *21*, 2430-2438.

[29] Loftabad, E. M.; Kalisvaart, P.; Kohandehghan, A.; Cui, K.; Kupsta, M.; Farbod, B.; Mitlin, D. Si Nanotubes ALD Coated with TiO_2, TiN or Al_2O_3 as High Performance Lithium Ion Battery Anode. *J. Mater. Chem. A* **2014**, *2*, 2504-2516.

[30] Jung, S. C.; Kim, H.-J.; Choi, J. W.; Han, Y.-K. Sodium Ion Diffusion in Al_2O_3: A Distinct Perspective Compared with Lithium Ion Diffusion. *Nano Lett.* **2014**, *14*, 6559-6563.

[31] Susman, S.; Ratner, M. A. Transport in Glassy Fast-Ion Conductors: A Study of $LiAlSiO_4$ Glass. *Journal of Non-Crystalline Solids* **1988**, *101*, 54-64.

[32] Luo, W.; Lin, C.-F.; Zhao, O.; Noked, M.; Zhang, Y.; Rubloff, G. W.; Hu, L. Ultrathin Surface Coating Enables the Stable Sodium Metal Anode. *Adv. Energy Mater.* **2017**, *7*, 1601526.

[33] Marichy, C.; Bechelany, M.; Pinna, N. Atomic Layer Deposition of Nanostructured Materials for Energy and Environmental Applications. *Adv. Mater.* **2012**, *24*, 1017-1032.

[34] Pan, Y.; Wu, X.-J.; Zhang, Z.-Q.; Fu, Z.-W.; Zhou, Y.-N. Binder and carbon-free SbSn-P nanocomposite thin films as anode materials for sodium-ion batteries. *J. Alloy Compd.* **2017**, *714*, 348-355.

[35] Lin, Y.-M.; Abel, P. R.; Gupta, A.; Goodenough, J. B.; Heller, A.; Mullins, C. B. Sn-Cu nanocomposite anode for rechargeable sodium-ion batteries. *ACS Appl. Mater. Interfaces* **2013**, *5*, 8273-8277.

[36] Liu, J.; Wang, S.; Kravchyk, K.; Ibáñez, M.; Krumeich, F.; Widmer, R.; Nasiou, D.; Meyns, M.; Llorca, J.;Arbiol, J.; Kovalenko, M. V.; Cabot, A. SnP Nanocrystals as Anode Materials for Na-Ion Batteries. *J. Mater. Chem. A* **2018**, *6*, 10958– 10966.

[37] Jung, Y. S.; Cavanagh, A. S.; Riley, L. A.; Kang, S.-H.; Dillon, A. C.; Groner, M. D.; George, S. M.; Lee, S.-H. Ultrathin Direct Atomic Layer Deposition on Composite Electrodes for Highly Durable and Safe Li-Ion Batteries. *Adv. Mater.* **2010**, *22*, 2172-2176.

[38] Zhou, X.; Liu, X.; Xu, Y.; Liu, Y.; Dai, Z.; Bao, J. An SbO_x/ Reduced graphene oxide composite as a high-rate anode material for sodium-ion batteries. *J. Phys. Chem. C* **2014**, *118*, 23527 -23534.

[39] Sun, Q.; Ren, Q.-Q.; Li, H.; Fu, Z.-W. High capacity Sb_2O_4 thin film electrodes for rechargeable sodium battery. *Electrochemistry Communications* **2011**, *13*, 1462-1464.

[40] Wang, Y.; Su, D.; Wang, C.; Wang, G. SnO_2@MWCNT nanocomposite as a high capacity anode material for sodium-ion batteries. *Electrochemistry Communications* **2013**,*29*,8-11.

[41] Wu, L.; Hu, X.; Qian, J.; Pei, F.; Wu, F.; Mao, R.; Ai, X.; Yang, H.; Cao, Y. Sb-C Nanofibers with long cycle life as an anode material for high-performance sodium-ion batteries. *Energy Environ. Sci.* **2014**, *7*, 323-328.

[42] Darwiche, A.; Marino, C.; Sougrati, M. T.; Fraisse, B.; Stievano, L.; Monconduit, L. Better cycling performances of bulk Sn in Na-ion batteries compared to Li-ion systems: An unexpected electrochemical mechanism. *J. Am. Chem. Soc.* **2012**, *134*, 20805-20811.

[43] Kim, C.; Lee, K.-Y.; Kim, I.; Park, J.; Cho, G.; Kim, K.-W.; Ahn, J.-H.; Ahn, H.-J. Long-term cycling stability of porous Sn anode for sodium-ion batteries. *J. Power Sources* **2016**, *317*, 153-158.

[44] Liu, Y.; Hudak, N. S.; Huber, D. L.; Limmer, S. J.; Sullivan, J. P.; Huang, J. Y. In Situ Transmission Electron microscopy Observation of Pulverization of Aluminum Nanowires and Evolution of the Thin Surface Al_2O_3 Layers During Lithiation-Delithiation Cycles. *Nano Lett.* **2011**, *11*, 4188-4194.

[45] Luo, L.; Yang, H.; Yan, P.; Travis, J. J.; Lee, Y.; Liu, N.; Piper, D. M.; Lee, S.-H.; Zhao, P.; George, S. M.; Zhang, J.-G.; Cui, Y.; Zhang, S.; Ban, C.; Wang, C.-M. Surface-Coating Regulated Lithiation Kinetics and Degradation in Silicon Nanowires for Lithium Ion battery. **2015**, *9*, 5559-5566.

[46] He, Y.; Piper, D. M.; Gu, M.; Travis, J. J.; George, S. M.; Lee, S.-H.; Genc, A.; Pullan, L.; Liu, J.; Mao, S. X.; Zhang, J.-G.; Ban, C.; Wang, C. In Situ Transmission Electron Microscopy Probing of Native oxide and Artificial Layers on Silicon nanoparticles for Lithium Ion Batteries. *ACS Nano* **2014**, *8*, 11816-11823.

[47] Cook, J. B.; Lin, T. C.; Detsi, E.; Weker, J. N.; Tolbert, S. H. Using X-ray Microscopy To Understand How Nanoporous Materials can be Used to Reduce the Large Volume Change in Alloy Anodes. *Nano Lett.* **2017**, *17*, 870-877.

[48] Andrews, J. C.; Weckhuysen, B. M. Hard X-ray Spectroscopic Nano-Imaging of Hierarchical Functional Materials at Work. *ChemPhysChem*. **2013**, *14*, 3655-3666.

[49] Nelson, J.; Misra, S.; Yang, Y.; Jackson, A.; Liu, Y.; Wang, H.; Dai, H.; Andrews, J. C.; Cui, Y.; Toney, M. F. In Operando X-ray Diffraction and Transmission X-ray Microscopy of Lithium Sulfur Batteries. *J. Am. Chem. Soc.* **2012**, *134*, 6337-6343.

[50] Weker, J. N.; Huang, X.; Toney, M. F. In situ X-ray Based Imaging of Nano Materials. *Current Opinion in Chemical Engineering* **2016**, *12*, 14-21.

[51] Ylivaara, O. M. E.; Liu, X.; Kilpi, L.; Lyytinen, J.; Schneider, D.; Laitinen, M.; Julin, J.; Ali, S.; Sintonen, S.; Berdova, M.; Haimi, E.; Sajavaara, T.; Ronkainen, H.; Lipsanen, H.; Koskinen, J.; Hannula, S.-P.; Puurunen, R. L. Aluminum Oxide from Trimethylaluminum and Water by Atomic Layer Deposition: The Temperature Dependence of Residual Stress, Elastic Modulus, Hardness and Adhesion. *Thin Solid Films* **2014**, *552*, 124-135.

[52] Shalaby, R. M. Influence of Indium Addition on Structure, Mechanical, Thermal and Electrical Properties of Tin-Antimony Based Metallic Alloys Quenched from Melt. *Journal of Alloys and Compounds* **2009**, *480*, 334-339.

Chapter 5: Understanding Stability in Nanoporous Antimony as Lithium and Sodium Ion Battery Anodes Using *Operando* Diffraction and Microscopy

5.1 Introduction

Lithium ion batteries have revolutionized energy storage devices. To further this growth to electric vehicles and grid-scale storage, increased energy densities is vital. Alloy anodes are materials that alloy with the alkali metal leading to very high capacities, charge per gram or cubic centimeter of material. Compared to graphite (372 mAh/g or 756 mAh/cm^3), alloy anodes such as Si (4200 mAh/g or 2190 mAh/cm^3), Sn (993 mAh/g or 1991 mAh/cm^3), Bi (384 mAh/g or 3800 mAh/cm^3), Ge (1600 mAh/g or 2180 mAh/cm^3), and Sb (660 mAh/g or 1889 mAh/cm^3) can offer more than double the capacity, which has a linear relationship to energy density.[1–4] However, because these materials alloy with so much lithium, they expand and contract, >200% expansion, leading to detrimental cracking of the electrode and material. This fracturing happens within the first few cycles resulting in extreme capacity fade. As a result, stabilizing alloy anodes for repeated cycling has been of interest for decades.

One very powerful tool to stabilize these materials is to nanostructure them. At the nanoscale, grains are more ductile so that repeated expansion and contraction will not fracture the material. The surface to volume ratios of nanoparticles are high so the stress of lithiation dissipates easier across the particle. Secondly, the small volume particles prevent formation of a core shell structure during lithiation and delithiation which can lead to fracture.[5–7] The nanoparticles, in particular, have garnered a lot of interest, and there are many nanoparticle alloy anodes that perform very well.[8–15] One issue is the repeated outward expansion. Even though nanoparticles do not fracture, expansion and contraction can disrupt the slurry made of carbon and polymer binder leading to active material that is no longer electronically connected to the

rest of the slurry. To prevent this, increasing the carbon content or synthesizing, or embedding, the material onto the carbon is most common.[8,10,12–14]. Other nanoarchitecture designs have been proposed to utilize nanoscale features.

To prevent disruption of the slurry, architectures with void space have proven to be valuable. In this way, the void space is space for expansion to occur into. Hollow structures like hollow nanoparticles and wires have been successfully used to stabilize cycling.[16–19] However, these structures, even though can perform better than dense nanoparticles still have issues with electronic connectivity. Similar to nanoparticles, these hollow particles are often embedded in the carbon additive to maintain conductivity. [18] Hard surface coatings that limit the volume expansion of the particle have also been successful. These coatings prevent the alloy anode material from disrupting the slurry because they are electronically connected to the slurry and confine the material.[11,20] These coatings undergo a lot of stress confining the anode material and can prevent full lithiation. Alternatively, yolk-shell structures are an impressive nanostructure that can mitigate issues related to a surface coating.[21–23] The yolk is the active anode material that is inside a shell that is connected to the slurry. This is different than a surface coating because there is void space between the yolk and the shell. In this way, expansion can freely occur if the shell is maintained, and the core stays connected to the shell. Even though this strategy is very effective, one limitation is the economic viability of creating such structures. A structure that expands internally would not disrupt the slurry and inexpensive to synthesize would be ideal for alloy anodes.

Selective dealloying is a relatively inexpensive way to create mesoporous networks.[24] The particles can be microns big, but the porosity and pore walls are tens of nanometers. These networks preserve the nanoscale nature of the grains, and the pores can act as space for the small

grains to expand into. This process involves an alloy of a sacrificial metal and a more noble metal. When exposed to acid or base, the sacrificial component etches out, and the more noble component re-arranges on the surface creating a mesoporous network. A schematic of this is shown in Figure 5.1a. This method has been used to create alloy anode architectures extensively.[3,25–29] Our group has observed stabilization in Sn and SbSn.[28,30] In the case of lithiation of mesoporous SbSn, we have observed that the pore walls are more structurally sound than in mesoporous Sn. Secondly, in trying to understand the mechanism of lithiation we observed amorphization of the material. We hypothesize that this amorphization is key to stabilizing structure because it allows for easier re-arrangement of atoms and does not involve rigid domain walls between crystallites. Interestingly, amorphization has been seen in other alloy anode systems like Si and Ge.[1,2,31] Here we aim to study the role of nanoscale architecture and amorphization in alloy anodes.

Sb, in particular, has very interesting behavior when cycled with lithium vs sodium. Sodium ion batteries are an attractive alternative to lithium ion batteries because sodium is more abundant and cheaper than lithium. However, because of its size, the volume expansion and contraction due to incorporation of the alkali is often more severe for sodium than lithium. Consequently, many alloy anode systems that work with lithium are worse with sodium. Sb is an exception, where Sb with sodium performs as well if not better than lithium. Literature suggests that this is the case because Sb cycles through crystalline intermediates when against lithium and amorphous intermediates when against sodium. Commonly referenced mechanisms are seen below in equations 1 and 2:

$$Sb + 3Li^+ + 3e^- \rightarrow Li_2Sb_{crystalline} + 1Li^+ + 1e^- \rightarrow Li_3Sb_{crystalline} \quad \text{(Equation 1)}$$

$$Sb + 3Na^+ + 3e^- \rightarrow Na_xSb_{amorphous} + (3-x)\,Na^+ + (3-x)e^- \rightarrow Na_3Sb_{crystalline} \quad \text{(Equation 2)}$$

Here, we synthesize mesoporous Sb using selective dealloying and study how mechanism on the atomic scale affects macroscale features. To accomplish this, we use *operando* transmission X-ray microscopy (TXM) at BL 6-2c at the Stanford Synchrotron Radiation Lightsource (SSRL). This is a powerful technique that allows imaging of large fields of view, ~30 μm, with high resolution, ~30 nm. We observe porosity changes as well as full particle changes. Secondly, this technique can be used on pouch cells, in a real-world environment. However, the electrodes have lower mass loadings, ~25%, compared to normal electrodes.[28,30,32] With this technique, we aim to learn how nanostructure and amorphous intermediates play a role in stabilizing alloy anodes for repeated cycling.

In this work, we synthesized nanoporous Sb (NP-Sb) via selective dealloying as an alloy anode for both lithium and sodium ion batteries. We obtain good capacity retention. We, then, use *operando* X-ray diffraction to observe the atomic-scale, crystalline changes of the NP-Sb. We correlate these results with results from *operando* TXM on both the bulk and porous material to identify how these atomic-scale changes affect the mesoscale structure and the overall macroscale particle. These results can help conclude how nanoscale architecture and mechanism synergistically work together to preserve capacity in alloy anodes.

5.2 Results

5.2.1 Synthesis and Electrochemistry

We synthesized NP-Sb using selective dealloying. We started with a Sn and Sb alloy (8:2 Sn:Sb at. ratio). The alloy was etched in heated conc. HBr for 20 minutes. A schematic for selective dealloying is in Figure 5.1a. Figure 5.1b is the corresponding isotherm from N_2

porosimetry with a surface area of 7.964 m^2/g. SEM images in Figure 5.1c and 5.1d confirm porosity along with the TEM image in Figure 5.1e.

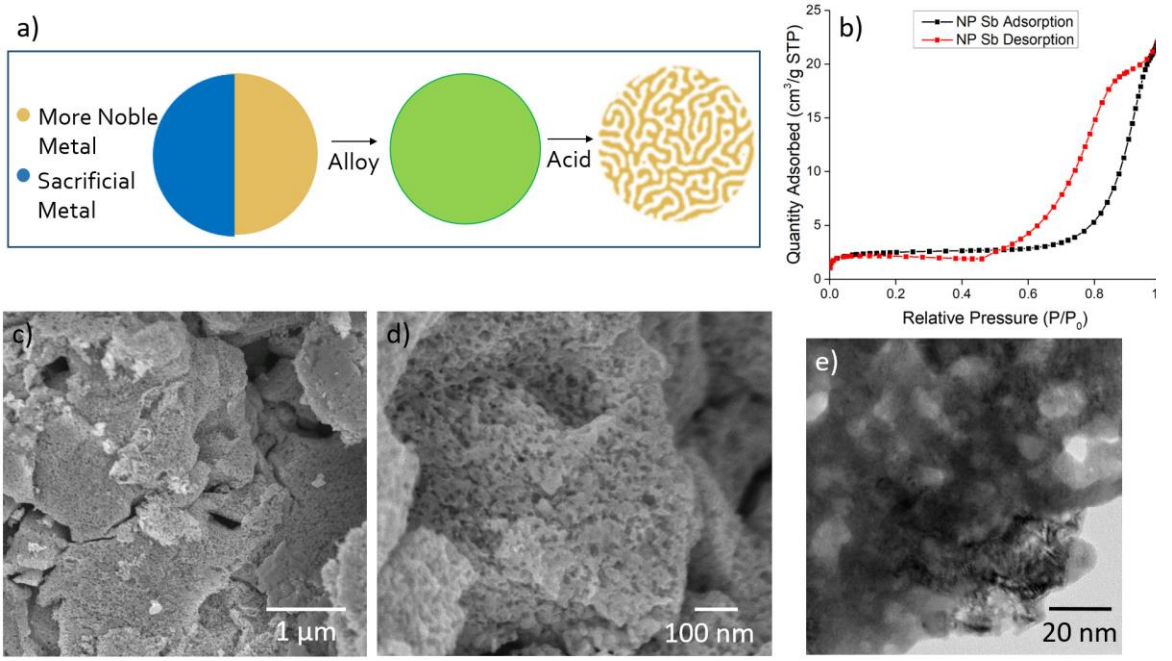

Figure 5.1.a. Cartoon explaining selective dealloying, where a sacrificial component of an alloy is etched out using acid **b.** Nitrogen porosimetry isotherm with adsportion and desorption curves shown. **c.** SEM image of mesoporous antimony synthesized using dealloying with scale bar of 1 micron **d.** SEM image of mesoporous antimony synthesized using dealloying with scale bar of 100 nanometers **e.** TEM image of mesoporous antimony synthesized using dealloying, where the nonuniform contrast

This resulting material was cycled in coin cells with a slurry of active material (66% wt), carbon fiber (16% wt), and carboxymethyl cellulose (18% wt). The cyclic voltammograms cycled at 0.1mV/s from 0.05 to 1.5 V are seen in Figure 5.2a and 5.2b for the NP-Sb vs lithium and sodium, respectively. For lithium, there is a reduction peak at 0.85 V consistent with the lithiation potential of Sb with its corresponding oxidation at 1.1 V. Against sodium, there is a reduction peak at 0.5 V consistent with sodiation of Sb and its corresponding oxidation at 0.8 V. The peaks are a broader for the sodium case suggesting that the sodiation mechanism is less

crystalline than the lithiation mechanism which suggests more complex intermediate behavior. Figure 5.2c shows long term cycling of the NP-Sb with lithium and sodium. We see that after an initial drop in capacity both curves stabilize and cycle well with a capacity retention of 440 mAh/g for lithium and 350 mAh/g for sodium after 50 cycles.

5.2.2 Operando X-Ray Diffraction

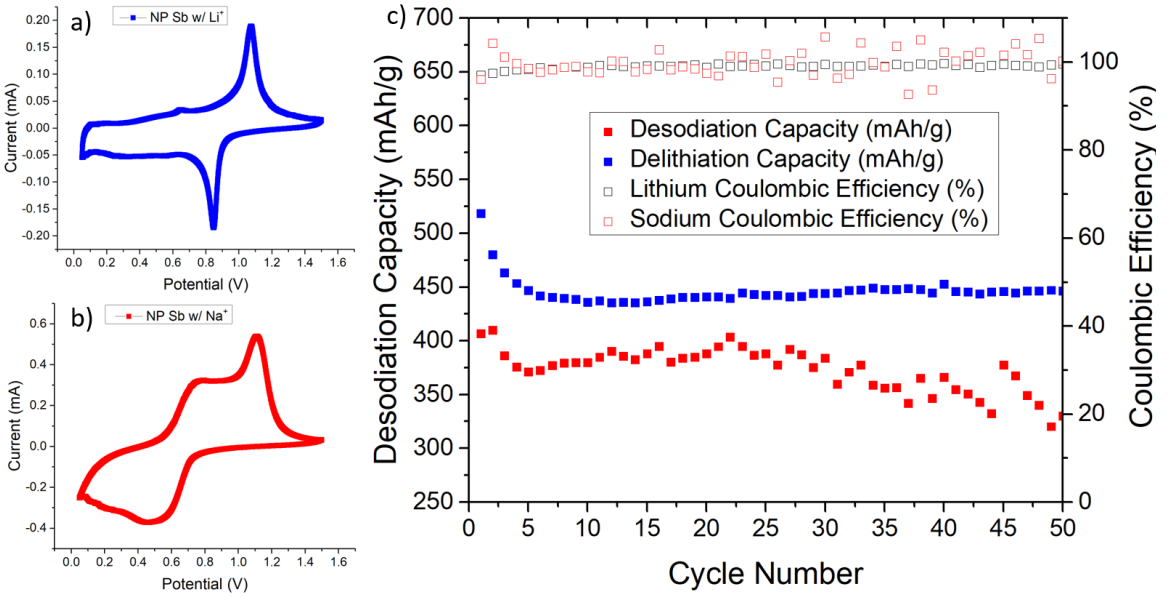

Figure 5.2. Electrochemical data for NP Sb cycled with both sodium and lithium. a) CV for NP Sb cycled with lithium. b) CV for NP Sb cycled with sodium. c) Graph showing capacity retention for NP Sb when cycled with lithium and sodium, and the corresponding coulombic efficiency values.

It is commonly understood that bulk Sb has crystalline intermediates with lithiation and amorphous intermediates with sodiation. However, it has been shown that nanostructured materials can incorporate the alkali differently than bulk. To verify the mechanism, we performed *operando* X-ray diffraction at SSRL BL 11-3. Figure 5.3 shows the galvanostat along with the diffraction patterns associated with the states of charge. In the beginning, crystalline antimony is present at around 2.02 $Å^{-1}$. Although, the peak is broad suggesting that it is nanoscale and poorly crystalline, this is common for dealloyed materials. As lithiation occurs,

the peak corresponding to Sb decreases while peaks grow at around 1.55 $Å^{-1}$ corresponding to Li_2Sb. Similarly, as lithiation continues, peaks of Li_2Sb disappear while peaks for Li_3Sb appear at around 1.67 and 1.92 $Å^{-1}$. One observation of note is that the peaks do not fully disappear before the next peaks appear resulting in two phase co-existence. Upon delithiation, crystalline Sb grows larger than when fully lithiated. However, it is much broader than the start suggesting that it is even less crystalline than when it started. There is also remnant Li_3Sb which implies that not all of the material is fully delithiated.

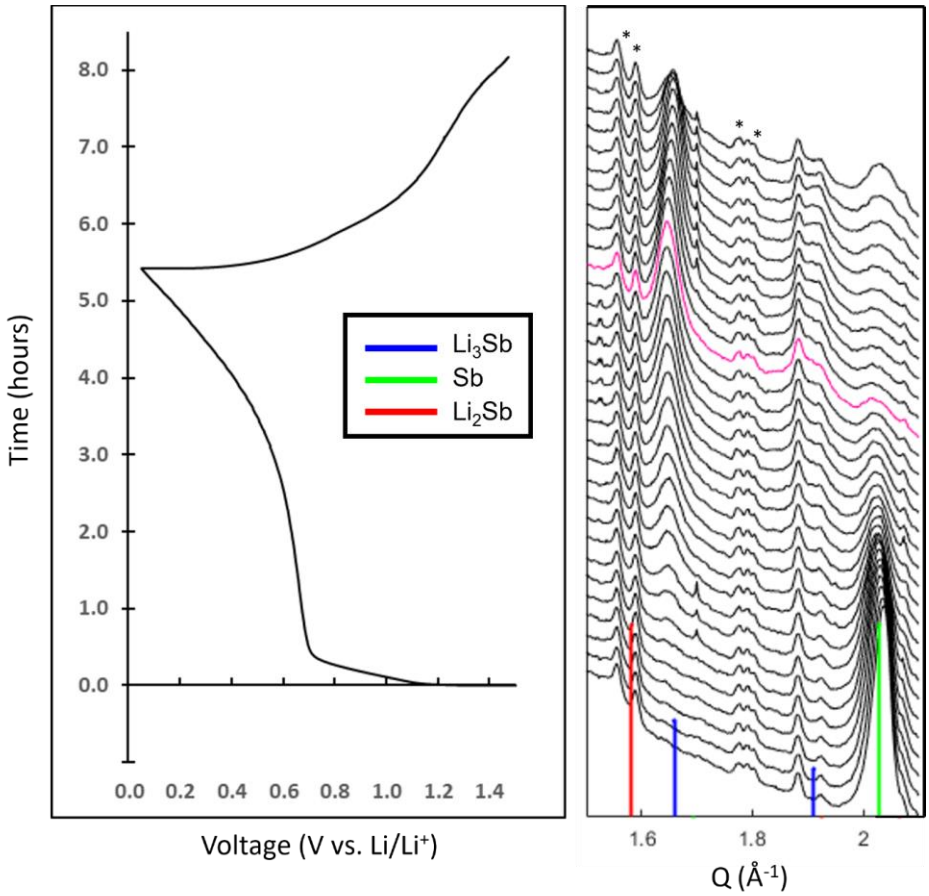

Figure 5.3. Galvanostat on the left with the corresponding diffraction pattern at that state of charge on the right. The key shows various crystal structures that are possibly present. Peaks that are starred are indicative of peaks associated with the pouch cell that are always present

Figure 5.4 is the galvanostat with corresponding diffraction patterns for the sodiation and desodiation of NP-Sb. As with the lithium case, crystalline Sb peaks at around 2.02 $Å^{-1}$ are at the beginning. These peaks fade with sodiation, and no peaks associated with the active material occur for several scans. Na_3Sb peaks emerge at around 1.32, 1.35, 1.55, 2.38, and 2.01 $Å^{-1}$ with continued sodiation. Unlike with lithium, no new crystalline phases form while another crystalline phase fades with sodium. This corroborates literature suggesting that Sb forms amorphous intermediates during sodiation. Upon desodiation, there are no discernible diffraction peaks. Crystalline Sb does not return, unlike with lithium. Another difference between the two mechanisms seen from diffraction is that we observe that lithiation of NP-Sb goes through a crystalline intermediates and that crystalline phases grow from another crystalline phase. Under sodiation, NP-Sb loses crystallinity before forming crystalline Na_3Sb. There are no crystalline intermediates when sodiated.

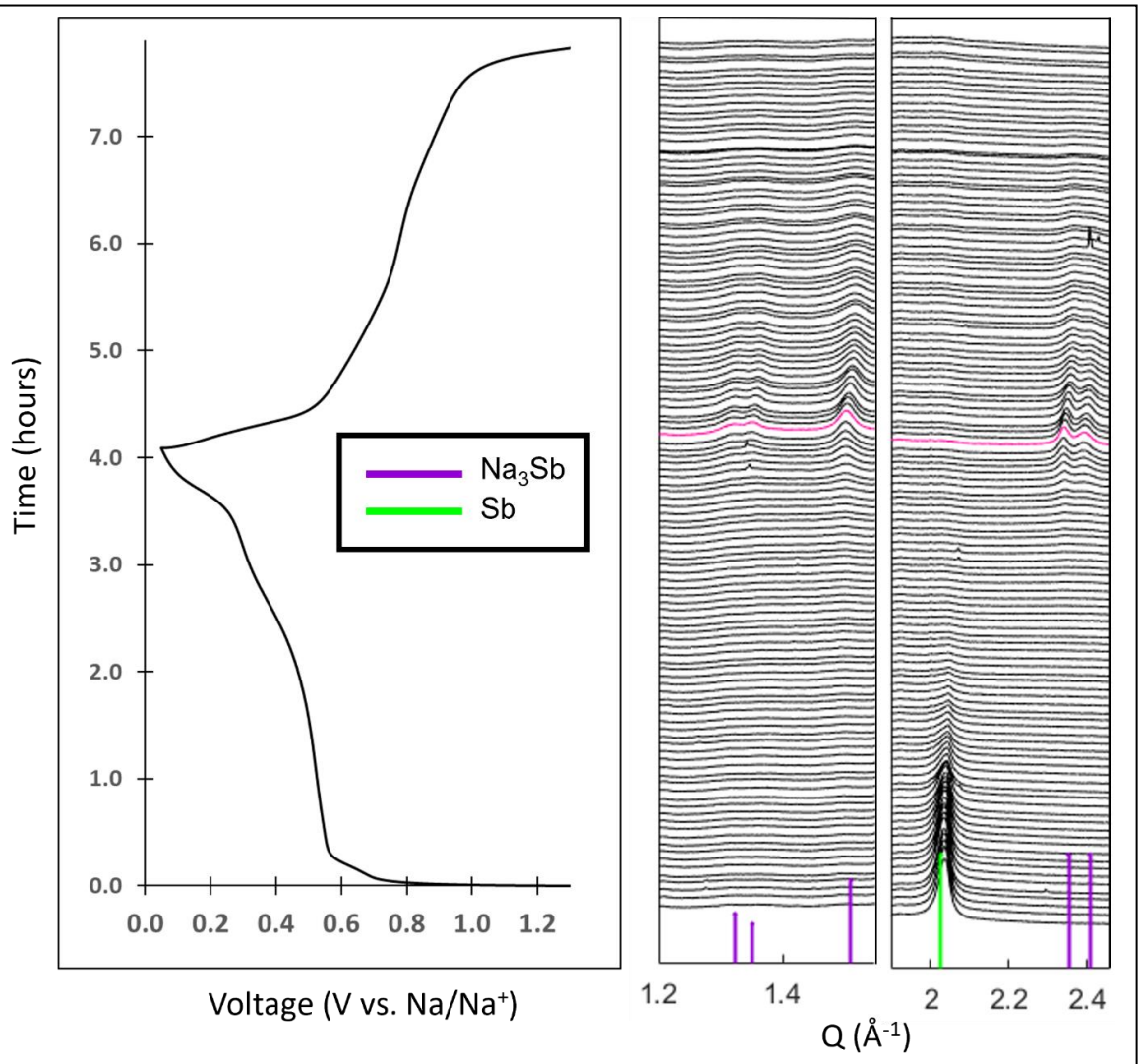

Figure 5.4. Galvanostat on the left with the corresponding diffraction pattern at that state of charge on the right. The key shows various crystal structures expected.

5.2.3 Macroscale Operando TXM

TXM from beamline 6-2c at SSRL is a powerful tool in understanding how particles change when cycled. Figure 5.5 shows images of bulk particles at different states of charge under sodiation and lithiation. It is important to understand how the bulk behaves in comparison to the nanoporous system to examine how nanostructure affects cycling. Figure 5.5a-c is bulk Sb under lithiation. We observe areal expansion of 65% and fracturing of the particle in the first cycle.

Figure 5.5d has a graph of the areal expansion throughout cycling for both lithiation and sodiation. In both graphs, there is burst of expansion during certain states of charge which is consistent with the alloying reactions at specific voltages. For sodiation, the bulk particle

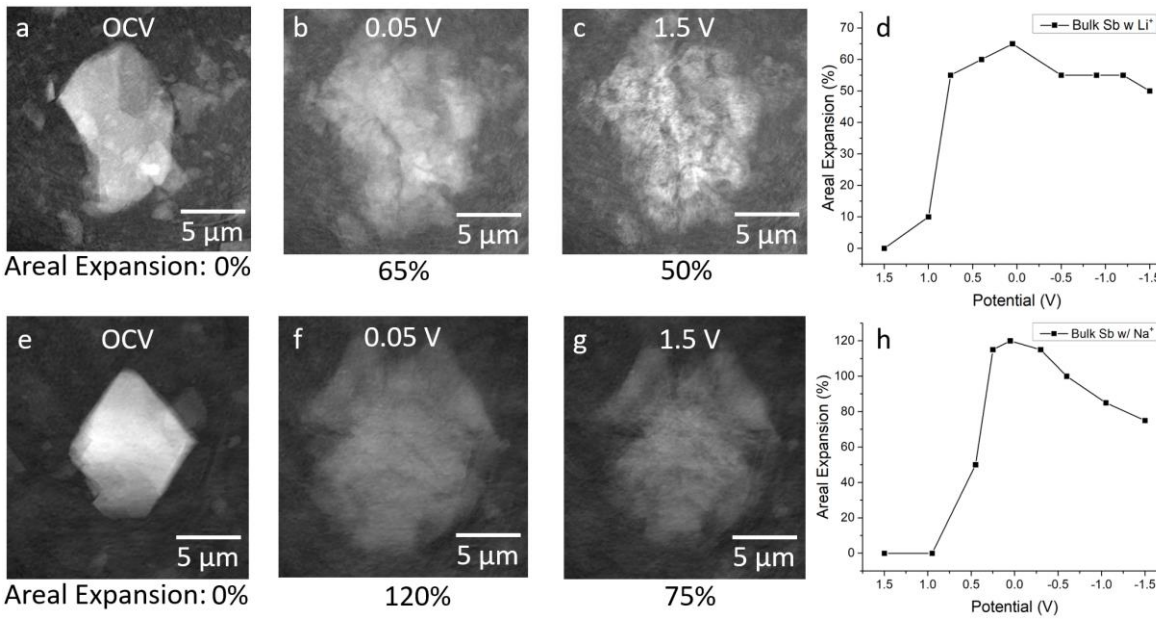

Figure 5.5. a. Bulk Sb particle at OCV **b.** Bulk Sb particle at 0.05 V (vs Li/Li^+), or fully lithiated **c.** Bulk Sb particle fully delithiated at 1.5 V (vs Li/Li^+) **d.** Graph of areal expansion versus state of charge where the peak of the expansion is full lithiation **e.** Bulk Sb particle at OCV **f.** Bulk Sb particle when fully sodiated at 0.05 V (vs. Na/Na^+) **g.** Bulk Sb particle when fully desodiated at 1.2 V (vs Na/Na^+) **h.** Graph of the areal expansion versus the state of charge where the peak is full sodiation.

expands more than lithium (120%), seen in Figure 5.5e-g. This is expected because sodium is larger than lithium so incorporating a larger ion would result in increased volume expansion. Interestingly, fewer fractures are observed with sodiation than with lithiation suggesting that the particles accommodate sodium better than lithium even though the volume expansion is greater with sodium.

NP-Sb behaves differently than bulk Sb. Figure 5.6 is images of NP-Sb under different states of charge for lithium and sodium. Figure 5.6d graphs the areal expansion of the NP-Sb against the voltage for lithiation. The overall shape of the graph is similar to Figure 5.5d which is expected because the alloying and dealloying reaction is at the same voltage for NP-Sb and bulk Sb. In both cases, the spike in volume expansion occurs around 1.0 V (vs. Li/Li^+) for lithiation and 0.8 V (vs. Na/Na^+) for sodiation. Even though the shape is the same, the nanoporous sample had much less volume expansion than the bulk counterpart: 50% and 100% for lithiation and sodiation, respectively. This shows that nanostructure can mitigate outward volume expansion.

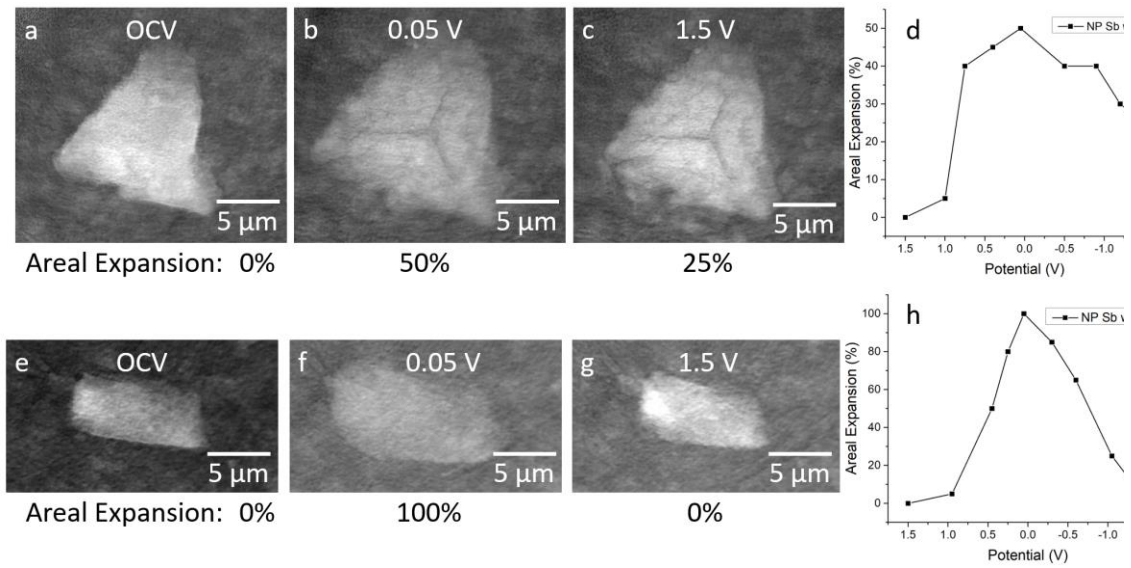

Figure 5.6. a. NP Sb particle at OCV **b.** NP Sb particle at 0.05 V (vs Li/Li^+), or fully lithiated **c.** NP Sb particle fully delithiated at 1.5 V (vs Li/Li^+) **d.** Graph of areal expansion versus state of charge where the peak of the expansion is full lithiation **e.** NP Sb particle at OCV **f.** NP Sb particle when fully sodiated at 0.05 V (vs. Na/Na^+) **g.** NP Sb particle when fully desodiated at 1.2 V (vs Na/Na^+) **h.** Graph of the areal expansion versus the state of charge where the peak is full sodiation.

The void space created by dealloying allows for inward volume expansion, resulting in less outward expansion. This would result in less disruption of the slurry. A second observation is

that during delithiation and desodiation, the nanoporous system shrinks in size whereas the bulk has minimal shrinking. This corroborates that our particles have nanocrystalline domains that expand and shrink similar to nanoparticles. In the case of sodium, the particle almost returns exactly to its original size even though it expands more than lithium. This suggests that the structural changes under sodiation allow for increased reversibility and structural rearrangement.

Figure 5.6a-c and 5.6e-g are the images of NP-Sb particles at different states of charge against lithium and sodium, respectively. Against sodium in Figure 5.6e-g, the particle expands and returns to a similar size and shape to when it started. This is highly unique even compared against other porous systems. When incorporating lithium in Figure 5.6a-c, there is some contraction, but the particle does not return to its original size or shape. In addition, fracturing and cracking appear in particles that are lithiated. This suggests that the pore walls are under more stress in lithiation than sodiation, even though sodium is larger than lithium. Interestingly, when matched to the diffraction, the fractures begin to appear around the same time as the crystalline Li_2Sb appears. We believe the stresses by having two phase co-existence and domain

walls between crystalline regions force the particle to fracture. This is not the case for sodiation because NP-Sb has non-crystalline intermediates allowing for structural adjustment.

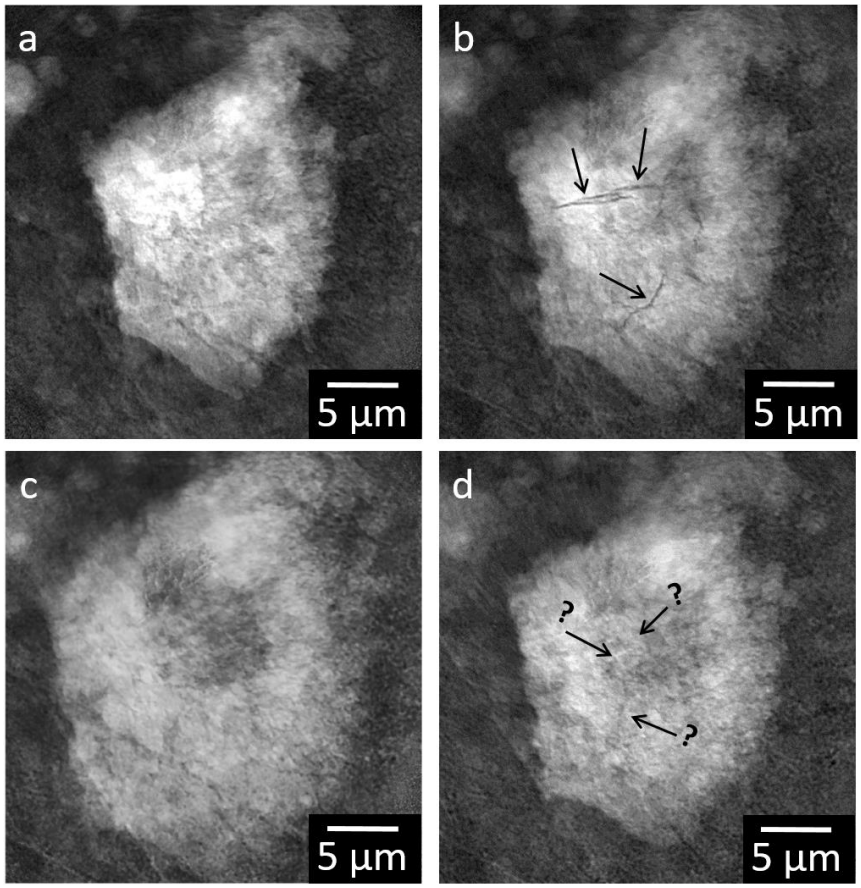

Figure 5.7. a. NP Sb particle at OCV **b.** NP Sb particle partially sodiated, showing interior cracking **c.** NP Sb particle fully sodiated at 0.05 V (vs Na/Na^+) **d.** NP Sb particle fully desodiated at 1.5 V (vs Na/Na^+)

For some bigger particles, we observe intriguing behavior. Figure 5.7 is images of a larger NP-Sb particle at different states of charge when sodiated. Similar to Figure 5.6 and 5.5 the particle expands. However, at a certain state of charge the particle cracks in the middle, seen in Figure 5.7b. It is odd that the particle begins fracturing in the middle because most fractures and stress start at the outer surface of the particle. After continued sodiation, the cracks disappear, seemingly healing in Figure 5.7c. When correlated to the diffraction results show previously, the cracks begin to appear when crystallinity starts decreasing around the 22nd scan

from the bottom. The stresses forming from domains walls between crystalline and non-crystalline domains fracture the particle. However, during the region where no crystalline Sb or sodiated Sb appear is where the apparent healing occurs which suggests that amorphization can lead to self-healing behavior. We hypothesize the amorphization allows for increased structural rearrangement. We only observe this behavior in NP-Sb and not bulk Sb. Thus, it is a combination of nanostructure and amorphous intermediates that cause this effect which is more than any one of them alone. When combined, the effect is not additive, but synergistic.

5.3 Conclusion

In this study, we synthesize mesoporous antimony through selective dealloying of antimony tin with hydrobromic acid. Interestingly, when cycled against sodium and lithium, the porous antimony performs better with sodium. Through X-ray diffraction at SSRL, we observe crystalline intermediates when cycled against lithium. In fact, as one phase shrinks, another one grows, suggesting two phase co-existence. With sodium, there are non-crystalline intermediate phases between the starting and ending crystalline phases. To understand how these crystallinity changes affect structure, we used TXM. With bulk samples, fracturing occurs. However, there is more fracturing with lithium even though the volume expansion is smaller. For porous samples, the particles do not expand as much as the bulk because the void volume can help accommodate particle expansion. In terms of fracturing, lithiation still cracks the particles. When mapped onto the diffraction, we notice the cracking starts to occur when the first lithiated phase appears, suggesting that shifting from one crystalline phase to another induces stresses to crack the particle. Sodium is much different. For one, when cycled, the particles expand and return to their original size. This is unusual, even for porous systems. Secondly, cracks that appear seemingly heal with further cycling. This healing occurs when no crystalline phases appear in diffraction.

We hypothesize that the non-crystalline phases allow for structural rearrangement so that fractures are healed. This is only observed in the nanostructured antimony. Thus, when amorphous intermediates and nanostructure are combined in one system, the effect is synergistic. We obtain new behavior that is not additive to each one individually: the system is highly reversible and self-healing. This is important in designing materials for anodes in rechargeable batteries because it provides design rules and phenomenon to achieve long lasting and high capacity materials. By using these design principles, we help propel rechargeable batteries to industries not yet capable of using these devices.

5.4 References

(1) Wang, J. W.; He, Y.; Fan, F.; Liu, X. H.; Xia, S.; Liu, Y.; Harris, C. T.; Li, H.; Huang, J. Y.; Mao, S. X.; Zhu, T. Two-Phase Electrochemical Lithiation in Amorphous Silicon. *Nano Letters* **2013**, *13* (2), 709–715. https://doi.org/10.1021/nl304379k.

(2) Liu, X.; Wu, X. Y.; Chang, B.; Wang, K. X. Recent Progress on Germanium-Based Anodes for Lithium Ion Batteries: Efficient Lithiation Strategies and Mechanisms. *Energy Storage Materials*. Elsevier B.V. September 1, 2020, pp 146–169. https://doi.org/10.1016/j.ensm.2020.05.010.

(3) Cook, J. B.; Detsi, E.; Liu, Y.; Liang, Y. L.; Kim, H. S.; Petrissans, X.; Dunn, B.; Tolbert, S. H. Nanoporous Tin with a Granular Hierarchical Ligament Morphology as a Highly Stable Li-Ion Battery Anode. *ACS Appl Mater Interfaces* **2017**, *9* (1), 293–303. https://doi.org/10.1021/acsami.6b09014.

(4) Lv, H.; Qiu, S.; Lu, G.; Fu, Y.; Li, X.; Hu, C.; Liu, J. Nanostructured Antimony/Carbon Composite Fibers as Anode Material for Lithium-Ion Battery. *Electrochimica Acta* **2015**, *151*, 214–221. https://doi.org/10.1016/j.electacta.2014.11.013.

(5) Lee, K. T.; Cho, J. Roles of Nanosize in Lithium Reactive Nanomaterials for Lithium Ion Batteries. *Nano Today*. February 2011, pp 28–41. https://doi.org/10.1016/j.nantod.2010.11.002.

(6) Im, H. S.; Cho, Y. J.; Lim, Y. R.; Jung, C. S.; Jang, D. M.; Park, J.; Shojaei, F.; Kang, H. S. Phase Evolution of Tin Nanocrystals in Lithium Ion Batteries. *ACS Nano* **2013**, *7* (12),11103–11111. https://doi.org/10.1021/nn404837d.

(7) Xu, L.; Kim, C.; Shukla, A. K.; Dong, A.; Mattox, T. M.; Milliron, D. J.; Cabana, J. Monodisperse Sn Nanocrystals as a Platform for the Study of Mechanical

Damage during Electrochemical Reactions with Li. *Nano Letters* **2013**, *13* (4), 1800–1805.https://doi.org/10.1021/nl400418c.

(8) Xiong, P.; Wu, J.; Zhou, M.; Xu, Y. Bismuth-Antimony Alloy Nanoparticle@Porous Carbon Nanosheet Composite Anode for High-Performance Potassium-Ion Batteries. *ACS Nano* **2020**, *14* (1), 1018–1026. https://doi.org/10.1021/acsnano.9b08526.

(9) Bryngelsson, H.; Eskhult, J.; Nyholm, L.; Herranen, M.; Alm, O.; Edström, K. Electrodeposited Sb and Sb/Sb2O3 Nanoparticle Coatings as Anode Materials for Li-Ion Batteries.*Chemistry of Materials* **2007**, *19* (5), 1170–1180. https://doi.org/10.1021/cm0624769.

(10) Nguyen, A. G.; Le, H. T. T.; Verma, R.; Vu, D. L.; Park, C. J. Boosting Sodium-Ion Battery Performance Using an Antimony Nanoparticle Self-Embedded in a 3D Nitrogen-Doped Carbon Framework Anode. *Chemical Engineering Journal* **2022**, *429*. https://doi.org/10.1016/j.cej.2021.132359.

(11) Fang, G.; Deng, X.; Zou, J.; Zeng, X. Amorphous/Ordered Dual Carbon Coated Silicon Nanoparticles as Anode to Enhance Cycle Performance in Lithium Ion Batteries. *Electrochimica Acta* **2019**, *295*, 498–506. https://doi.org/10.1016/j.electacta.2018.10.186.

(12) Luo, W.; Zhang, P.; Wang, X.; Li, Q.; Dong, Y.; Hua, J.; Zhou, L.; Mai, L. Antimony Nanoparticles Anchored in Three-Dimensional Carbon Network as Promising Sodium-Ion Battery Anode. *Journal of Power Sources* **2016**, *304*, 340–345. https://doi.org/10.1016/j.jpowsour.2015.11.047.

(13) Yuan, Z.; Dong, L.; Gao, Q.; Huang, Z.; Wang, L.; Wang, G.; Yu, X. SnSb Alloy Nanoparticles Embedded in N-Doped Porous Carbon Nanofibers as a High-Capacity Anode Material for Lithium-Ion Batteries. *Journal of Alloys and Compounds* **2019**, *777*, 775–783. https://doi.org/10.1016/j.jallcom.2018.10.295.

(14) Pan, Q.; Wu, Y.; Zheng, F.; Ou, X.; Yang, C.; Xiong, X.; Liu, M. Facile Synthesis of M-Sb(M = Ni, Sn) Alloy Nanoparticles Embedded in N-Doped Carbon Nanosheets as High Performance Anode Materials for Lithium Ion Batteries. *Chemical Engineering Journal* **2018**, *348*, 653–660. https://doi.org/10.1016/j.cej.2018.05.043.

(15) Zhang, W.; Miao, W.; Liu, X.; Li, L.; Yu, Z.; Zhang, Q. High-Rate and Ultralong-Stable Potassium-Ion Batteries Based on Antimony-Nanoparticles Encapsulated in Nitrogen and Phosphorus Co-Doped Mesoporous Carbon Nanofibers as an Anode Material. *Journal of Alloys and Compounds* **2018**, *769*, 141–148. https://doi.org/10.1016/j.jallcom.2018.07.369.

(16) Cheng, Y.; Huang, J.; Li, R.; Xu, Z.; Cao, L.; Ouyang, H.; Li, J.; Qi, H.; Wang, C. Enhanced Cycling Performances of Hollow Sn Compared to Solid Sn in Na-Ion Battery. *Electrochimica Acta* **2015**, *180*, 227–233. https://doi.org/10.1016/j.electacta.2015.08.125.

(17) Liu, J.; Yang, Z.; Wang, J.; Gu, L.; Maier, J.; Yu, Y. Three-Dimensionally Interconnected Nickel-Antimony Intermetallic Hollow Nanospheres as Anode Material for High-Rate Sodium-Ion Batteries. *Nano Energy* **2015**, *16*, 389–398. https://doi.org/10.1016/j.nanoen.2015.07.020.

(18) Lin, Z.; Wang, G.; Xiong, X.; Zheng, J.; Ou, X.; Yang, C. Ni-Polymer Gels-Derived Hollow NiSb Alloy Confined in 3D Interconnected Carbon as Superior Sodium-Ion Battery Anode. *Electrochimica Acta* **2018**, *269*, 225–231. https://doi.org/10.1016/j.electacta.2018.03.010.

(19) Boebinger, M. G.; Yarema, O.; Yarema, M.; Unocic, K. A.; Unocic, R. R.; Wood, V.; McDowell, M. T. Spontaneous and Reversible Hollowing of Alloy Anode Nanocrystals for Stable Battery Cycling. *Nature Nanotechnology* **2020**, *15* (6), 475–481.https://doi.org/10.1038/s41565-020-0690-9.

(20) Zhou, D.; Song, W. L.; Fan, L. Z. Hollow Core-Shell SnO2/C Fibers as Highly Stable Anodes for Lithium-Ion Batteries. *ACS Applied Materials and Interfaces* **2015**, *7* (38), 21472–21478. https://doi.org/10.1021/acsami.5b06512.

(21) Hong, W.; Ge, P.; Jiang, Y.; Yang, L.; Tian, Y.; Zou, G.; Cao, X.; Hou, H.; Ji, X. Yolk-Shell-Structured Bismuth@N-Doped Carbon Anode for Lithium-Ion Battery with High Volumetric Capacity. *ACS Applied Materials and Interfaces* **2019**, *11* (11), 10829–10840. https://doi.org/10.1021/acsami.8b20477.

(22) Li, S.; Niu, J.; Zhao, Y. C.; So, K. P.; Wang, C.; Wang, C. A.; Li, J. High-Rate Aluminium Yolk-Shell Nanoparticle Anode for Li-Ion Battery with Long Cycle Life and Ultrahigh Capacity. *Nature Communications* **2015**, *6*. https://doi.org/10.1038/ncomms8872.

(23) Liu, N.; Lu, Z.; Zhao, J.; Mcdowell, M. T.; Lee, H. W.; Zhao, W.; Cui, Y. A Pomegranate-Inspired Nanoscale Design for Large-Volume-Change Lithium Battery Anodes. *Nature Nanotechnology* **2014**, *9* (3), 187–192. https://doi.org/10.1038/nnano.2014.6.

(24) McCue, I.; Benn, E.; Gaskey, B.; Erlebacher, J. Dealloying and Dealloyed Materials. *Annual Review of Materials Research* **2016**, *46* (1), 263–286. https://doi.org/10.1146/annurev-matsci-070115-031739.

(25) Kunduraci, M. Dealloying Technique in the Synthesis of Lithium-Ion Battery Anode Materials. *Journal of Solid State Electrochemistry*. Springer New York LLC August 1, 2016, pp 2105–2111. https://doi.org/10.1007/s10008-016-3226-3.

(26) Wang, Z.; Fei, P.; Xiong, H.; Qin, C.; Zhao, W.; Liu, X. CoFe2O4 Nanoplates Synthesized by Dealloying Method as High Performance Li-Ion Battery Anodes. *Electrochimica Acta* **2017**, *252*, 295–305. https://doi.org/10.1016/j.electacta.2017.08.189.

(27) Zhang, H.; An, W.; Song, H.; Xiang, B.; Mei, S.; Hu, Y.; Gao, B. Synthesis of Micro-Sized Porous Antimony via Vapor Dealloying for High-Performance Na-Ion Battery Anode. *Solid State Ionics* **2020**, *352*. https://doi.org/10.1016/j.ssi.2020.115365.

(28) Cook, J. B.; Lin, T. C.; Detsi, E.; Weker, J. N.; Tolbert, S. H. Using X-Ray Microscopy to Understand How Nanoporous Materials Can Be Used to Reduce the Large Volume Change in Alloy Anodes. *Nano Letters* **2017**, *17* (2), 870–877. https://doi.org/10.1021/acs.nanolett.6b04181.

(29) Li, M.; Qiu, T.; Foucher, A. C.; Fu, J.; Wang, Z.; Zhang, D.; Rappe, A. M.; Stach, E. A.; Detsi, E. Impact of Hierarchical Nanoporous Architectures on Sodium Storage in Antimony-Based Sodium-Ion Battery Anodes. *ACS Applied Energy Materials* **2020**, *3* (11), 11231–11241. https://doi.org/10.1021/acsaem.0c02161.

(30) Lin, T. C.; Dawson, A.A.; King, S. C.; Yan, Y.; Ashby, D. S.; Mazzetti, J. A.; Dunn, B. S.; Weker, J. N.; Tolbert, S. H. Understanding Stabilization in Nanoporous Intermetallic Alloy Anodes for Li-Ion Batteries Using Operando Transmission x-Ray Microscopy.*ACS Nano* **2020**, *14* (11), 14820–14830. https://doi.org/10.1021/acsnano.0c03756.

(31) Chou, C. Y.; Hwang, G. S. On the Origin of the Significant Difference in Lithiation Behavior between Silicon and Germanium. *Journal of Power Sources* **2014**, *263*, 252–258. https://doi.org/10.1016/j.jpowsour.2014.04.011.

(32) Cook, J. B.; Lin, T. C.; Detsi, E.; Weker, J. N.; Tolbert, S. H. Using X-Ray Microscopy to Understand How Nanoporous Materials Can Be Used to Reduce the Large Volume Change in Alloy Anodes. *Nano Letters* **2017**, *17* (2), 870–877 https://doi.org/10.1021/acs.nanolett.6b04181.

Chapter 6: Redox Active Dodecaborates as a Cathode Material for Li-ion Batteries

6.1 Introduction

Lithium ion batteries are incredibly prevalent today. Because of their relatively large energy density and lifetime, they power electronic devices: cellphones, laptops, and cars. To increase adoption to grid scale storage or heavier duty vehicles, the energy density must increase. Often, the cathode material limits the energy density of the battery because its gravimetric capacity, charge stored per gram of material, is less than conventional anodes. For example, common cathodes like lithium cobalt oxide, lithium manganese oxide, lithium nickel cobalt aluminum oxide, and nickel manganese cobalt oxide all have capacities lower than graphite at 372 mAh/g.[1–4] Secondly, cathodes contribute significantly to the cost of the battery because they contain rare earth metals. As a result, researchers have studied lithium sulfur batteries, where sulfur is the cathode.

Sulfur is very cheap in comparison to rare earth metals, and it offers a very high capacity, going from elemental sulfur (S_8) to lithium sulfide (Li_2S).[5–7] Many lithium polysulfides are intermediates: Li_2S_2, Li_2S_4, Li_2S_6. These polysulfides are soluble in the electrolyte, leading to rapid capacity decay due to active material leaving the electrode. Because of this shuttling, lithium sulfur batteries have not been widely adopted. Many researchers have tried to mitigate the effects of this effect. Some methods have included physically trapping the sulfur through core-shell networks or using electronic structure to anchor polysulfides.[8–10] Others have tried to use catalysis to speed up the reaction so that the polysulfides are not long-lasting.[11,12] Wudl et al. crosslinked benzene rings with disulfide bridges at three vertices.[13,14] If full capacity is not realized, each sulfur stays bonded to a network and cannot dissolve into the electrolyte. However, the theoretical capacity is much lower than elemental sulfur due to only one disulfide

bridge breaking, half of the elemental sulfur capacity, and the excess mass of the benzene ring. Here, we use this idea as a model, but instead of benzene rings, we use red-ox active dodecaborates.

Dodecaborates are icosahedral cages made of twelve boron atoms.[14] Electron density is delocalized across the entire cage, leading to incredible stability. They have been used for gas separation, biological therapies, polymer doping, and flow batteries, to name a few applications.[15–18] Using solution synthetic methods, these clusters can be functionalized in a variety of ways. This can include functionalization on all twelve vertices, some vertices, or heterofunctionalization. When functionalized, the clusters are redox active. The functional groups on the vertices dictate the voltage window of redox, which can range several volts.[19] Depending on the functional group, the cage can have up to four states: -2, -1, 0, +1.[20]

In this study, we crosslink dodecaboranes with disulfide bridges and obtain redox from two redox centers: the sulfur and the dodecaborate cage. A target reaction pathway is in Figure 6.1a. To accomplish this, we take advantage of the cluster stability and perform a heterogeneous, solid-state reaction at 800° C. This is uncommon for boron clusters, as most syntheses are done using solution-phase methods. Additionally, this is also one of the first times boron cluster redox has been observed in the solid state, whereas most measurements were done in solution.

6.2 Synthesis and Characterization

To convert these clusters to crosslinked sulfurized clusters, precursor clusters are heated in a tube furnace with flowing hydrogen sulfide at various temperatures. The precursor clusters are cesium iododododecaborate ($Cs_2B_{12}I_{12}$) and lithium iododododecaborate ($Li_2B_{12}I_{12}$) which are synthesized using previously published solution phase methods.[14] Figure 6.1b shows a FTIR spectrum comparison. The starting material is observed to contain boron iodide bonds at around 2900 cm^{-1}.[21] After the hydrogen sulfide treatment, the boron iodide bonds are no longer in the material and boron hydrogen bonds appear at around 2500 cm^{-1}. [22,23]

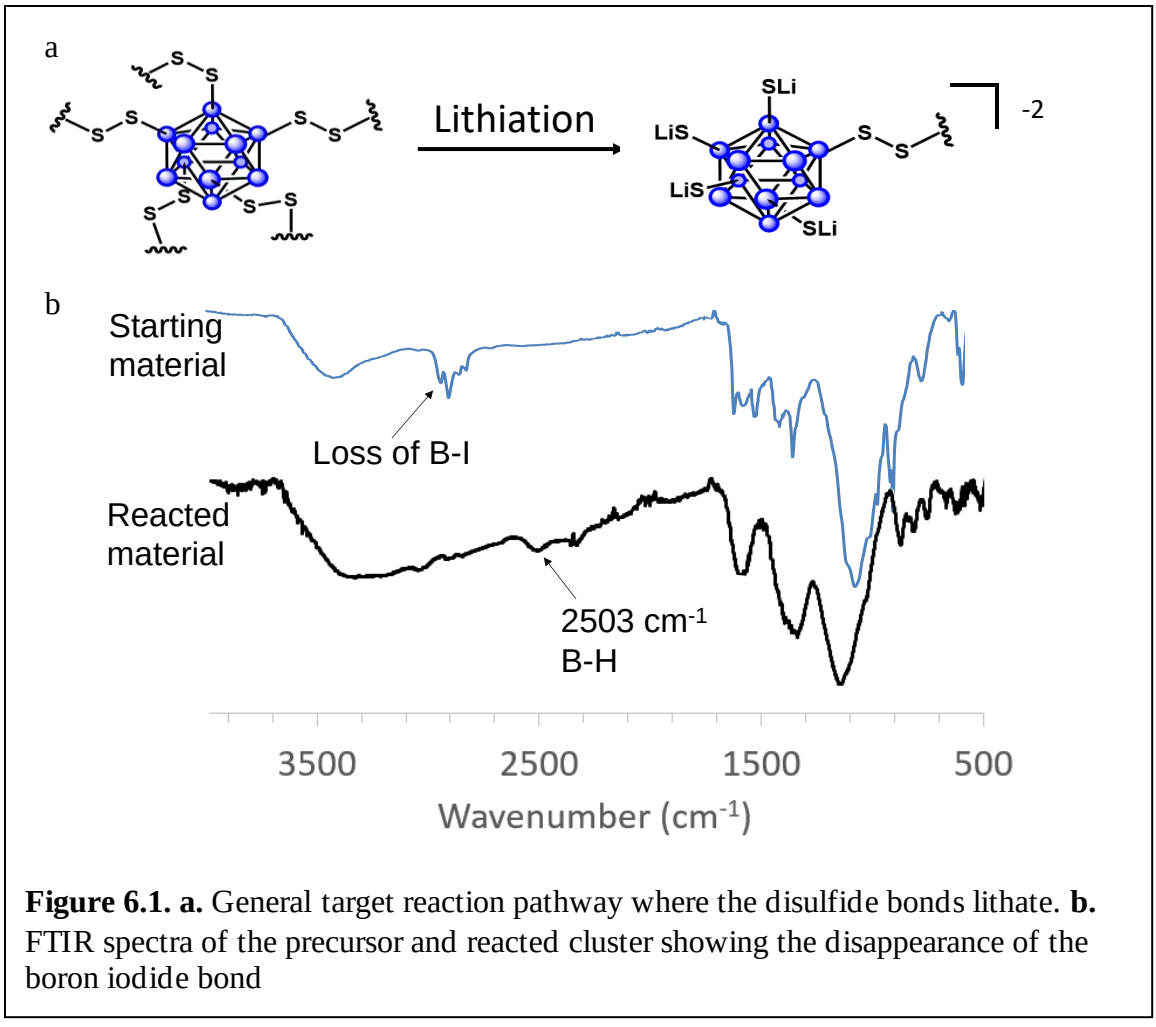

Figure 6.1. a. General target reaction pathway where the disulfide bonds lithate. **b.** FTIR spectra of the precursor and reacted cluster showing the disappearance of the boron iodide bond

To further understand the structure and bonding motifs of the resulting compound, x-ray photoelectron spectroscopy (XPS) was performed. Figure 6.2 shows the results. Generally, as the temperature increased, the degree of sulfurization increases, but the cluster degrades after 800°C. So 800°C was chosen as the temperature for synthesis. The sulfur spectrum provides insight to the bonding motifs of the sulfur. Figure 6.2a is a sulfur spectrum of a compound with one sulfur bonded to one vertex of the boron cage ($Cs_2B_{12}H_{11}SH$). There are three distinct peaks. The first peak at lowest binding energy, around 159 eV, is the thiol peak. It is also the peak with the largest area which is reasonable because the compound mainly has a thiol. The next peak, at around 162 eV, indicates the disulfide. The model compound surface degrades to have disulfides. Similar to other systems, the disulfide is a couple to a few eV's shifted to higher energy compared to the thiol.[12,24,25] The last peak is surface oxidation indicating sulfate, around 169 eV, which is in line with other sulfate compounds.

To obtain the most sulfur and prevent degradation, the precursor clusters were heated at 800° C. Figure 6.2b indicates that the boron from the cluster is intact revealing a peak at 188.5 eV which is consistent with boron in a dodecaborate. Figure 6.2c is the sulfur spectrum of the synthesized compound revealing that the main peak is consistent with the disulfide observed with the model compound. This, in conjunction with FTIR spectrum suggests that the structure is a boron cluster crosslinked to other clusters through disulfide bridges seen in Figure 6.2d where

the blue atoms are boron. When not bonded to sulfur, the boron is terminated by a hydrogen atom.

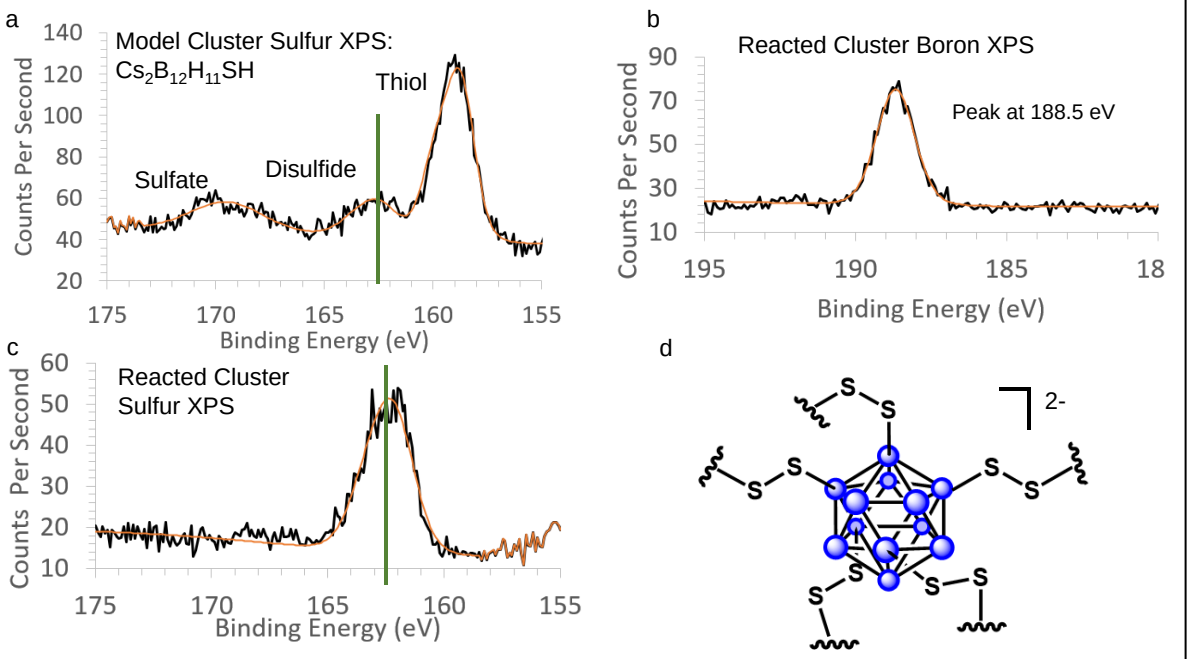

Figure 6.2. a. Sulfur XPS spectrum of a model cluster to indicate where to expect thiol, disulfide, and sulfate peaks **b.** Boron XPS spectrum of the reacted cluster showing that the boron cage is intact **c.** Sulfur XPS spectrum of the reacted cluster indicating that disulfide linkages are the major bonding motif for the sulfur in the compound **d.** ChemDraw model of the expected crosslinked boron cluster stoichiometry

6.3 Electrochemistry

Figure 6.3 shows the electrochemistry of the clusters. Electrodes were made in a 70:15:5:10 ratio of active material: carbon fiber: carbon nanotubes: PVDF. There were cycled in1 M lithium fluorophosphate ($LiPF_6$) in 50:50 ethylene carbonate (EC): diethyl carbonate (DEC). Figure 6.3a is the cyclic voltammetry of the cluster cycled at 0.1 mV/s. The highlighted region is the first cycle which begins by cycling to higher voltage, taking out lithium from the structure. The large peak, at around 4.2 V (vs. Li/Li^+) is lithium coming out of the structure that

balances the boron cluster, indicating cluster oxidation. As the voltage goes down, there are two peaks. One associated with sulfur reduction and another associated with cluster reduction. As the second cycle progresses, there are two peaks during oxidation: sulfur and cluster. This is different than the first cycle where there is only one main peak. This is reasonable because in the first cycle, the sulfur is not in its reduced form so there are no lithium ions to extract. Whereas, in the second cycle, both the cluster and the sulfur are reduced and can provide lithium to cycle. This system is unique in that the sulfur and the cluster are electron transfer centers. In this system the reversibility is poor and the peak separation is large. For further studies, optimization with different electrolyte systems can reveal better electrochemistry.

To mimic a more realistic scenario, galvanostatic cycling was performed on this material at a rate of C/15 with a theoretical capacity of 600 mAh/g. Figure 6.3b shows the results. The

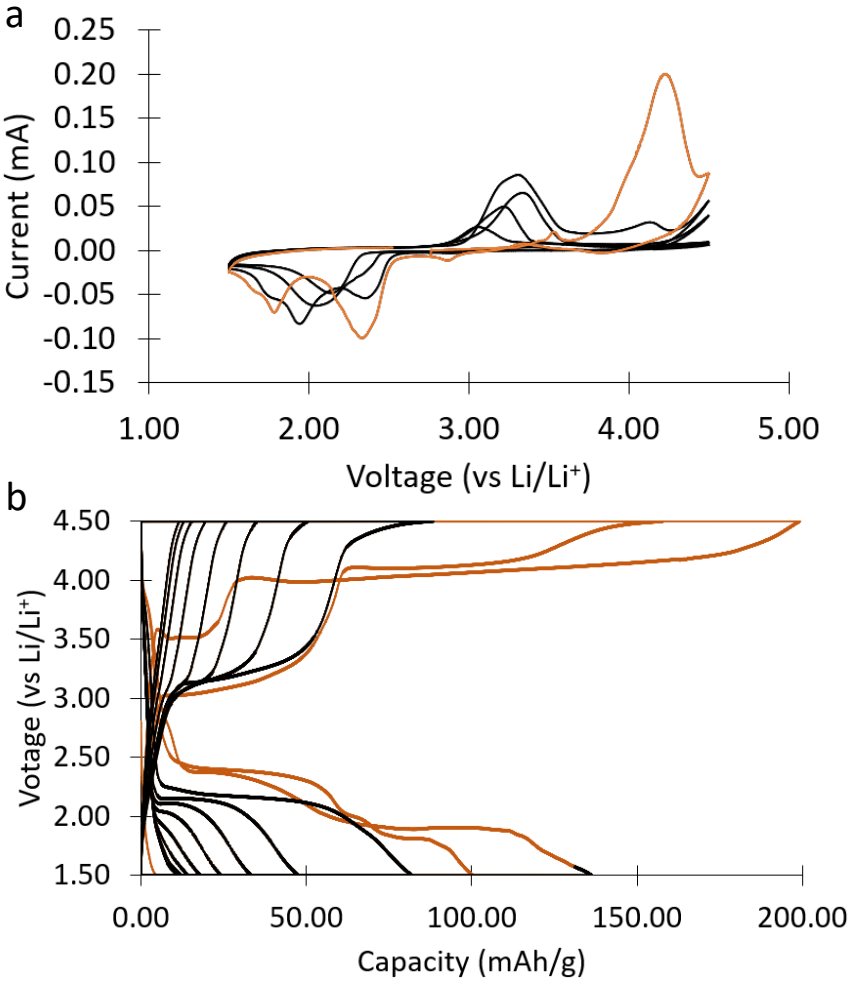

Figure 6.3. a. Cyclic voltammograms of the sulfurized cluster at 0.1 mV/s in 1 M $LiPF_6$ in EC:DEC **b.** Galvanostatic cycling of the sulfurized cluster at rate of C/15 in1 M $LiPF_6$ in EC;DEC

first two cycles are highlighted. In both reduction and oxidation, there are two plateaus that indicate two electron transfer events. This is in line with reduction and oxidation occurring at the sulfur as well as the boron cluster. Each plateau is roughly where the peaks are in the cyclic voltammetry. Degradation occurs quickly and the material only survives several cycles. However, there is clear evidence showing two electron transfer events. The obtained capacity is

also lower than the theoretical. There are a number of reasons to explain why the material performs poorly including degradation and lack of electrolyte access to the entire material. However, the material still provides more than 100 mAh/g and has both anionic and cationic reduction and oxidation in the same material.

6.4 Conclusion

In this study, we synthesized a novel dodecaborate crosslinked by disulfide bridges polymer using a heterogeneous solid state synthesis. When cycled, this material uniquely had both the cluster and the sulfur participating in electron transfer. Even though there was poor reversibility, the material obtained over 100 mAh/g in capacity. This proof of concept can be improved several ways. The oxidation of the cluster is relatively high, so using different electrolytes to prevent degradation will improve reversibility. In addition, the peak separation is large and the obtained capacity is much lower than theoretical. One way to increase electrolyte access and kinetics would be to nanostructure the material which may increase the capacity and help with reversibility. This study one of the few times boron cluster electron transfer has been observed in the solid state, and it also exhibits how boron clusters can be transformational in cathode materials due to their high oxidation potential and low molecular weight which opens doors to fundamentally new types of cathode materials that can improve our current battery technology.

6.5 References

(1) Manthiram, A.; Goodenough, J. B. Layered Lithium Cobalt Oxide Cathodes. *Nature Energy*. Nature Research March 1, 2021, p 323. https://doi.org/10.1038/s41560-020-00764-8.

(2) de Hoog, J.; Timmermans, J.-M.; Ioan-Stroe, D.; Swierczynski, M.; Jaguemont, J.; Goutam, S.; Omar, N.; van Mierlo, J.; van den Bossche, P. Combined Cycling and Calendar Capacity Fade Modeling of a Nickel-Manganese-Cobalt Oxide Cell with Real-Life Profile Validation. *Appl Energy* **2017**, *200*, 47–61. https://doi.org/https://doi.org/10.1016/j.apenergy.2017.05.018.

(3) Lesel, B. K.; Ko, J. S.; Dunn, B.; Tolbert, S. H. Mesoporous LixMn2O4 Thin Film Cathodes for Lithium-Ion Pseudocapacitors. *ACS Nano* **2016**, *10* (8), 7572–7581. https://doi.org/10.1021/acsnano.6b02608.

(4) Wong, D.; Shrestha, B.; Wetz, D. A.; Heinzel, J. M. Impact of High Rate Discharge on the Aging of Lithium Nickel Cobalt Aluminum Oxide Batteries. *J Power Sources* **2015**, *280*, 363–372. https://doi.org/https://doi.org/10.1016/j.jpowsour.2015.01.110.

(5) Wild, M.; O'Neill, L.; Zhang, T.; Purkayastha, R.; Minton, G.; Marinescu, M.; Offer, G. J. Lithium Sulfur Batteries, a Mechanistic Review. *Energy Environ Sci* **2015**, *8* (12), 3477–3494. https://doi.org/10.1039/C5EE01388G.

(6) Peng, H. J.; Huang, J. Q.; Cheng, X. B.; Zhang, Q. Review on High-Loading and High-Energy Lithium–Sulfur Batteries. *Advanced Energy Materials*. Wiley-VCH Verlag December 20, 2017. https://doi.org/10.1002/aenm.201700260.

(7) Rana, M.; Ahad, S. A.; Li, M.; Luo, B.; Wang, L.; Gentle, I.; Knibbe, R. Review on Areal Capacities and Long-Term Cycling Performances of Lithium Sulfur Battery at High

Sulfur Loading. *Energy Storage Materials*. Elsevier B.V. March 1, 2019, pp 289–310. https://doi.org/10.1016/j.ensm.2018.12.024.

(8) Yan, R.; Oschatz, M.; Wu, F. Towards Stable Lithium-Sulfur Battery Cathodes by Combining Physical and Chemical Confinement of Polysulfides in Core-Shell Structured Nitrogen-Doped Carbons. *Carbon N Y* **2020**, *161*, 162–168. https://doi.org/10.1016/j.carbon.2020.01.046.

(9) Xu, J.; Tang, W.; Yu, F.; Zhao, S.; Niu, D.; Zhang, X.; Xin, Z.; Chen, R. Trimming the π Bridge of Microporous Frameworks for Bidentate Anchoring of Polysulfides to Stabilize Lithium–Sulfur Batteries. *J. Mater. Chem. A* **2020**, *8* (36), 19001–19010. https://doi.org/10.1039/D0TA06383E.

(10) Luo, C.; Hu, E.; Gaskell, K. J.; Fan, X.; Gao, T.; Cui, C.; Ghose, S.; Yang, X.-Q.; Wang, C. A Chemically Stabilized Sulfur Cathode for Lean Electrolyte Lithium Sulfur Batteries. **2020**, *117* (26). https://doi.org/10.1073/pnas.2006301117/-/DCSupplemental.

(11) Peng, L.; Wei, Z.; Wan, C.; Li, J.; Chen, Z.; Zhu, D.; Baumann, D.; Liu, H.; Allen, C. S.; Xu, X.; Kirkland, A. I.; Shakir, I.; Almutairi, Z.; Tolbert, S.; Dunn, B.; Huang, Y.; Sautet, P.; Duan, X. A Fundamental Look at Electrocatalytic Sulfur Reduction Reaction. *Nat Catal* **2020**, *3* (9), 762–770. https://doi.org/10.1038/s41929-020-0498-x.

(12) Hu, Q.; Wang, B.; Lu, J.; Zhang, C.; Yang, C.; Chang, S.; Dong, H.; Wu, C.; Hong, Y.; Zhang, L. Promoting Electrocatalytic Conversion of Polysulfide Using Cobalt Disulfide Nanocrystals for Lithium Sulfur Batteries. *The Journal of Physical Chemistry C* **2020**, *124* (39), 21319–21328. https://doi.org/10.1021/acs.jpcc.0c06135.

(13) Preefer, M. B.; Oschmann, B.; Hawker, C. J.; Seshadri, R.; Wudl, F. High Sulfur Content Material with Stable Cycling in Lithium-Sulfur Batteries. *Angewandte Chemie* **2017**, *129* (47), 15314–15318. https://doi.org/10.1002/ange.201708746.

(14) Axtell, J. C.; Saleh, L. M. A.; Qian, E. A.; Wixtrom, A. I.; Spokoyny, A. M. Synthesis and Applications of Perfunctionalized Boron Clusters. *Inorg Chem* **2018**, *57* (5), 2333–2350. https://doi.org/10.1021/acs.inorgchem.7b02912.

(15) Zhang, Y.; Yang, L.; Wang, L.; Duttwyler, S.; Xing, H. A Microporous Metal-Organic Framework Supramolecularly Assembled from a Cu II Dodecaborate Cluster Complex for Selective Gas Separation . *Angewandte Chemie* **2019**, *131* (24), 8229–8234. https://doi.org/10.1002/ange.201903600.

(16) Fukuo, Y.; Hattori, Y.; Kawabata, S.; Kashiwagi, H.; Kanemitsu, T.; Takeuchi, K.; Futamura, G.; Hiramatsu, R.; Watanabe, T.; Hu, N.; Takata, T.; Tanaka, H.; Suzuki, M.; Miyatake, S. I.; Kirihata, M.; Wanibuchi, M. The Therapeutic Effects of Dodecaborate Containing Boronophenylalanine for Boron Neutron Capture Therapy in a Rat Brain Tumor Model. *Biology (Basel)* **2020**, *9* (12), 1–16. https://doi.org/10.3390/biology9120437.

(17) Aubry, T. J.; Axtell, J. C.; Basile, V. M.; Winchell, K. J.; Lindemuth, J. R.; Porter, T. M.; Liu, J. Y.; Alexandrova, A. N.; Kubiak, C. P.; Tolbert, S. H.; Spokoyny, A. M.; Schwartz, B. J. Dodecaborane-Based Dopants Designed to Shield Anion Electrostatics Lead to Increased Carrier Mobility in a Doped Conjugated Polymer. *Advanced Materials* **2019**, *31* (11). https://doi.org/10.1002/adma.201805647.

(18) Barton, J. L.; Wixtrom, A. I.; Kowalski, J. A.; Qian, E. A.; Jung, D.; Brushett, F. R.; Spokoyny, A. M. Perfunctionalized Dodecaborate Clusters as Stable Metal-Free Active

Materials for Charge Storage. *ACS Appl Energy Mater* **2019**, *2* (7), 4907–4913. https://doi.org/10.1021/acsaem.9b00610.

(19) Wixtrom, A. I.; Parvez, Z. A.; Savage, M. D.; Qian, E. A.; Jung, D.; Khan, S. I.; Rheingold, A. L.; Spokoyny, A. M. Tuning the Electrochemical Potential of Perfunctionalized Dodecaborate Clusters through Vertex Differentiation. *Chemical Communications* **2018**, *54* (46), 5867–5870. https://doi.org/10.1039/C8CC03477J.

(20) Stauber, J. M.; Schwan, J.; Zhang, X.; Axtell, J. C.; Jung, D.; McNicholas, B. J.; Oyala, P. H.; Martinolich, A. J.; Winkler, J. R.; See, K. A.; Miller, T. F.; Gray, H. B.; Spokoyny, A. M. A Super-Oxidized Radical Cationic Icosahedral Boron Cluster. *J Am Chem Soc* **2020**, *142* (30), 12948–12953. https://doi.org/10.1021/jacs.0c06159.

(21) Finch, A.; Hyams, I. J.; Steele, D. Far Infra-Red Spectra of Boron Tri-Bromide and Boron Tri-Iodide. *Trans. Faraday Soc.* **1965**, *61* (0), 398–401. https://doi.org/10.1039/TF9656100398.

(22) Muetterties, E. L.; Merrifield, R. E.; Miller, H. C.; Knoth, W. H.; Downing, J. R. Chemistry of Boranes. III.1 The Infrared and Raman Spectra of B12H12 - and Related Anions. *J Am Chem Soc* **1962**, *84* (13), 2506–2508. https://doi.org/10.1021/ja00872a011.

(23) Tague, T. J.; Andrews, L. Reactions of Pulsed-Laser Evaporated Boron Atoms with Hydrogen. Infrared Spectra of Boron Hydride Intermediate Species in Solid Argon. *J Am Chem Soc* **1994**, *116* (11), 4970–4976. https://doi.org/10.1021/ja00090a048.

(24) Castner, D. G.; Hinds, K.; Grainger, D. W. X-Ray Photoelectron Spectroscopy Sulfur 2p Study of Organic Thiol and Disulfide Binding Interactions with Gold Surfaces. *Langmuir* **1996**, *12* (21), 5083–5086. https://doi.org/10.1021/la960465w.

(25) Liu, W.; Luo, C.; Zhang, S.; Zhang, B.; Ma, J.; Wang, X.; Liu, W.; Li, Z.; Yang, Q.-H.; Lv, W. Cobalt-Doping of Molybdenum Disulfide for Enhanced Catalytic Polysulfide Conversion in Lithium–Sulfur Batteries. *ACS Nano* **2021**, *15* (4), 7491–7499. https://doi.org/10.1021/acsnano.1c00896.